ISBN ISBN 978-82-471-1760-6 (printed ver.)
ISBN ISBN 978-82-471-1761-3 (electronic ver.)
ISSN 1503-8181

Doctoral theses at NTNU, 2009:182

Morten Stakkeland

Tracking in radar surveillance systems

NTNU
Norwegian University of
Science and Technology

Thesis for the degree of
philosophiae doctor
Faculty of Information Technology, Mathematics and
Electrical Engineering
Department of Engineering Cybernetics

NTNU
Norwegian University of
Science and Technology

Doctoral theses at NTNU, 2009:182

NTNU

Morten Stakkeland

Tracking in radar surveillance systems

Thesis for the degree of philosophiae doctor

Trondheim, January 2010

Norwegian University of
Science and Technology
Faculty of Information Technology, Mathematics and Electrical Engineering
Department of Engineering Cybernetics

NTNU
Norwegian University of Science and Technology

Thesis for the degree of philosophiae doctor

Faculty of Information Technology, Mathematics and Electrical Engineering
Department of Engineering Cybernetics

ISBN 978-82-471-1760-6 (printed ver.)
ISBN 978-82-471-1761-3 (electronic ver.)
ISSN 1503-8181

ITK-report 2010-1-W

Doctoral Theses at NTNU, 2009:182

Printed by Tapir Uttrykk

Preface

THIS thesis is submitted in fulfillment of the requirements for the degree "Philosophiae Doctor" at the Norwegian University of Science and Technology (NTNU), the Department of Engineering Cybernetics. The research was a part of the SEALS - Sea Air and Land Surveillance project which was funded in part by the Research Council of Norway under grant number 159373/I40.

Acknowledgments

I would first of all like to thank my two supervisors Oddvar Hallingstad and Øyvind Overrein for providing me with excellent guidance and support throughout this whole process. I owe most of my knowledge about radar signal processing and statistical estimation to these two.

The other students in the Cybernetics group at UNIK have also been an important resource over these years. There has always been a resourceful person in the hallway that could be used as sparring partner for new ideas. Especially thanks to my office mate and table tennis opponent Morten for many fruitful discussions. Keep on working on that forehand smash. Good luck to Roar the newcomer.

The staff and students at the ISIF lab at the university of New Orleans gave me valuable support and input during my stay in New Orleans. I learned a lot from Professor Xiao-Rong Li as well as the rest of the group. Hurricane Katrina is not thanked.

The industrial sponsors that made the SEALS program possible are also thanked, Norcontrol IT, Kongsberg Maritime, Kongsberg Defence and Aerospace and Park Air Systems. By funding research and education of new researchers in this manner, they have laid the foundation for technical progress within the field. Special thanks to the members of the steering committee, who provided valuable feedback to our work.

Also thanks to friends and family who provided help with proofreading and mental support.

Finally, I would like to send huge thanks to Sverre and Inger for showing great patience and tolerance during this whole process and for surviving many working vacations on Jeløya. You are the best.

Summary

THE first part of this thesis focuses on the detection part of a radar surveillance system, and specifically derive methods for estimating the clutter density in a CFAR system from scan to scan, by making some basic assumptions on the system configuration. It is shown how the gain in applying a Bayesian estimator depend on the system configuration, and the gain is analyzed for some well known CFAR configurations. As an intermediate result, the variance of the clutter density for some CFAR configurations is derived. It is indicated how the derived variance may be a useful tool in the analysis of CFAR systems. Empirical Bayesian estimation is introduced as a way to apply optimal Bayesian estimation even though the prior density of the estimated random variable is unknown. Empirical Bayesian estimators in general use past data to estimate the prior density of the current random variable. A linear empirical Bayesian (LEB) estimator is applied to estimate the clutter density in the CFAR case, and it is shown that the LEB estimators converge to the corresponding linear Bayesian estimators as the set of past data gets large. The LEB estimators use the sample mean and variance of past measurements as inputs to estimate the current realization of the estimated random variable, or estimatee.

The second part of this thesis is related to modeling of the errors in surveillance radar position measurements, and developing estimation filters that incorporate the models into tracking systems in an optimal manner. Monte Carlo simulations using simplified rectangular target models and simplified models of the components in radar surveillance systems are used to generate large data sets of simulated measurements. The parameters of the proposed measurement error models are then estimated from the data sets, using maximum likelihood estimation methods. It is shown that there may be a correlation between the aspect angle of the target and position measurement errors when the target is extended relative to the resolution of the system. In tracking systems it is commonly assumed that no such correlation exists and that the measurement errors in range and bearing are independent. In this thesis, two new measurement models are proposed. One proposed model assumes that the measurement noise is independent of the bearing angle, but dependent on the aspect angle. A second proposed model incorporates dependencies on both aspect angle and bearing angle in the measurement equation. Several state dependent measurement equations are also proposed to model biases that in some applications may be present in surveillance radar measurements.

A discussion is given on how the standard Kalman filter fails to provide optimal estimates in

cases where the measurement noise is dependent on the state vector of the target, and best linear unbiased estimation (BLUE) filters are hence derived in order to apply optimal filtering in this case. It is shown how higher order unscented transforms may be used to approximate the terms of the recursive BLUE filter, and that a third order unscented transform fails to provide sufficient accuracy. Some simulation results show how the BLUE filters in some cases has better root mean square error (RMSE) performance than suboptimal Kalman filters that use the standard measurement models. Simulations using simulated radar measurements also show that the proposed new model that includes dependency on both bearing and aspect angle has the best performance at all ranges, while the model assuming uncorrelated noise in range and bearing is good at long range where the target becomes a point target.

A tool developed to generate trajectories consisting of random sequences of maneuvers is used in the simulations to generate a large number of random trajectories. This tool proves to be useful when analyzing the performance of the tracking filters, as it introduces the opportunity to analyze estimation filter performance as a function of a number of different kinematic parameters on trajectories that have dynamics that are realistic for the considered application.

List of papers

1. Morten Stakkeland and Xiao-Rong Li, "Estimating instantaneous false alarm rate in a CFAR system by Bayesian and empirical Bayesian methods," in *The Proceedings of the 2007 IEEE Radar Conference,* 2007. © 2007 IEEE. Reprinted, with permission, from The Proceedings of the 2007 IEEE Radar Conference .

2. Morten Stakkeland, Øyvind Overrein, and Oddvar Hallingstad. "Tracking and fusion of surveillance radar images of extended targets," in *The Proceedings of FUSION 2007, the 10th International Conference on Information Fusion*, 2007. Reprinted with permission from ISIF.

3. Morten Stakkeland, Øyvind Overrein, and Oddvar Hallingstad. "The error statistics of surveillance radar position measurements," in *The Proceedings of Radar 2007, the IET International Conference on Radar Systems*, 2007. Reprinted with permission from the IET.

4. Morten Stakkeland, Øyvind Overrein, Edmund Brekke, and Oddvar Hallingstad. "Tracking of targets with state dependent measurement errors using recursive BLUE filters," in *The Proceedings of FUSION 2009, the 12th International Conference on Information Fusion*, 2009. Reprinted with permission from ISIF.

List of acronyms

Acronym	
ADT	Average Decision Threshold
AIS	Automatic Identification System
BLUE	Best Linear Unbiased Estimator
CA-CFAR	Cell Averaging CFAR
CFAR	Constant False Alarm Rate
CUT	Cell Under Test
EB	Empirical Bayesian
GPS	Global Positioning System
HOUT	Higher Order UT
IMM	Interacting Multiple Models
IMO	International Maritime Organization
IPDAF	Integrated PDAF
ISAR	Inverse Synthetic Aperture Radar
JM	Jump Markov
JMNLS	JM Non Linear System
KLD	Kullback Leibler Divergence
LEB	Linear Empirical Bayesian
LMMSE	Linear Minimum Mean Square Error
MHT	Multiple Hypothesis Tracking
MMSE	Minimum Mean Square Error
MOM	Method of Moments
MSE	Mean Square Error
OS-CFAR	Ordered Statistics CFAR
PDAF	Probabilistic Data Association Filter
pdf	Probability density function
RCS	Radar Cross Section

Acronym	
RMSE	Root Mean Square Error
RMSEp	Position RMSE
RMSEv	Velocity RMSE
SNR	Signal to Noise Ratio
TBD	Track Before Detect
UT	Unscented Transform

Nomenclature

The nomenclature contains a summary of the notation used in paper chapter one to four, as well as the notation used in the papers one to four when it differs from paper one to four.

Notation	**Definition**
$P(A)$	Probability of event A
x	Vector valued random variable
X	Matrix valued random variable, random matrix
$F_z(x) = P(z \leq x)$	Cumulative probability function for z
$f_z(x) = \frac{d}{dx} F_z(x)$	Probability density function (pdf) for z
$f_z(x\|w)$	Conditional pdf for z given w
$g_z(m)$	Discrete probability mass function for z
$E(z) = \bar{z} = \int x f_z(x)\, dx$	Mean value, or expected value of z
$E(z\|w) = \int x f_z(x\|w)\, dx$	Conditional mean value of z given w
$C_z = cov(z) = E\left((z-\bar{z})(z-\bar{z})^T\right)$	Covariance of z
$\sigma_z^2 = var(z) = E\left((z-\bar{z})^2\right)$	Variance of one dimensional z
$cov(z\|w) = E\left((z-\bar{z})(z-\bar{z})^T\|w\right)$	Conditional covariance of z given w
$C_{xz} = cov(x,z) = E\left((x-\bar{x})(z-\bar{z})^T\right)$	Covariance of x and z
z_k	Kinematic measurement obtained at time t_k
$Z^k = \{z_1, z_2, ..., z_k\}$	Set of all kinematic measurements including t_k
m_k	Number of kinematic measurements at t_k
$Y^k = \{m_1, m_2, ..., m_k\}$	Set of all m_i including t_k
$\hat{x}_k^{MMSE} = E\left(x_k\|Z^k\right)$	MMSE estimator at t_k
$\hat{P}_k^{MMSE} = cov\left(x_k\|Z^k\right)$	Covariance of MMSE estimator
$\hat{x}_k^{BLUE}$	BLUE estimator at t_k
$MSE\left(\hat{x}_k^{BLUE}\right)$	Mean Square Error of BLUE estimator at t_k
$\hat{x}_k^{LEB}$	LEB estimator at t_k

Notation	Definition
$\mathcal{N}(x; \bar{x}, C_x)$	Normal distribution with mean $\bar{x}$ and covariance C_x
$\mathcal{IW}(X_k; n, C)$	Inverse Wishart distribution, n degrees of freedom, C positive definite
$\mathcal{W}(X_k; n, C)$	Wishart distribution, n degrees of freedom, C positive definite
θ	Heading angle
ϕ	Bearing angle
r	Range
ψ	Aspect angle
p_k^x	x component of position in Cartesian frame at t_k
v_k^x	x component of velocity vector at t_k
p_k^y	y component of position in Cartesian frame at t_k
v_k^y	y component of velocity vector at t_k

Notation paper one

Notation	Definition
$\hat{x}^{LMMSE} = \hat{x}^{BLUE}$	LMMSE notation used in *paper one*

Notation paper two

Notation	Definition
m_k	State of Markov chain at time t_k

Contents

1 Introduction

1.1 A short introduction to target tracking

To construct a system that can locate and track moving objects involves many challenging tasks. Firstly, the right kind of sensor needs to be applied and deployed in the system, sensors that can measure the properties of the objects with sufficient accuracy. Secondly, the measurements from the sensors may be noisy, they may measure different physical properties and they may provide measurements to the system at differing times and uneven intervals. These noisy measurements then have to be combined, or fused, in order to obtain an estimate of the position, velocity, acceleration, and in some cases the shape of the present objects. The objects may be invisible for periods of time, they may change shape or appearance, and they may be confused with other similar objects.

This multidisciplinary and complex field is called target tracking. Target tracking systems are currently being applied in an increasing number of applications where there is a need to locate and keep track of moving objects or targets. Many of the algorithms commonly used in target tracking systems have been developed for military or civilian surveillance systems, like for instance air traffic control systems. However, the emerging intelligent autonomous and semi-autonomous systems introduce a demand for accurate and reliable sensing systems that can map and keep track of objects in the vicinity. One example can be seen in the collision avoidance and warning systems in modern high end cars. The methods of target tracking have also been applied for tracking moving objects in video images. One example of such applications is to keep track of the football on the field in 3D, using the images from a number of 2D cameras as input.

The first link in the tracking system is the physical sensors. Some examples are radars, sonars, acoustic microphones, cameras, infrared cameras among many others. The system needs to have accurate models of the errors in each sensor in order to combine the measurements in an optimal manner. A measurement from an accurate sensor should be given higher credibility than one from a less accurate sensor. In some applications the targets may cooperate with the tracking system through a transponder system. The Automatic Identification System (AIS) in naval applications is an example of such a system. The monitored vessels transmit their identity and position data to a central surveillance system. This information can be combined with measurements from land

based radars in a central estimation system.

The measurements are then processed by computers to estimate the state of the system. Depending on the application, the computer may aim to estimate a number of different parameters. The number of targets present may be unknown and needs to be established before the kinematic state of each target can be estimated. The kinematic state of an object may among other parameters include position, velocity and acceleration. The state can be estimated using a combination of available measurements and a model of how the target moves. The system may in addition to kinematic state estimation also try to identify or classify the targets. Knowledge of the class of a target may in some cases help to identify its intentions.

Many advanced statistical methods can be applied in this process, including Bayesian inference and pattern recognition algorithms. The high computational power and storage capacity in modern computers has introduced the possibility to increase the complexity of real time target tracking systems significantly. This trend is likely to continue in the future, and may be further expanded with the increased use of parallel computing.

1.2 Surveillance with land based radars

The focus of this thesis is surveillance systems that apply one or more radars in order to keep track of moving objects. Examples of such systems are air traffic control systems and coastal surveillance systems. In these applications, the number of targets may be high and several radars may cover the same area. Figure 1.1 shows a two dimensional radar image obtained from a surveillance radar in harbor surveillance system. The figure shows a section of the Singapore harbor. About 25 ships can be seen in the image in addition to reflections from the sea surface and land structures. Radar signals reflected from the sea surface are sometimes called clutter and they often make tracking difficult. The system has to distinguish between clutter and measurements originating from real targets.

As mentioned previously, radar measurements can some times be combined with transponder systems. For instance the International Maritime Organization (IMO) has agreed on a standard, the AIS, where each ship transmits its identity and GPS measured position to land based centrals. This could in principle function as a stand-alone system, but in practice there is a need for complementary sensors in cases when vessels fail to give correct AIS data. In addition only vessels heavier than 300 gross tonnage on international voyages, vessels at more than 500 gross tonnage on domestic voyages, and all passenger vessels are required to carry an AIS transponder [1]. The radar measurements can also be used by the tracking algorithm to increase the total accuracy in the estimation algorithms.

The distance from the radars may in many cases vary from the order of meters to tens of kilometers. The second part of the work described in this thesis examines the errors in the radar position measurements as a function of the distance from the radar. It is shown that there is a difference in the nature of the measurement error at long and short ranges, and it is shown how this discovery can be used to improve the accuracy of tracking systems.

Each radar produces a large stream of data, up to several gigabytes per second. The radar image seen in figure 1.1 needs to be processed in order to extract position of each individual target. One possible approach is to threshold all the pixels, and group neighboring pixels into clusters. The position measurement can then be taken to be the center of each cluster. Each position measurement still has to be associated with the correct target. The first part of the thesis works with a special kind of method of generating the threshold, called Constant False Alarm Rate (CFAR) processing.

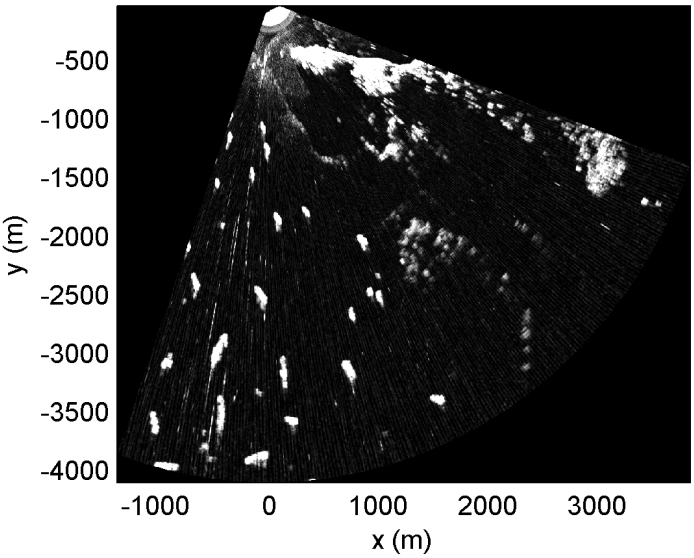

Figure 1.1: *Radar image of a section of the harbor of Singapore. Displayed with permission from Norcontrol IT.*

1.3 Main contributions

The main contributions of the thesis are summarized as follows.

- The statistics of the clutter density in CFAR systems is derived in *paper one*, extending analysis previously published in available literature. The derived results can be applied to analyze and optimize CFAR systems.

- A best linear unbiased estimator (BLUE) is derived for the clutter density in *paper one* under the assumption that the clutter density has a binomial distribution. The estimator may be integrated with data association algorithms which require clutter density as an input parameter in order to discriminate between clutter and targets. Empirical Bayesian estimation is introduced as a an extension of Bayesian estimation to cases where the prior distribution of the estimated variable is unknown.

- A framework for simulating radar position measurement errors for extended targets is described in *paper three* and chapter 3. Target radar images are generated using the methods described in [2]. It is demonstrated that there may be correlation between the aspect angle of a target and the position measurement noise. This correlation has previously been unknown or ignored in target tracking systems.

- Two new measurement models which incorporates the correlation between aspect angle and measurement noise are presented in *paper three*, and integrated into a tracking framework in *paper two*. One model assumes that the measurement noise is perfectly correlated with the aspect angle of the target, while one three parameter model includes correlation

with both aspect and bearing angle. The simulations in *paper two* and *paper four* show that the three parameter model is the best fit.

- Optimal BLUE filters for state dependent measurement errors are derived in *paper four.* The measurement equations applied in *paper two* are reformulated in order to derive optimal filters. The derived BLUE filters are demonstrated by Monte Carlo simulations to perform better than suboptimal filters when applied on the measurement models introduced in *paper three*.

- A tool for generation of random trajectories based on non linear jump Markov systems is introduced in *paper two* and further developed in *paper four*. The simulation tool provides a framework for generating sequences of realistic target maneuvers.

1.4 Thesis outline

This thesis is based on the work described in *paper one* to *four*, while the work in *paper one* is extended with some additional analyses and results in chapter 2. A more extensive discussion than provided in *paper two* on alternative methods to track extended targets is given in chapter 3. Chapter 3 also contains more elaborate discussions on radar position error modeling than what was provided in *paper two*, *paper three,* and *paper four*, and also extends the work in *paper three* by containing more elaborate descriptions of the components in the applied Monte Carlo simulations. Some additional simulation results are included in appendix A. Chapter 4 contains a discussion of the derived methods and results. *Paper one, paper two*, *paper three,* and *paper four* are then included in chapters five to eight.

2

Estimating clutter density in CFAR systems

In the following sections, the main results of *paper one* are summarized and extended with additional analysis and discussions. Some results and figures from *paper one* as well as additional background information are included for clarity.

2.1 Background

The clutter density or false alarm rate, which is the probability of obtaining a measurement that is not originating from a target within a cell or an area, is an important parameter for the data association algorithm. In the probabilistic data association filter (PDAF) algorithm [3] the clutter density is used to calculate the association probabilities within a validation gate, which is defined as the probability that each measurement within the gate originates from the target. The false alarm rate is also an important parameter when calculating track score [4], which may be used for track initiation, confirmation and deletion and is an important parameter in multiple hypothesis tracking (MHT).

In the parametric version of the PDAF algorithm, the number of false alarms is assumed to be given by a Poisson distribution

$$g_{m_k}(m) = P(m_k = m) = \frac{(\lambda_k V_k)^m}{m!} \exp(-\lambda_k V_k) \tag{2.1}$$

where the clutter density λ_k is assumed to be known, and V_k is the volume of the validation gate from which a number m_k of kinematic measurements are obtained. The expected number of false alarms at a given scan is then $\bar{m}_k = \lambda_k V_k$. The nonparametric version of the PDAF implicitly estimates the clutter density, by the use of a diffuse prior [3], as

$$\hat{\lambda}_k = \frac{m_k}{V_k} \tag{2.2}$$

The integrated PDAF algorithm (IPDAF) [5], introduced the estimator

$$\hat{\lambda}_k = \begin{cases} 0 \\ \frac{1}{V_k}\left[m_k - P_D P_G P\left(O_k | Y^{k-1}\right)\right] \end{cases} \tag{2.3}$$

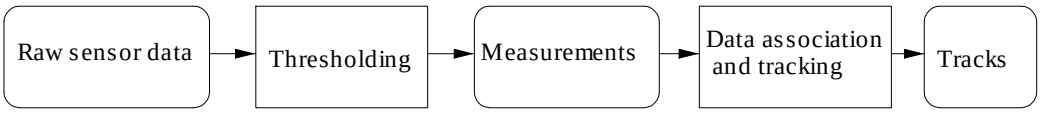

Figure 2.1: *Data flow in common tracking system.*

where P_D the probability of detection, P_G is the probability that the target is found within the validation region, and $P\left(O_k|Y^{k-1}\right)$ is the probability that the target exists at time t_k given the set $Y^{k-1} = \{m_1, m_2, ..., m_{k-1}\}$. Several additional estimators were introduced in [6], all of which include the probability that there exists a perceivable target at time t_k, a target that may provide a measurement. Several estimators were derived, including conditional mean estimators, as well as maximum likelihood (ML) estimators and estimators based on method of moments (MOM) approximation. Neither of these models incorporated any prior information about the clutter density.

In *paper one*, the clutter density, or instantaneous false alarm rate, in Constant False Alarm Rate (CFAR) systems were estimated using several different Bayesian estimators. The clutter density was modeled as a random variable, and its statistical distribution was derived for some different CFAR configurations. It was then shown how the clutter density could be estimated from scan to scan for some systems, gaining a more accurate estimate of the clutter density than when assuming that it is constant.

2.1.1 CFAR configurations

A graphical representation of how the raw radar or sonar data often is processed in tracking systems is given in figure 2.1. The pixel maps provided by the sensors are preprocessed by a CFAR algorithm, which sends a set of detections or measurements to a tracking algorithm at each scan. The data association and tracking algorithm then use the measurements to update the estimated states of existing tracks, initiate new tracks, and terminate tracks that no longer can be associated with measurements. An alternative approach to what is seen in figure 2.1, is the track before detect (TBD) approach, described for instance in [4]. In TBD algorithms, target tracking is performed based on raw data over several scans before a detection is declared. TBD algorithms are in general computationally expensive and thus hard to incorporate in a real time surveillance system with high data rates.

The main principle behind all CFAR configurations is that the threshold used to determine whether a given cell contains a target or not is calculated using a set of reference cells. The averaging can be temporal or spatial, meaning that the reference set can be chosen over a region at a given time, or for a given set of cells over time. A generic CFAR system is shown in figure 2.2. The cells $x_1, x_2 ... x_N$ as well as the cells $y_1^i, y_2^i, ..., y_M^i$ in each of the reference sets D_1,D_2, ..., D_N are random variables. The distribution of each random variable depends on a number of different parameters. For instance, the distribution of reflections from the surface of the ocean depends on the state of the sea surface [7]. Rayleigh, Weibull, K-distribution and log-normal distributions are commonly used noise model in radar and sonar systems. The values in the cells may be measurements of either amplitude or intensity, which will influence the distribution in each pixel.

The number of declared measurements is given as the sum of the indicator functions, $\sum_{i=1}^{N} I_i$. The threshold T_i used to test a cell x_i is calculated using using a function f on a set of reference

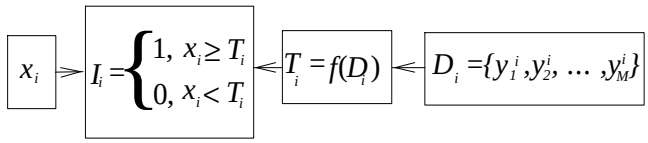

Figure 2.2: *Representation of Generic CFAR system, $i = 1..N$. N cells are under test, the threshold for each cell is generated by a function on a set D_i consisting of M reference cells.*

cells D_i. The reference set is usually chosen as a set of cells in the neighborhood of the cell under test. A guard zone around the cell under test is sometimes included in order to handle the effect of extended target images or densely spaced targets [8]. The implementation of function $f(D_i)$ can be divided into two main classes, ordered statistics CFAR (OS-CFAR) and cell averaging CFAR (CA-CFAR).

A CA-CFAR system is defined by the following equation

$$T_i = f(D_i) = \frac{\alpha}{M} \sum_{k=1}^{M} y_k^i \tag{2.4}$$

where α is a design parameter commonly used to control the mean false alarm rate P_{FA}. For a scenario where all the cells have a Rayleigh distribution given as

$$f_{x_i}(x) = \frac{x}{\mu^2} \exp\left(-\left(\frac{x^2}{2\mu^2}\right)\right) \tag{2.5}$$

and square law detection is applied in the system, then the mean clutter density is shown for instance in [9] to be given by

$$P_{FA} = \left(1 + \frac{\alpha}{M}\right)^{-M} \tag{2.6}$$

An OS-CFAR algorithm is based on constructing the ordered set $D^{i\prime} = \left\{y_{(1)}, y_{(2)}, ..., y_{(M)}\right\}$ by rearranging the elements of D^i arranged such that $y_{(1)}^i \leq y_{(2)}^i \leq ... \leq y_{(M)}^i$. The function $f(D_i)$ is then given by the integer parameter K, $1 \leq K \leq M$, and the parameter α and the following equation

$$f(D_i) = \alpha y_{(K)}^i. \tag{2.7}$$

In [8], it was shown that the mean clutter density or mean false alarm rate for a OS-CFAR system with square law detection and cells with Rayleigh distribution was the following expression

$$P_{FA} = K\binom{M}{K} \frac{(K-1)!\,(\alpha + M - K)!}{(\alpha + M)} \tag{2.8}$$

[10] derived that the corresponding mean false alarm rate for a system where all the cells had a Weibull distribution given by

$$f_{x_i}(x) = \frac{\gamma}{\mu}\left(\frac{x}{\mu}\right)^{\gamma-1} \exp\left(-\left(\frac{x}{\mu}\right)^{\gamma}\right) \tag{2.9}$$

and square law detection was applied on a OS-CFAR configuration. The mean false alarm rate was then shown to be given by

$$P_{FA} = \frac{M!}{(M-K)!} \frac{\Gamma\left(\alpha^{\gamma/2} + M - K + 1\right)}{\Gamma\left(\alpha^{\gamma/2} + M + 1\right)} \tag{2.10}$$

where γ is the shape factor of the Weibull distribution. [10] also extended CFAR to incoherent integration over several scans. In [11], similar results were derived for K-distributed clutter in a CA-CFAR system.

A number of different varieties of the CFAR algorithms described above has also been proposed and described in the literature, as for instance the CA - greatest of - CFAR algorithm described in [8], where the largest average from two reference sets is chosen. However, the analysis in the present work is restricted to the most basic OS-CFAR and CA-CFAR algorithms.

Clutter density as random variable

As argued in *paper one*, the threshold for each cell under test, T_i, is a function of a set of random variables at each scan, and is thus also a random variable itself. Given T_i and f_{x_i} the probability of false alarm in cell i is given exactly by the equation

$$p_i = P\left(x_i \geq T_i | T_i\right) = P\left(I_i = 1 | T_i\right) = \int_{T_i}^{\infty} f_{x_i}(x) dx, \tag{2.11}$$

where p_i is defined on the interval $[0, 1]$. This was named the instantaneous false alarm rate in *paper one*, but is named clutter density in this chapter in order to avoid confusion with the commonly applied expression *false alarm rate*, which is often used for P_{FA}. In *paper one*, the probability density function (pdf) of p_i is derived for different CFAR configurations. This is accomplished by first deriving the pdf of the threshold T_i using the pdf of the reference cells and the function $f\left(D_i\right)$. The pdf of p_i, $f_{p_i}\left(x\right)$, can then be derived using the function in equation (2.11). By this approach, a pdf is derived for Rayleigh noise in a CA-CFAR system, and the result in equation (2.6) is confirmed by calculating the mean value, $\bar{p} = \int_0^1 x f_{p_i}\left(x\right) dx$. An expression for of the variance of p_i is also derived,

$$\sigma_p^2 = var(p_i) = \int_0^1 \left(x - E(p_i)\right)^2 f_{p_i}(x) dx = \left(\frac{2\alpha}{M} + 1\right)^{-M} - \left(\frac{\alpha}{M} + 1\right)^{-2M} \tag{2.12}$$

For a OS-CFAR system where linear detection is applied on cells with Weibull noise, the corresponding mean and variance are derived, and the expressions are given by the following two equations

$$\bar{p} = \frac{\Gamma(M+1)\Gamma(M-K+\alpha^\gamma+1)}{\Gamma(M-K+1)\Gamma(M+\alpha^\gamma+1)} \tag{2.13}$$

$$\begin{aligned} \sigma_p^2 = \Gamma(M+1) \cdot \big\{ & \Gamma(M-K+2\alpha^\gamma+1)\Gamma(M-K+1)\Gamma(M+\alpha^\gamma+1)^2 \\ & -\Gamma(M+1)\Gamma(M-K+\alpha^\gamma+1)^2\Gamma(M+2\alpha^\gamma+1)\big\} / \\ & \big\{\Gamma(M-K+1)^2\Gamma(M+2\alpha^\gamma+1)\Gamma(M+\alpha^\gamma+1)^2\big\} \end{aligned} \tag{2.14}$$

The mean and variance are independent of the Weibull scale parameter μ, but depend on the shape parameter γ and the parameters α and K.

Confirming equation (2.10), the pdf could also be derived for a OS-CFAR applying square

law detection on Weibull noise. The variance could then be shown to be given by.

$$\sigma_p^2 = \Gamma(M+1)\cdot\Big\{\Gamma(M-K+2\alpha^{\gamma/2}+1)\Gamma(M-K+1)\Gamma(M+\alpha^{\gamma/2}+1)^2 \qquad (2.15)$$
$$-\Gamma(M+1)\Gamma(M-K+\alpha^{\gamma/2}+1)^2\Gamma(M+2\alpha^{\gamma/2}+1)\Big\}\,/$$
$$\Big\{\Gamma(M-K+1)^2\Gamma(M+2\alpha^{\gamma/2}+1)\Gamma(M+\alpha^{\gamma/2}+1)^2\Big\}$$

The mean and variance for a OS-CFAR system with Rayleigh noise can be derived by inserting $\gamma = 2$ in equations (2.13), (2.14), and (2.15).

2.1.2 CFAR Loss

CFAR loss is often defined as the increase in SNR needed to maintain the mean probability of detection for a given target in a CFAR system compared to that of ideal detection with a constant threshold. In [9], a Swerling I or II target was used to derive the CFAR loss for a CA-CFAR system and Rayleigh noise. The measure average decision threshold (ADT) was introduced in [8], which is defined as the average detection threshold divided by the average noise power which is independent of the distribution of the target signal. This measure is then approximated to be proportional to the increase in SNR needed to maintain a constant probability of detection. Variations in the parameter α needed to keep a given mean false alarm rate for a given noise distribution was introduced as a measure of CFAR loss in [11]. This measure is independent of the target distribution, but is not very intuitive and it is also hard to compare the measure for different system configurations.

The variance of the false alarm rate, σ_p^2, is clearly related to the ADT measure introduced in [8], as it is a function of the distribution of the generated threshold as well as the distribution of the cell under test. As argued in *paper one*, σ_p^2 is a useful parameter when examining the performance of a CFAR system. It may be linked directly to CFAR loss in the same manner as the ADT measure, but it may also be used as a measure of the variations in the expected false alarm rate in a given CFAR configuration. An illustration is given in figure 2.3 where σ_p^2 is plotted for an OS-CFAR system as a function of the parameter K. It is shown how the variance is comparable for $K = 15..20$ and lowest for $K = 19$ in this case.

2.2 Estimation of clutter density

2.2.1 Assumptions

Several different estimators of the clutter density were introduced in *paper one*, all of which were based on the assumption that the number of false alarms were given by a binomial distribution,

$$P(m_k = k|p) = \binom{M}{k} p^k\,(1-p)^{M-k} \qquad (2.16)$$

where m_k is the number of declared measurements at t_k. The mean and variance of the binomial distribution given the parameter p are given by $E(m_k|p) = Mp$ and $\mathrm{var}(m_k|p) = Mp(1-p)$. The binomial distribution arise from the sum of M independent Bernoulli trials with the probability p of success, $P\,(I_i = 1) = p$ for all i. This implicitly restricts the configurations where the estimators can be applied.

Firstly, the same random threshold has to be applied to all the cells in the volume. This configuration is sometimes applied in radar surveillance systems. The generated threshold can

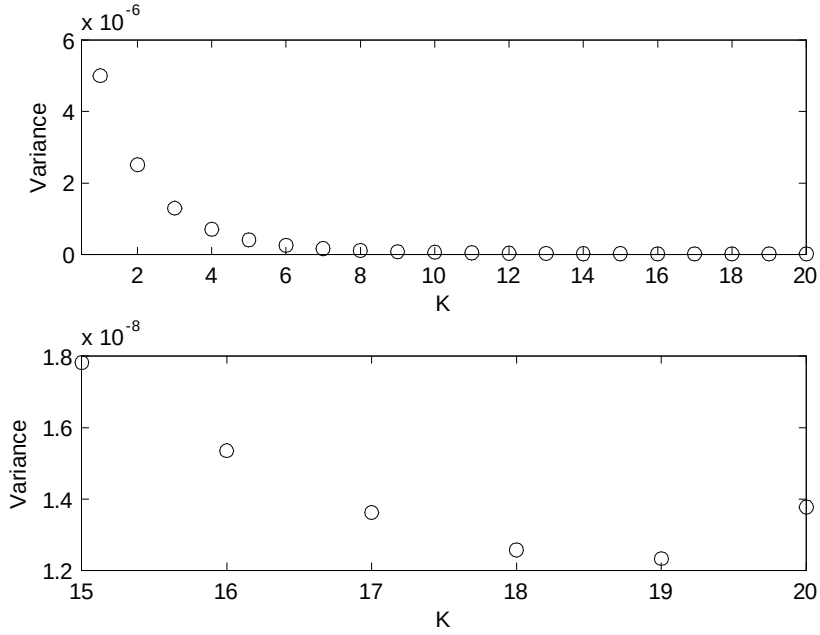

Figure 2.3: *Plot of σ_p^2 as function of K for OS-CFAR configuration, cells with Rayleigh distribution. $M = 20$, $E(p_i) = P_{FA} = 10^{-5}$. Plot K=1..20 (top), detail K=15-20 (below).*

then be made statistically independent of the cells under test by generating it from another set of cells. Secondly, the noise in each cell needs to be independent, $f_{x_i x_j}(x_i, x_j) = f_{x_i}(x_i) f_{x_j}(x_j)$ for all i and j, which means that no spatial or temporal correlation may exist. Systems where the cell under test and reference set of cells are used as a sliding average as illustrated in figure 2.4, where neighbor cells may appear in each other reference sets, do not fulfill these requirements. In general the Bernoulli trials in two neighbor cells will not be independent if they use some of the same cells as reference cells, and it is hard to derive a parameterized probability density function for this kind of system.

2.2.2 Bayesian and classical estimation

In Bayesian estimation, the estimate is based on the posterior density $f(x|z)$ which is obtained using Bayes' law and given by the following equation, where $f_x(x|z)$ is the posterior density of the estimatee, $f_z(z|x)$ is the likelihood function for the measurements given x and $f_x(x)$ is the prior pdf of the estimatee.

$$f_x(x|z) = \frac{f_z(z|x) f_x(x)}{f_z(z)} = \frac{f_z(z|x) f_x(x)}{\int f_z(z|x) f_x(x) dx} \tag{2.17}$$

A prior density $f_x(x)$ thus needs to be available in order to obtain an estimate. In contrast, the estimatee is modeled as a completely unknown constant or an unknown time varying parameter in classical estimation, and no prior information is applied. In the application considered in this chapter, assuming that the clutter density is constant and equal to P_{FA} may be considered to

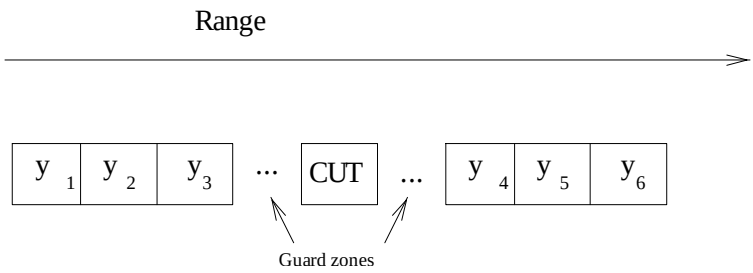

Figure 2.4: *Illustration of system where cell under test (CUT) is moved in range direction, using cells on both sides as reference sets to estimate the background and calulcate the threshold.*

be a classical estimator, while the presented linear Bayesian are the Bayesian counterparts. As discussed in *paper one*, the applied empirical Bayesian estimators may be considered to be a compromise between classical and Bayesian estimation, in the sense that no prior information about the estimatee is needed because it is estimated from past data.

2.2.3 MMSE and BLUE estimators

Based on the posterior density, an estimate of x can be obtained in several different ways. The minimum mean square error estimator (MMSE) can be shown to minimize the square error function given by

$$\hat{x}^{MMSE} = \arg\min_{\hat{x}} E\left((\hat{x}-x)^T(\hat{x}-x)\right) \tag{2.18}$$

The MMSE estimator is given by the conditional mean [12]. The MMSE estimator and its covariance are given by the following equations.

$$\hat{x}^{MMSE} = E(x|z) = \int x f_x(x|z)dx \tag{2.19}$$

$$\hat{P}^{MMSE} = \mathrm{cov}(x|z) = \int (x - E(x|z))(x - E(x|z))^T f_x(x|z)dx \tag{2.20}$$

A closed form solution of equation (2.19) is often hard to obtain, and the best linear unbiased estimator (BLUE) is hence a tractable alternative. The notation linear minimum mean square error estimator (LMMSE) was applied in *paper one*, but the more widely used BLUE notation is adapted in this thesis, also in order to be consistent with paper four. The BLUE estimator minimizes the quadratic cost function by a linear function of the measurement z, as given by the following equation.

$$\hat{x}^{BLUE} = \arg\min_{\hat{x}=Az+b} E\left((\hat{x}-x)^T(\hat{x}-x)\right) \tag{2.21}$$

The BLUE estimator is given by [12]

$$\hat{x}^{BLUE} = \bar{x} + C_{xz}C_z^{-1}(z-\bar{z}) \tag{2.22}$$

$$MSE(\hat{x}^{BLUE}) = C_x - C_{xz}C_z^{-1}C_{zx} \tag{2.23}$$

where $\bar{x}$ is the prior mean of the estimatee, $C_{xz} = E\left((x-\bar{x})(z-\bar{z})^T\right) = C_{zx}^T$ is the covariance between the estimatee and the measurements, $C_z = \left((z-\bar{z})(z-\bar{z})^T\right)$ is the measurement mean square error (MSE), and $\bar{z}$ is the measurement mean. The notation MSE is applied rather than covariance because the BLUE estimator is not a conditional mean [12].

The BLUE estimator has the advantages that it only depends on the first two moments of the estimatee, it is unbiased $E(x-\hat{x}) = 0$, and it is the best in the mean square error sense within the class of linear estimators. Among its other beneficial properties is that for the case that x and z are jointly Gaussian, the BLUE estimator coincides with the conditional mean, and is hence the optimal estimator in the sense that it minimizes equation (2.18). In this case, its conditional MSE coincides with its unconditional MSE, $MSE\left(\hat{x}^{BLUE}|z\right) = MSE\left(\hat{x}^{BLUE}\right) = \hat{P}^{MMSE}$.

The BLUE estimator for the case that the likelihood function is given by the binomial distribution in equation (2.16) was derived in *paper one*, and is given by the two following equations, where p and σ_p^2 is the prior mean and variance of the clutter density.

$$\begin{aligned}\hat{x} &= \bar{x} + C_{xz}C_z^{-1}(z-\bar{z}) \\ &= \bar{p} + \frac{\sigma_p^2}{\bar{p}(1-\bar{p}) + (N-1)\sigma_p^2}(m_k - N\bar{p})\end{aligned} \tag{2.24}$$

$$MSE(\hat{x}) = C_x - C_{xz}C_z^{-1}C_{zx} = \sigma_p^2\left(\frac{\bar{p}(1-\bar{p}) - \sigma_p^2}{\bar{p}(1-\bar{p}) + (N-1)\sigma_p^2}\right) \tag{2.25}$$

2.2.4 Gain

In *paper one*, the gain of estimating the clutter density at each scan was defined by G given by the following equation.

$$G = \left[\frac{\sigma_p^2}{MSE(\hat{x}^{BLUE})}\right]_{dB} \tag{2.26}$$

By making the assumption that the gain is constant and equal to P_{FA}, then the error covariance is given by $E(p_i - P_{FA})^2 = \sigma_p^2$. The gain G is thus a measure of the accuracy of an estimator which assumes that $p_i = P_{FA}$, compared to that of the BLUE estimator. This gain is calculated as

$$G = 10\log_{10}\left(\frac{\bar{p}(1-\bar{p}) + (N-1)\sigma_p^2}{\bar{p}(1-\bar{p}) - \sigma_p^2}\right)$$

in this chapter, as both the enumerator and denominator are squared values, while $20\log_{10}(A)$ was used in *paper one*. The gain was plotted in *paper one* as a function of number of cells N in an CA-CFAR system with Rayleigh noise (figure 4), as function of the parameter K in an OS-CFAR system with $N = 20$ and Weibull noise (figure 5), and as function of N in an OS-CFAR system with $K = N - 3$ (figure 6). Choosing linear or square law detection does not influence these results, as P_{FA} in equation (2.13) and (2.10) are determined by the ratio α^γ and $\alpha^{\gamma/2}$ respectively. The relationship between α and γ is fixed as α^γ is constant for a given false alarm rate. Assuming that α is used to keep P_{FA} constant and solving equation (2.6) for α gives

$$\alpha = N\left(P_{FA}^{-1/N} - 1\right) \tag{2.27}$$

Inserting this into equation (2.12) gives

$$\sigma_p^2 = \left(\frac{2\alpha}{N}+1\right)^{-N} - \left(\frac{\alpha}{N}+1\right)^{-2N} = \left(2P_{FA}^{-1/N}-1\right)^{-N} - P_{FA}^2 \tag{2.28}$$

Thus

$$\lim_{N\to\infty} \sigma_p^2 = 0 \tag{2.29}$$

which is expected because when the set of reference cells becomes large, the CFAR threshold becomes the ideal threshold. The gain can thus be written as

$$G = \frac{\sigma_p^2}{MSE(\hat{x}^{BLUE})} = \frac{P_{FA}\left(1-P_{FA}\right) + (N-1)\left(\left(2P_{FA}^{-1/N}-1\right)^{-N} - P_{FA}^2\right)}{P_{FA}\left(1-P_{FA}\right) - \left(2P_{FA}^{-1/N}-1\right)^{-N} + P_{FA}^2} \tag{2.30}$$

Thus

$$\lim_{N\to\infty} G = \frac{-P_{FA}\ln^2\left(P_{FA}\right) - 1 + P_{FA}}{-1+P_{FA}} = 1 + \frac{P_{FA}\ln^2\left(P_{FA}\right)}{1-P_{FA}} \tag{2.31}$$

This expression provides an explanation why the different curves in figure 4 of *paper one* converged to different values, as they represented different mean false alarm rates. Also, by estimating the gain of information in the sense of Fisher by using the BLUE estimator compared to using P_{FA} ,

$$\begin{aligned}\Delta I &= MSE\left(\hat{x}^{BLUE}\right)^{-1} - \sigma_p^{-2} = \left(\frac{N}{E\left(p\right)\left(1-E\left(p\right)\right) - \sigma_p^2}\right) \\ &= \frac{N}{P_{FA} - \left(2P_{FA}^{-1/N}-1\right)^{-N}} \overrightarrow{N\to\infty} \frac{N}{P_{FA}\left(1-P_{FA}\right)}\end{aligned} \tag{2.32}$$

The added information per cell in the sense of Fisher is thus given by approximately $\left(P_{FA}\left(1-P_{FA}\right)\right)^{-1}$ which explains the difference in the rates of convergence for the different mean false alarm rates, as the information added in each cell is larger for a low false alarm rate.

2.2.5 Empirical Bayesian estimation

The estimator given in section 2.2.3 depended on being able to calculate the mean and variance of the clutter density analytically or numerically. Accurate knowledge of the distribution of each cell is in many cases unrealistic, as the distribution may vary over time and space and sufficient knowledge about the distribution of each cell may be unavailable. This is the background of why Empirical Bayesian estimation was introduced in *paper one*, in order to avoid being dependent on exact knowledge about the distributions $f_{x_i}\left(x\right)$ or P_{FA} and σ_p^2.

As discussed in *paper one*, the term Empirical Bayes (EB) estimation was introduced by Robbins [13], and is based on Bayesian estimation but assumes that the prior distribution of the estimatee can be estimated from previous measurements. The prior distribution is thus modeled as a random variable, but given a frequentist interpretation in the sense that its prior distribution can be observed and estimated using classical estimation methods [14]. A representation of the main principle of EB estimation is shown in table 2.1. Previous measurements z_1 to z_{l-1} are used to extract information about the prior distribution $f_x\left(x\right)$, and this estimate is then applied to make

an estimate $\hat{x}_l$ based on the measurement z_l. As discussed in *paper one*, empirical estimators are often divided into two classes, parametric and nonparametric, where the parametric approach assumes that the prior distribution belongs to a given class of distributions. In the nonparametric approach, no such assumption is made, but the prior density is estimated using the expression $\hat{f}(z) \approx \int f(z|x)\hat{f}(x)dx$. In many cases, no explicit estimate of $\hat{f}(x)$ is needed in order to obtain an estimate $\hat{x}_l$, [15]. .

Table 2.1: *Organization of data in empirical Bayesian approach*

	Past data			**Current data**
Realizations	x_1	...	x_{l-1}	x_l
Measurements	z_2	...	z_{l-1}	z_l

2.2.6 Linear empirical Bayesian estimation (LEB)

Linear EB estimators is a class of nonparametric EB estimators which is based on estimating the two first moments of the measurement distribution $f(z)$. Robbins derived a general scalar estimator in [16], which can be generalized to a vector case by equation (2.35) [15]. If likelihood function $f_z(z|x)$ satisfies the following two equations

$$E(z|x) = x \tag{2.33}$$

$$\text{cov}(z|x) = A + bx^T + xb^T + axx^T \tag{2.34}$$

where A, b and a are constants, then the LEB estimator can be written as

$$\hat{x}_k^{LEB} = \hat{z} + \frac{1}{1+a}\left(I - \left(\hat{\sigma}^2\right)^{-1}\left(A + b\hat{z}^T + \hat{z}b^T + a\hat{z}\hat{z}^T\right)\right)\cdot(z_k - \hat{z}) \tag{2.35}$$

where $\hat{z}$ and $\hat{\sigma}^2$ is the sample mean and covariance of the past data.

LEB estimator for binomial distribution

A derivation of a LEB estimator for the binomial distribution is given in *paper one*, based on [16] and [15]. This estimator is the LEB estimator for all likelihood functions where $E(m_k|p) = p$ and $\text{var}(m_k|p) = p(1-p)$. The estimator is given by

$$\hat{p}_k^{LEB} = \hat{z} + \frac{N}{N-1}\left(1 - \frac{\hat{z}(1-\hat{z})}{N\hat{\sigma}^2}\right)\left(\frac{m_k}{N} - \hat{z}\right) \tag{2.36}$$

where m_k is number of declared measurements at time t_k, and $\hat{z}$ and $\hat{\sigma}^2$ are the sample mean and variance of the past measurements divided by N. An additional scalar estimator derived in [17] was presented in *paper one*, but the convergence properties of the estimator in equation (2.36) were found to be equal or comparable to those of the estimator in [17] in the performed Monte Carlo simulations. Equation (2.36) was thus used, as it is more computationally efficient.

It is possible to derive empirical estimators of the mean square error of the estimator in equation (2.36) which also is based on the sample mean and variance of the obtained measurements. However, this estimator was shown to be sensitive to the variances of the sample mean and variance, and thus was demonstrated to use a large number of measurements to converge to the actual $MSE\left(\hat{p}_l^{LEB}\right)$. This was examined through Monte Carlo analyses.

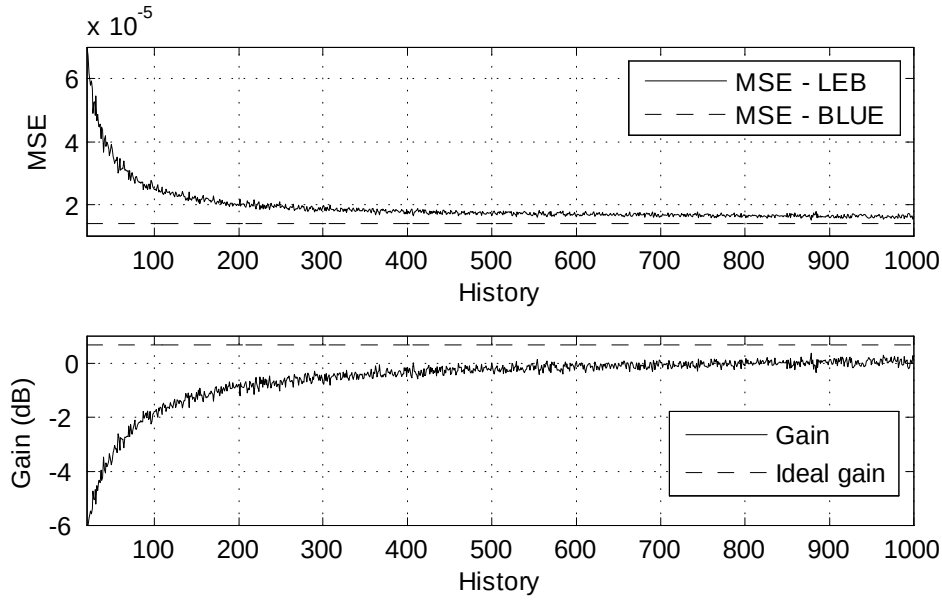

Figure 2.5: *Convergence of MSE of LEB estimator. CA-CFAR system with* $N = 10$ *and Rayleigh noise.* $P_{FA} = 10^{-3}$*. Monte Carlo simulations with* 10^6 *runs.*

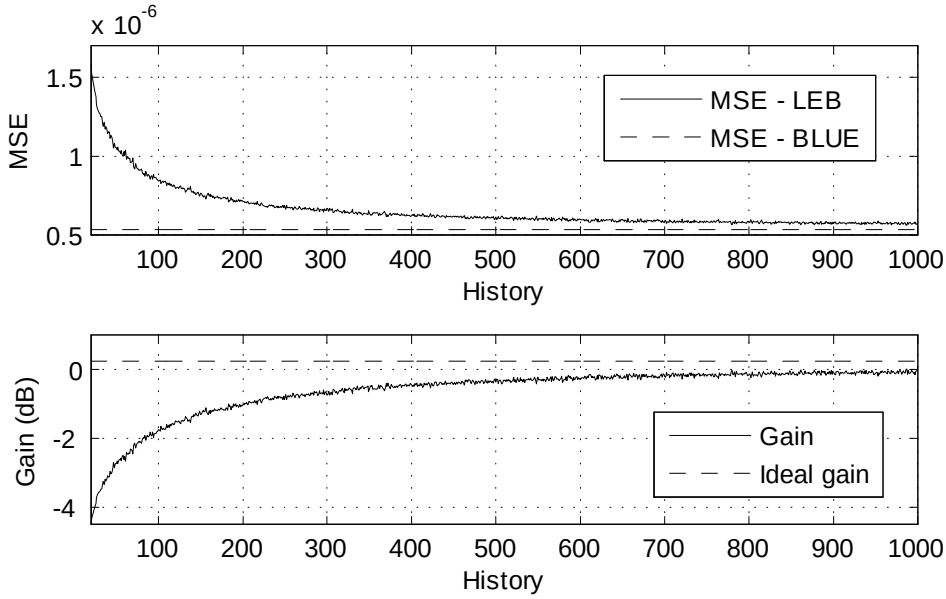

Figure 2.6: *Convergence of MSE of LEB estimator. CA-CFAR system with* $N = 100$ *and Rayleigh noise.* $P_{FA} = 10^{-3}$*. Monte Carlo simulations with* 10^5 *runs.*

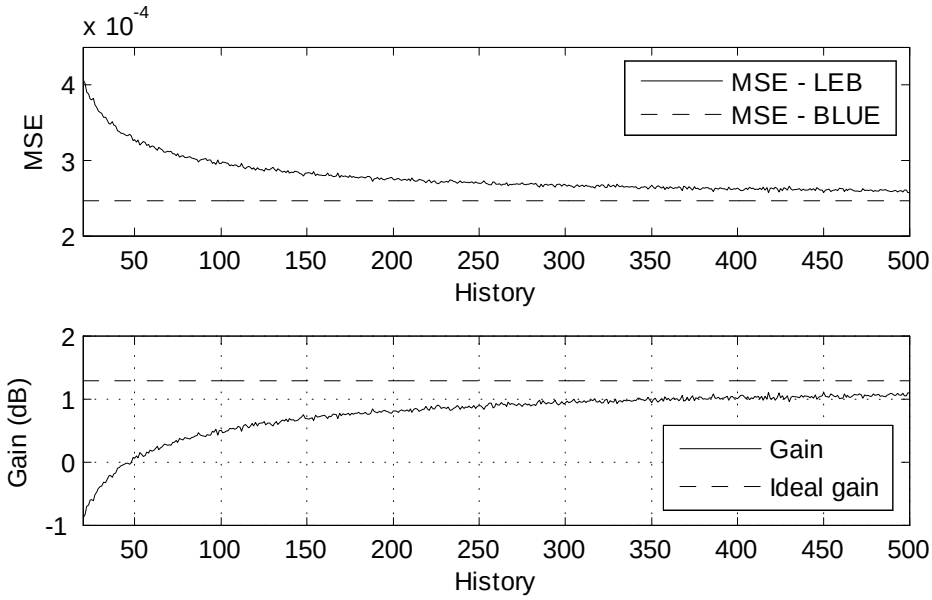

Figure 2.7: *Convergence of MSE of LEB estimator. CA-CFAR system with* $N = 10$ *and Rayleigh noise.* $P_{FA} = 10^{-2}$*. Monte Carlo simulations with* 10^6 *runs.*

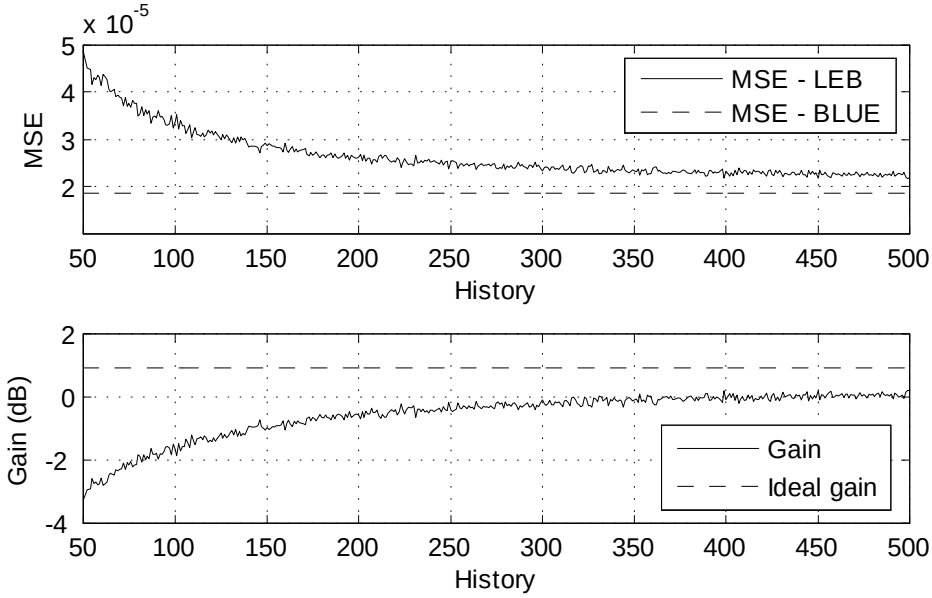

Figure 2.8: *Convergence of MSE of LEB estimator. OS-CFAR system with* $N = 10$ *and Rayleigh noise.* $P_{FA} = 10^{-3}$*. Monte Carlo simulations with* 10^6 *runs.*

Figure 3 in *paper one* shows how the MSE of the LEB estimator converges to that of the corresponding BLUE estimator for a CA-CFAR configuration. However, the figure was generated by drawing p from a truncated Rayleigh distribution, and with a relatively large N of 10^3 cells. Figures 2.5, 2.6, and 2.7 show similar convergence curves for several other cases, using a CA-CFAR configurations. The threshold in these figures was generated by a gamma distribution, $T \sim Gamma(N, \frac{\alpha\lambda}{N})$ using the results derived in *paper one* while x_i were generated using the exponential distribution $x_i \sim Exponential(\lambda)$. In figure 2.8, the convergence curve for a OS-CFAR configuration is shown. A set of reference cells was used to generate the threshold at each scan, as it was found to be more computationally demanding to generate the thresholds from the derived pdf of the threshold.

In general, the LEB estimators converge to the corresponding BLUE estimators [14], but as illustrated in figures 2.5, 2.6, 2.7, and 2.8, the rate of convergence may vary for different system configurations and needs to be examined for each case. For the CA-CFAR systems, the point where the gain becomes larger than zero was found to depend mostly on P_{FA} rather than on N. For $P_{FA} = 10^{-2}$, G was positive after ~50 scans, whereas for $P_{FA} = 10^{-3}$ it was positive around 800-1000 scans, and G was shown to be larger than 0 after ~5000 scans when $P_{FA} = 10^{-4}$. For the SO-CFAR system with $P_{FA} = 10^{-3}$, as shown in figure 2.8, the estimator converged faster than for the CA-CFAR estimator with the same mean false alarm rate.

3

Extended targets in surveillance radar applications

THIS chapter further extends the work presented in *paper two*, *paper three,* and *paper four*, in the sense that the simulation setup introduced in *paper three* is described in further detail, while some background material from *paper two* and *paper three* is included for clarity. Some additional simulation results are then presented in appendix A. This chapter also contains a discussion of the applied signal processing and tracking methods compared to previously published methods for tracking extended targets, extending the work in *paper two*. A justification of the state dependent bias models proposed in *paper four* is also presented.

3.1 Tracking extended targets

The work described in *paper three* focused on deriving error models for radar surveillance systems, where the signal processing is implemented using centroid processing as outlined in *papers two* and *paper three*. To cluster detected pixels and compute the cluster centroid as presented in [18] is computationally efficient. This is important in a radar surveillance system where a large amount of data needs to be processed and a high number of targets may be present. However, information that potentially could be used to improve the accuracy of the tracking system is discarded when the image centroid is used as the only input to the tracking algorithm. Methods developed for group tracking could potentially be used in order to utilize information in the target image. An extensive review of group tracking approaches as well as a classification of different variants of group tracking can be found in [19], where group tracking is defined as tracking a cluster of closely spaced objects. A first class of group trackers was for instance described in [20], where the centroid of a cluster is tracked without retaining individual tracks for the objects in the cluster. In [20], one tracking filter is implemented for the centroid using a standard tracking filter approach, while a separate filter is defined to track the extent of the cluster. The state vector of the extent filter is defined as the six dimensional vector

$$x = \left[\sigma_x^2, \sigma_{xy}^2, \sigma_{xz}^2, \sigma_y^2, \sigma_{yz}^2, \sigma_z^2\right]^T \tag{3.1}$$

The target extent is then defined as given by the volume

$$\delta x^T R^{-1} \delta_x \leq \beta \tag{3.2}$$

$$R = \begin{bmatrix} \sigma_x^2 & \sigma_{xy}^2 & \sigma_{xz}^2 \\ \sigma_{xy}^2 & \sigma_y^2 & \sigma_{yz}^2 \\ \sigma_{xz}^2 & \sigma_{yz}^2 & \sigma_z^2 \end{bmatrix} \tag{3.3}$$

It is argued in [20] that the same approach could be used for an extended target. This setup could be directly adapted to the 2D tracking applications considered in this thesis, with some restrictions. The second filter, estimating the extent of the target, would not improve the RMSE of a single target filter, but it may be used for other purposes. The estimated target image extent could potentially be used by the tracking algorithm to improve data association in a multi target or cluttered environment, similar to how target amplitude was used in [21]. However, using image extent in a multi sensor environment as outlined in [20] may prove to be problematic as the image is a function of the target sensor geometry for each sensor. Large differences may thus appear in the target images generated by sensors at different locations. In addition, the problem of one group or cluster dissolving into smaller clusters is not relevant for an extended target image, but is an important element in the group tracking approach.

In [22] and [23], the extent of the group target was modeled and estimated using random matrices. The estimated object extension is assumed to have an inverse Wishart density given by

$$f_{X_k}(X_k|Z_k) = \mathcal{IW}\left(X_k; \hat{\nu}_k, \hat{X}_k\right) \propto |X_k|^{-\frac{\hat{\nu}_k}{2}} \exp\left(trace\left(-\frac{1}{2}\hat{X}_k X_k^{-1}\right)\right) \tag{3.4}$$

where ν_k is a parameter of the inverse Wishart distribution, and its estimate at each step is given by $\hat{\nu}_k$. The notation $\hat{x}_k$ is in this thesis defined as the estimate of the random variable x at time k, utilizing all measurements up to, and including time k. By assuming appropriate system models for X_k and ν_k, it is shown that the predicted density of the extension is given by a Wishart density function, as

$$\begin{aligned} f_{X_k}(X_k|X_{k-1}) &= \mathcal{W}\left(X_k; \bar{\delta}_k, \frac{X_{k-1}}{\bar{\delta}_k}\right) \\ &\propto |X_{k-1}|^{-\frac{\bar{\delta}_k}{2}} |X_k|^{-\frac{\bar{\delta}_k - d - 1}{2}} \exp\left(trace\left(-\frac{1}{2}\bar{\delta}_k X_k X_{k-1}^{-1}\right)\right) \end{aligned} \tag{3.5}$$

where $\bar{\delta}_k$ is a parameter chosen as $\bar{\delta}_k = \delta \exp(T/\tau)$, T is the sampling interval, and τ and δ are spatial evolution parameters. The notation $\bar{x}_k$ is in this thesis defined as the predicted variable, or as the estimate of the variable x at time k utilizing all measurements up to and including time $k-1$. The predicted kinematical state of the target is assumed to be dependent on the target state, as

$$f_{x_k}(x_k|X_k, Z_{k-1}) = \mathcal{N}\left(x_k; \bar{x}_k, \bar{P}_k \otimes X_k\right) \tag{3.6}$$

$\otimes$ indicates a Kronecker product, defined by

$$A \otimes B = \begin{bmatrix} a_{11} \cdot B & a_{12} \cdot B & \cdots & a_{1n} \cdot B \\ a_{21} \cdot B & a_{22} \cdot B & & \\ \vdots & & \ddots & \\ a_{m1} \cdot B & & & a_{mn} \cdot B \end{bmatrix}$$

The cluster or group target is assumed to be constructed by n_k independent measurements originating from the cluster, and measurements of the centroid and target extent are defined by

$$z_k = \frac{1}{n_k} \sum\nolimits_{j=1}^{n_k} z_k^j$$
$$E_k = \sum\nolimits_{j=1}^{n_k} \left(z_k^j - z_k \right) \left(z_k^j - z_k \right)^T$$

Based on a derived likelihood function, the jointly posterior pdf is derived using a Bayesian framework and shown to be given on the form

$$f_{x_k, X_k} \left(x_k, X_k | Z^k \right) = \mathcal{N} \left(x_k; \hat{x}_k, \hat{P}_k \otimes X_k \right) \mathcal{IW} \left(X_k; \hat{\nu}_k, \hat{X}_k \right)$$

where Z^k is the set of all measurements up to time k. Simple recursive equations are then derived for the prediction and estimation for both the target extent and the kinematic state.

The methods derived in [22] and [23] could potentially be adapted to the considered application by defining each pixel as a measurement, even though the assumptions made to derive the likelihood function may be violated. The simple recursive structure of the derived filter would not imply an increase in computational load compared to the methods presented in *paper two* and *paper four*. However, the assumptions imposed on the system by assuming that the predicted kinematic state is a function of target extent do not transfer easily to an extended target image scenario, where the shape of the image depends on the kinematic state. This framework may thus be more suitable for extended objects consisting of many individual objects, where it may be possible to make considerations on the kinematics of the group objects based on the shape of the cluster.

A second class of group tracking is also defined in [19], where tracks of individual objects in a cluster as well as the cluster information are retained. A general formulation of this approach can be found in [24], where a point matching algorithm is proposed in order to solve the problem of associating measurements in the cluster with individual tracks. A similar approach based on tracking the position of points on an object in a sequence of video images was presented in [25]. In [26], a Bayesian multiple hypothesis approach is implemented using particle filters, and the Bayesian particle filter approach is further investigated in [27]. For 2D surveillance radars, experience shows that the speckle noise and other noise components present in the target images makes it hard to identify individual features on the targets. As discussed in *paper two*, surveillance systems will often be optimized to detect targets, and not to measure the amplitude of peaks in the target image. Tracking of individual reflectors, like for instance corner reflectors, will often be hard or impossible, as indicated in figure 1.1. This approach could, however, be feasible for instance when considering the resolution and image quality of the ISAR images presented in [28].

Another approach was described in [29], where it is assumed that a measurement of the length and width of the target is available as measurements. This approach is not applicable for the surveillance radar applications considered in this thesis, as the width and length of the target image may differ and in worst case be uncorrelated with the dimensions of the target. There may also be significant speckle noise in the target image from scan to scan, creating measurement errors of large magnitudes.

The work in [30] introduced a measurement model which was applied in a track before detect filter in [31], where measurements originated from the target are assumed to be independent and have a spatial Poisson distribution over a target region. This approach was not considered because of two main reasons. Firstly, the track before detect approach is extremely computationally

expensive, which does not fit in well with a high data rate and high target number surveillance application. Secondly, assuming that the measurements are given as clustered pixels, the spatial Poisson distribution in general will not be correct.

3.2 Position measurement error models

In the following subsections, alternatives to the Monte Carlo simulations described in *paper two* and *paper four* are discussed, and a justification is given for the state dependent biases proposed in *paper four*.

3.2.1 Radar position error modeling

As discussed in *paper two* and *paper three*, it is common to assume that range measurement errors are independent from bearing and elevation measurement errors when radar position measurements are included in a tracking system. Assuming that the measurement consists of an angle (bearing) and range measurement, the measurement vector at time t_k and its covariance can be written as

$$z_k = \left[\begin{array}{cc} r_k & \phi_k \end{array} \right]^T \tag{3.7}$$

$$C_z = \left[\begin{array}{cc} \sigma_r^2 & 0 \\ 0 & \sigma_\phi^2 \end{array} \right] \tag{3.8}$$

As shown in *paper two* and *paper three*, this assumption may fail to be true for targets that are extended relative to the resolution of the radar. Numerical values for σ_r^2 and σ_ϕ^2 need to be derived in order to apply the model in a tracking system. Models of σ_r^2 and σ_ϕ^2 based on matched filtering and a given signal to noise ratio (SNR) for selected waveforms can be found for instance in [7]. However, these models may not transfer directly to scenarios with extended targets where the target may cover several resolution cells.

An analytical approach to modeling the error statistics of radar measurements of extended targets can be found in [32]. The wandering of the apparent center of the target relative to its geometric center is named glint. The phase front is defined as the plane with constant phase in the electrical field returned from the target. The angular error of the position measurement is derived by considering the direction of phase front reflected from the target. The apparent direction of the target is normal to this phase front. A normalized measure of the angular error is defined by

$$\eta = \frac{\tan \upsilon}{\alpha_0/2}$$

where υ is the difference between the apparent target direction and the center of geometry, and α_0 is the angular extent of the target. Assuming that the returned signal of the two point targets are Rayleigh distributed, it is shown that the difference between η and its expected value, $E(\eta)$, has a student-t distribution.

The range error is defined as the group delay of the returned electromagnetic signal. By approximating the system as linear, it is shown that the normalized range error also has a student-t distribution and that the range and angular errors are independent. These results are also shown to be true for more complex, but still simplified targets, where Rayleigh point targets are distributed uniformly over a rectangular area. Barton extends these results by approximating the first lobe of the student-t distribution by a Gaussian distribution, giving that the standard deviation of the glint is given by $\sigma_g = L/3$, where L is the extent of the target [7].

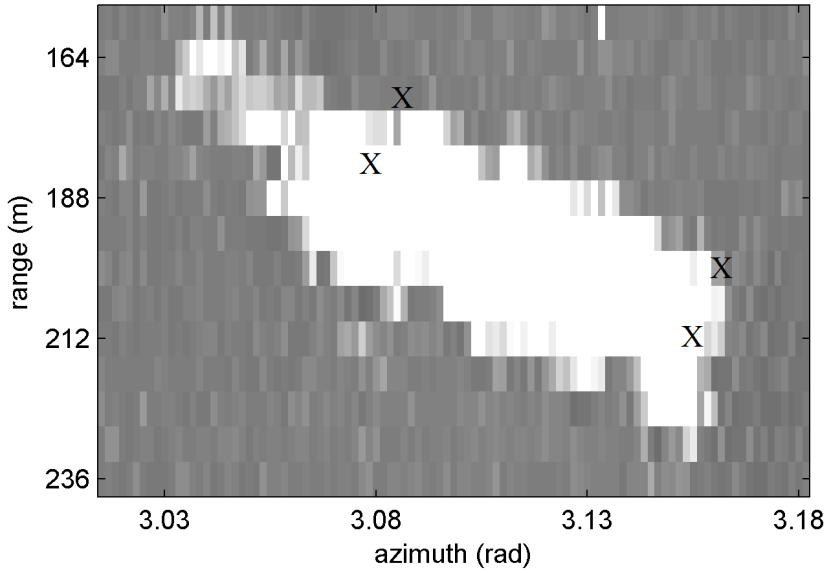

Figure 3.1: *Caption of surveillance radar image of a commercial vessel showing clutter in the wake of the vessel. The corners of the rectangular targets are marked by X. The target is moving towards lower right corner of image. Displayed with permission from Norcontrol IT.*

The models presented in [32] can not be applied directly in the target tracking systems considered in this thesis. Firstly, the errors are normalized and need to be transformed into physical units. Secondly, the effects of the signal form and processing need to be included in the calculations in a real system, as indicated in [7] and [2]. In addition, in this thesis targets that may be considerably larger than the size of the range and angular resolution of the radar are studied. Depending on the range, the targets may be covered by many resolution cells. The work in [32] does not include considerations of signal processing other than the angular response of the receiver.

As discussed in *paper three*, a second approach to derive the values of σ_r^2 and σ_ϕ^2 is described by [33], and [34] for systems applying centroid processing on image sensors. One underlying assumption in this method is that the noise in the pixels is uncorrelated, which in general will not be true for a radar image where the image may contain speckle noise. Secondly, it is assumed that the mean and variance of the pixels in the target image are known, which in many cases would be unreasonable. However, the assumption may in some cases be true for point targets where the target image may be similar to a Gaussian plume, and where the SNR can be predicted or learned from experience.

3.2.2 Measurement biases

In *paper four*, two state dependent biases were proposed which were functions of the velocity of the considered target. The first proposed bias model assumes that the bias is proportional to the

velocity vector, as

$$b^1 = K \cdot v = K \cdot [v^x, v^y]^T \tag{3.9}$$

The parameter K is then a system parameter and has units s. The second proposed bias assumes that the bias was aligned with the velocity vector, but of constant magnitude, as

$$b^2 = K \cdot \frac{v}{|v|} = K \cdot [\cos(\theta), \sin(\theta)]^T \tag{3.10}$$

The motivation for proposing this class of target dependent biases can be seen in figure 3.1, where a radar image at closed range is shown. The image clearly shows how a significant amount of clutter may be induced in the wake of the target, and it is very likely that the induced clutter may be rendered as a part of the target image by a segmentation algorithm. A bias in the backwards direction is thus generated. The amplitude of the wake and thus also the clutter may be a function of velocity, which is why the first bias is proposed. In other cases it may be reasonable to assume that the bias is constant, which can be modeled by the second bias.

The radar image shown in figure 3.1 was a result of an experiment conducted in 2005, where recorded radar images of a commercial ferry were compared to the measurements obtained from a highly accurate differential GPS system mounted on the vessel. Two differential GPS transmitters were used, each with an accuracy of ~3cm, and synchronized samples were obtained with a frequency of 1 Hz. The position and heading of the vessel could thus be obtained with a high degree of accuracy. The experiment provided a basis for analytical considerations based on the raw images, but did not record enough data to allow statistical analysis of the state dependent measurement biases. The biases seen in figure 3.1 were observed, and it was seen that clutter in the wake of the target was more likely to appear close to the radar, where the grazing angle was high.

Bias due to occlusion

The third bias proposed in *paper four*, where the bias was a function of the aspect angle, had a more heuristic justification than the two previous ones. The target sensor geometry in the experiment described above meant that metal structures and objects all over the target surface were visible at all times, making the occlusion effect smaller than in other applications. However, occlusion effects may in other cases cause significant biases in the target images. As argued in *paper four* as well as in [35], the structures on the target that contribute to the target image for a given aspect angle may be shifted from the geometrical center of the target, which may cause a bias in the measurements for small changes in the aspect angle. In *paper four*, a simple bias model was proposed that may be appropriate for cases where expected occlusion is a function of aspect angle. The bias is proposed to be given by the following expression.

$$b_k^3 = \alpha \cdot |\cos(\psi_k)| \cdot r_k / |r_k| = K \cdot |\cos(\theta_k - \phi_k)| \cdot \begin{bmatrix} \cos\phi_k & \sin\phi_k \end{bmatrix}^T \tag{3.11}$$

The expression could also be extended to include elevation angle.

As discussed in *paper four*, it is proposed to use state dependent biases in order to handle correlation between measurements at small aspect angles as an alternative to the approach described in [33] and [35], where the bias between that geometrical center of the target and the image center is estimated at each scan. The results in appendix A show that a very small change in aspect angle may produce a completely different realization of the speckle noise and hence a different target image. The offset may thus be difficult to estimate, especially if the aspect angle changes rapidly. However, for cases where two different sensors with different sensing principles

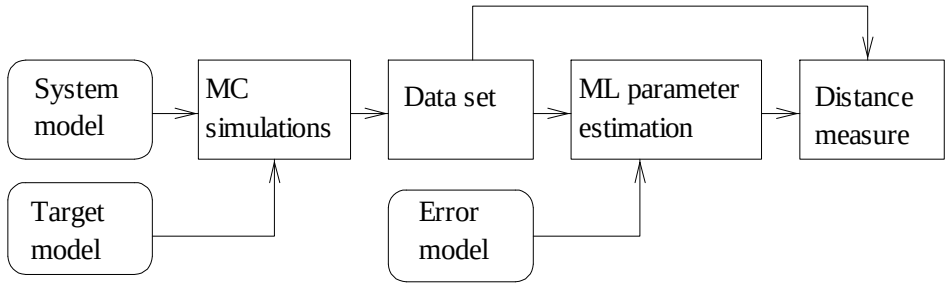

Figure 3.2: *Schematics of MC simulations.*

are fused as described in [33], different objects may contribute to the target images for each sensor, causing offsets which need to be modeled, or estimated as proposed in [35]. A bias would then be defined as an offset in the target image compared to the geometrical center of the target for each sensing principle.

3.3 Monte Carlo simulations and parameter estimation

The main aims of the work described in *paper two* and *paper three* were to examine the correlation between measurement errors of 2D surveillance radars and the aspect angle of a target, and also to develop models of these linked measurement errors that can be applied in an automated target tracking system. As discussed in *paper three* and in section 3.2, expressing the measurement error for an extended target error in a real 2D surveillance radar system analytically as it was done in [32] would be hard or impossible. The alternative approach applied in this thesis was to derive the parameter of the error models using Monte Carlo simulations, where simplified target models and system components were used to generate simulated radar images for a target with a given position and aspect angle. These generated images were then processed into range and bearing measurements using similar processing as commonly applied in 2D surveillance systems.

The main flow in the simulations can be seen in figure 3.2. Simplified and idealized models of the spatial filtering and ideal matched filtering were constructed as presented in *paper three*, and further described in the following subsections. The simulations were performed with targets consisting of a collection of point targets with fixed position relative to each other, as described in *paper three*.

The sensor target geometry was varied in a systematic manner in order to investigate the relationship between aspect angle, SNR and measurement error, as described in *paper two*, *paper three,* and *paper four*. Section 3.3.1 contains a description of the considered sensor target geometry, which is similar to many other 2D surveillance applications. Maximum likelihood estimation was then applied to fit statistical models of the measurement error to large sets of simulated measurements. A summary of the applied measurement models is found in *paper four*. The distance between the derived error model and the generated measurement set was calculated using the Kullback Leibler distance, which is described in section 3.3.8. The results and methods presented here are adapted to this specific application, but may easily be adapted to other applications by modifying the models applied in the Monte Carlo simulations.

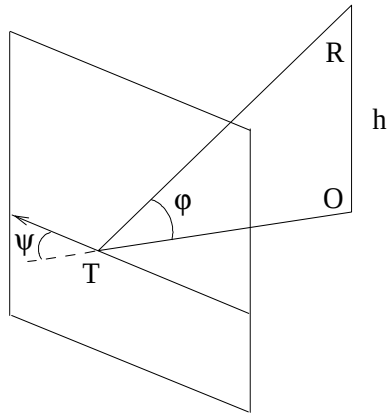

Figure 3.3: *Sensor target geometry for single sensor system. T is the position of the target, ψ is the aspect angle, φ is the elevation angle, h is the relative height of the sensor.*

3.3.1 Sensor target geometry

This thesis focus mainly on maritime surveillance systems, where the considered targets will consist mostly of ships moving at relatively low velocities. The distance between the target and the radars may vary from less than 100 meters to tens of kilometers. A general representation of the considered sensor target geometry can be seen in figures 3.3, 3.4, 3.5, and 3.6. The symbols denoting aspect angle ψ, range and bearing $\begin{bmatrix} r & \phi \end{bmatrix}^T$, and heading angle θ, will be used throughout this thesis.

Figure 3.3 shows the target sensor geometry for a single sensor where the sensor is located at the point R. The aspect angle ψ is the heading of the target with respect to the sensor. It is defined by the angle between the two planes drawn in figure 3.3. One plane is defined by the position of the radar, R , the position of the radar projected to ground level, O, and the center position of the target, T. The second plane is defined by the vertical plane through the center line or the main axis of the target.

A schematic representation of a 2D sensor-target geometry can be seen in figure 3.4. Let the sensor frame be defined in the Cartesian frame by the x and y axes, and the r and ϕ in polar coordinates. Then, let the axes x' and y' be aligned with the main axes of the target. The aspect angle of the target with respect to the sensor is then defined by the angle ψ and the heading angle of the target with respect to the x axis by

$$\theta = \phi + \psi \tag{3.12}$$

The aspect angle ψ as shown in figure 3.4 is defined as < 0. For a multi sensor scenario, the sensor target geometry is shown in figure 3.5, where the parameters of system one and two are given superscripts 1 and 2, respectively. The axes of the coordinate system defined by the main axes of the target are x' and y'. If $\Omega = 0$ and the axes of two sensors are aligned, then the heading angle with respect to the x axis in the two systems will be equal, $\theta = \theta^2$.

The radars applied in maritime surveillance applications will often be located at a height h above the surface, as illustrated in figure 3.3 and figure 3.6. This creates a bias $\Delta = \rho - r$ between the assumed polar or cylindrical frame and actual range. The measured distance is given by ρ, while the distance in the cylindrical reference frame is given by r. The bias is negligible

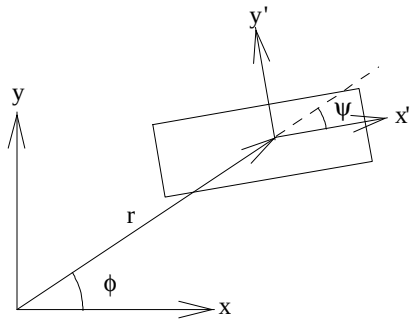

Figure 3.4: *Single sensor 2D sensor target geometry.*

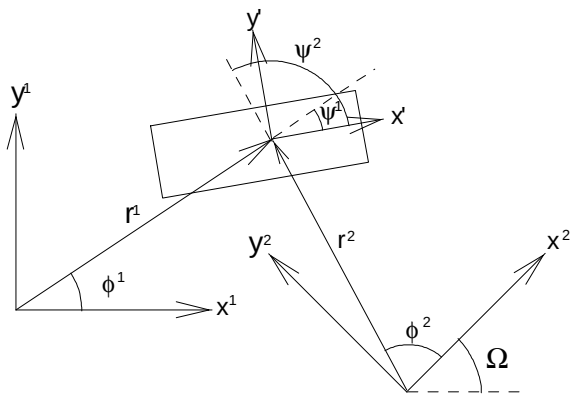

Figure 3.5: *Multisensor 2D sensor target geometry.*

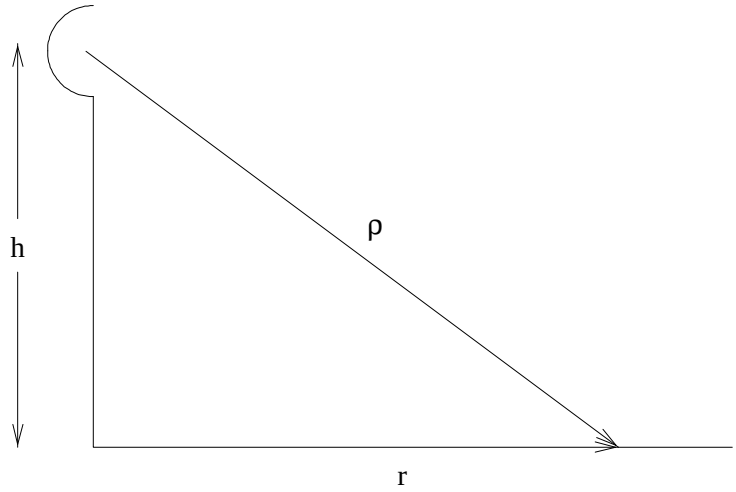

Figure 3.6: *Spherical frame and cilyndrical frame.*

for large r. The distance to the target is given by

$$\rho = \sqrt{h^2 + r^2} \tag{3.13}$$

This bias Δ can easily be accounted for if h is known and the targets move in a plane or surface with constant height, by assuming that the distance to the target is ρ when r is small. In coastal surveillance applications, the elevated position of the radars means that many structures on the top of the ship are visible and thus reflect the electromagnetic field transmitted from the radars, especially for short ranges.

3.3.2 Sampling in time and space

The radars in the considered applications were assumed to be surveillance radars in mono static configurations. Electromagnetic waveforms are transmitted and received using the same antenna element, which rotates and scans its surroundings in two dimensions. The scanning in azimuth is discrete in the sense that electromagnetic waveforms are transmitted and received at a finite number of azimuth angles. The received waveform at each azimuth angle is sampled in time at discrete intervals with a frequency f_r, which means that the corresponding sampling points in range are also discrete and spaced $d = c/f_r$, where c is the velocity of light in air. A schematic representation of how each radar scans the two dimensional space is shown in figure 3.7.

As shown in figure 3.7, the sampling points or the position of the pixels are regularly spaced in polar coordinates, but not in the Cartesian frame. The number of pixels per unit area is inversely proportional to the range r. The value of each sampling point or pixel is stored in an array, and each value is updated once per revolution of the radar. Typical revisiting time for each pixel is somewhere in the order of one to ten seconds.

If the position of a pixel k is given in polar coordinates by (r_k, ϕ_k), then its position in Cartesian coordinates is given by

$$\begin{bmatrix} p_k^x \\ p_k^y \end{bmatrix} = \begin{bmatrix} r_k \cos\phi_k \\ r_k \sin\phi_k \end{bmatrix} \tag{3.14}$$

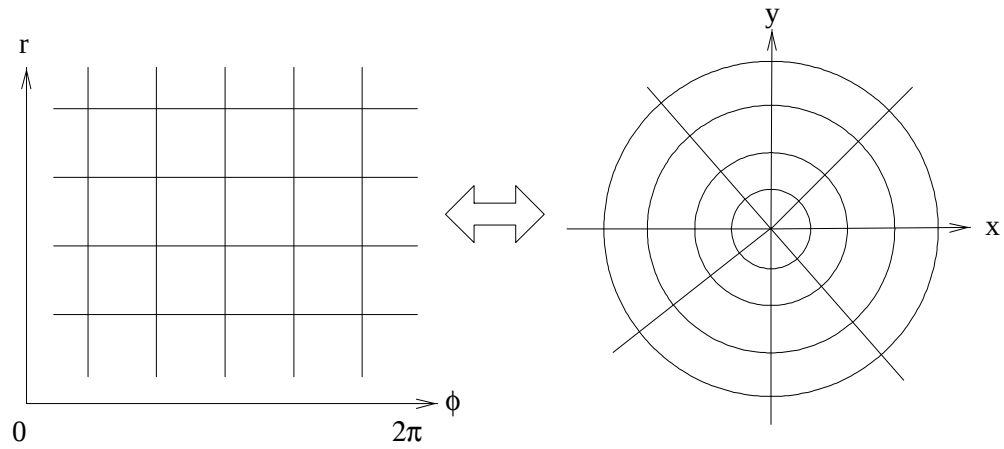

Figure 3.7: *Sampling geometry in two dimensions*

The bias caused by an antenna placed at a height h above the ground plane can easily be accounted for by replacing r_k by ρ_k, where ρ_k was defined in section 3.3.1.

Spatial filtering

The antenna element works as a spatial filter, by modulating the received electromagnetic field by its angular response function. When applying an antenna with width L and a rectangular aperture, the angular response function of the antenna is given by [7]

$$H(\theta) = \frac{\sin\left(\frac{\pi L}{\lambda}\sin\phi\right)}{\frac{\pi L}{\lambda}\sin\phi} \tag{3.15}$$

where λ is the wavelength of the transmitted wave, and θ is the off axis angle. A non rectangular aperture function will often be chosen in order to reduce the side lobes of the angular response function [7]. All antennas modeled in this thesis were assumed to be reciprocal, meaning that the angular response functions are the same when transmitting and receiving.

A filter with frequency response function equal to the complex conjugate of the frequency spectrum of the applied waveform is commonly applied for filtering in range. This filter is often called the matched filter [7], [9]. The frequency response of the matched filter is given by $\sin(\pi\tau f)/\pi\tau f$ when a rectangular waveform with pulses of duration τ is applied. The output from the matched filter is thus given by a triangular function with SNR at the peak output given by E/N_0, where E is the signal energy and N_0 is the noise power [7].

The resolution in range depends on the applied waveform as well as the sampling density. The maximum resolution when applying a rectangular waveform is given by the applied pulse length τ. If the resolution is defined as the smallest distance in which two point targets can be resolved, then it is given by $c\tau/2$.

Noise components in the sampled pixels

The noise in each pixel can be divided into two main components, thermal noise generated by the receiving system and clutter, which are reflections or radiation from other sources than the target

itself. The interfering objects may consist of a combination of other targets, clutter reflected from the sea surface, rain, the ground, other radars, and many other sources. The sources of the spurious reflections may be located close to the target or in one of the side lobes of the antenna. Waves reflected from the target may be reflected by the sea surface or other reflectors, and in effect interfere with waves traveling in a straight path to the radar. Cosmic radiation, waves transmitted from other radars, and other sources of electromagnetic interference will also disturb the measurements.

The intensity of the signal received from a single deterministic scatterer located at a distance R can be predicted by the standard radar equation [7], as

$$S_r = \frac{P_t G_r G_t A_r \sigma}{(4\pi R^2)^2} \tag{3.16}$$

where S_r is the received power, P_t is the transmitted power, G_r is the gain of the receiving antenna and A_r is the effective aperture area, G_t is the gain of the transmitting antenna and σ is the effective radar cross section of the target. The SNR can be estimated if the noise power in the system is known. When more than one scattering object contributes to the returned waveform, the received signal becomes a more complex function than indicated in equation (3.16). The waveform measured by the antenna can be modeled as a linear superposition of electromagnetic fields returned from each individual scattering object. The target image may have considerable fluctuations from scan to scan due to this interference and these fluctuations are frequently called speckle noise. The speckle noise may cause the apparent target center to wander outside the limits of the target.

Following the work in [2] where a quasi-optical simplest component method is presented, the measured signal can be written as the sum of the signals from each individual scattering object by the following equation.

$$\dot{E}(t, \mathbf{L}) = (\mathbf{p}_{rec}^0)^{*T} \left[\sum A_i(\mathbf{R}^0, \mathbf{L}) U(t - \Delta t_i) \exp(-j2\pi f \Delta t_i) 10^{-Q_{Abi}/20} \right] \mathbf{p}_{tr}^0 \tag{3.17}$$

$\dot{E}(t, \mathbf{L})$ is here a complex representation of the signal at time t, the magnitude of the signal is $\left|\dot{E}\right|$. The position of the receiving antenna relative to the transmitting antenna is defined by $\mathbf{L}$, which is zero for the mono static configuration. $U(t - \Delta t_i)$ is the output from the matched filter from scatterer number i, Δt_i is the delay in time from scatterer number i, Q_{Abi} is the absorption coefficient of the material of scatterer i expressed in dB, and $\mathbf{p}_{rec}^0$ and $\mathbf{p}_{tr}^0$ are the polarization of the receiving and transmitting antennas, respectively. $A_i(\mathbf{R}^0, \mathbf{L})$ is the polarization scattering matrix of scatterer number i.

Noise generated by the analog signal processing will interfere with the electromagnetic field measured by the antenna element. Given that the linear envelope detection is applied in the system, and that the measured signal is a sinusoidal signal with amplitude A, then the output from the envelope detector in a given pixel is given by the Ricean distribution

$$f_x(x|A, N) = \frac{x}{N^2} \exp\left(-\frac{x^2 + A^2}{2N^2} \right) I_0\left(\frac{Ax}{N^2} \right) \tag{3.18}$$

where N^2 is the noise power of the white noise generated by the system and I_0 is the modified Bessel function of zeroth order. This result was first derived by Rice [36] but a derivation can also be found for instance in [9]. Given that linear envelope detection is applied, the signal s_o in figure 3.8 thus has a Ricean distribution, where A is equal to the output calculated by equation 3.17, and N is the noise power of the system.

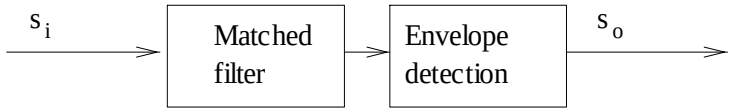

Figure 3.8: *Signal processing and envelope detection.*

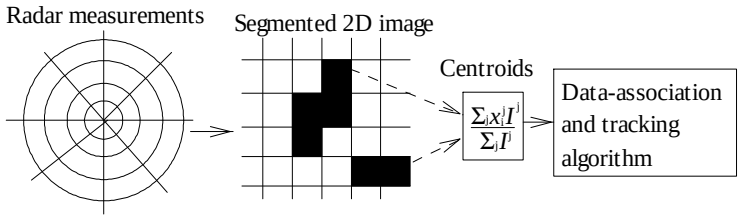

Figure 3.9: *Signal processing schematic in a 2D radar surveillance system.*

3.3.3 Signal processing

As discussed in *paper two*, the raw radar measurements in 2D surveillance systems are commonly processed as showed in figure 3.9 due to demand for efficient real time data processing capacity and high data rates encountered in surveillance systems. Thresholding and segmentation of the radar image is the next step after the analog signal processing. A kind of CFAR processing procedure is often applied in order to do detection, [8], [7]. The CFAR algorithm may be modified with a buffer on each side of the cell under test to be able to handle extended targets [7]. The pixels that have been tested and found to contain a measurement are then segmented into clusters assumed to contain the image generated by one target. The segmentation process, grouping of pixels that are in the image of the same target, can be done in several ways. A kind of nearest neighbor algorithm may be the simplest and most straightforward alternative. An efficient least-squares algorithm to cluster neighboring pixels in surveillance systems is proposed in [18], [37].

In some cases, the images from two separate targets may be overlapping for a period of time. This could be handled by the data association algorithm, as for instance described in [3]. A measurement vector $z = \begin{bmatrix} z_x & z_y \end{bmatrix}^T$ is generated for each segment, by calculating the image centroid . The centroid position measurement in each coordinate is given by

$$z_x = \frac{\sum_j x^j I^j}{\sum_j I^j} \tag{3.19}$$

$$z_y = \frac{\sum_j y^j I^j}{\sum_j I^j} \tag{3.20}$$

where *j* runs over all the pixels in pixel cluster or segment. I^j is here the measured intensity or amplitude of pixel number *j* and $\begin{bmatrix} x^j & y^j \end{bmatrix}^T$ is the position of each pixel in the plane.

Equation (3.19) and (3.20) show that z_x and z_y never will be independent. The same intensi-

ties or amplitudes appear in each expression,

$$z_x = f\left(I^1, I^2, ..., I^N\right)$$
$$z_y = g\left(I^1, I^2, ..., I^N\right)$$

The intensities I^j are in general random because of the random components in each pixel, as discussed in section 3.3.2. Thus, the joint probability density function $f_{xy}\left(z_x, z_y\right)$ can never be written as $f_x\left(z_x\right) f_y\left(z_y\right)$. In some cases, the covariance may be approximately zero.

$$C_{z_x z_y} = E\left(\left(z_x - \bar{z}_x\right)\left(z_y - \bar{z}_y\right)\right) \approx 0$$

The two centroids are thus uncorrelated, but not independent.

3.3.4 Target model

As presented in *paper three*, the target was modeled to consist of a large number of conducting spheres randomly distributed over a given area, but with fixed positions relative to each other. The point targets were distributed on a rectangular or ellipsoidal area, where the size and shape of the area were chosen to resemble the shape of ships. The main aim of the simulations was to simulate the spatial extent of the target, rather than the 3D geometric form of a real target. By applying the conducting sphere model, the terms relating to polarization in equation (3.17) are eliminated, as the electromagnetic field is reflected from a conducting sphere without changes in the polarization. All multiple reflections were ignored in the simulations, and the scatterers were mostly modeled to have equal radar cross section. An illustration of a target used in the simulations can be seen in appendix A.

3.3.5 Radar image generation

The approach presented in [2] is based on constructing target models using simple objects with known reflective properties. In this manner, the signal reflected from the target may be reconstructed using equation (3.17). When the target is constructed by conducting spheres and the polarization of the receiving antenna is assumed to be equal to that of the transmitting antenna, the field equation (3.17) simplifies to the following equation.

$$\dot{E}(t) = \sum\nolimits_i U(t - \Delta t_i) \exp(-j2\pi f \Delta t_i) \tag{3.21}$$

The Q_{Abi} factor could be assumed to be approximately zero, and was anyway canceled out from the equations as only SNR was considered in this work.

The angular response of an element located at an angle $(\phi - \phi')$, where ϕ' is the direction of the main axis of the antenna, is given by equation 3.15 squared, as

$$H^2\left(\phi - \phi'\right) = \left(\frac{\sin\left(\frac{\pi L}{\lambda}\sin\left(\phi - \phi'\right)\right)}{\frac{\pi L}{\lambda}\left(\phi - \phi'\right)}\right)^2$$

The equation is squared because of the reciprocity of the antenna; it is modeled to have the same angular response for transmission and reception of the signal.

Assuming that the applied waveform is quadratic and that the matched filter can be realized in an optimal manner, the output is given on the following form where T is the length of the

pulse.

$$U'(t) = \begin{cases} 0 & t < 0 \\ At & 0 \leq t < T \\ 2AT - At & T \leq t < 2T \\ 0 & 2T \leq t \end{cases}$$

The response as a function of time can be translated to response as function of range, $U(r)$, by using that $r = \frac{ct}{2}$ and $L = \frac{cT}{2}$. Thus the output from the signal processing at a range r for when the antenna is directed at ϕ is given by the sum of the contribution of the individual scattering objects as

$$\dot{E}(r, \phi) = \sum_j H^2 \left(\phi^j - \phi\right) U\left(r - r^j\right) \exp(-jk\left(r - r^j\right)) \tag{3.22}$$

where $\left(r^j, \phi^j\right)$ is the position of scattering object number j and k is the wave number of light in air.

As discussed in section 3.3.2, the resolution in range and angle is finite. The effect of the finite sampling grid, that the location of the target relative to the sampling points of the system may generate significant variations in the target images, was discussed in *paper three*. This effect was found to be larger for a high SNR. In order to compensate for this effect, the sampling grid was moved to M x N different positions for each target image, and the image was processed for each choice of sampling grid. The value of each separate pixel could then be calculated by equation (3.22), and noise could be added by assuming that the value of the pixel was given by the Ricean distribution in equation (3.18), where $A = K \cdot \left|\dot{E}(r, \phi)\right|$. The normalization factor K is included in order to be able to define the SNR in the simulations. Only the SNR was investigated, which meant that only the relationship A^2/β^2 in equation (3.18) was of interest in each pixel. Thus, the scale factor could be adjusted in the simulations in order to obtain the estimated SNR. The sensor geometry shown in figure 3.4 was used as basis in the simulations. The targets were located at the x-axis, $\phi = 0$, while the range, r, aspect angle or heading $\psi = \theta$ and SNR were varied in order to investigate the statistical measurement error.

3.3.6 Measurement error models

The conditional forms of the measurement equations presented in *paper three* were used in the Monte Carlo simulations. The measurement noises were assumed to be Gaussian, additive, and zero mean in all of the models, as $z = Hx_k + w_k$.

Model C

As argued in *paper three*, the first model was named model C, as the measurement covariance is assumed to depend on the position in Cartesian space. This is the standard equation which may be obtained by applying a Taylor expansion on equations (3.8) and (3.7), [38].

$$\operatorname{cov}(w_k|\phi_k) = E\left(w_k w_k^T|\phi_k\right) = \Phi_k R_k^C \Phi_k^T \tag{3.23}$$

$$= \begin{bmatrix} \cos\phi_k & -\sin\phi_k \\ \sin\phi_k & \cos\phi_k \end{bmatrix} \begin{bmatrix} \sigma_r^2 & 0 \\ 0 & \sigma_{\phi*}^2 \end{bmatrix} \begin{bmatrix} \cos\phi_k & \sin\phi_k \\ -\sin\phi_k & \cos\phi_k \end{bmatrix} \tag{3.24}$$

The measurement noise thus consists of an angular and a range component, where the variance of the angular component is $\sigma_{\phi*}^2$ with units m^2.

Model O

The second model was named model O in *paper four*, as it assumes that the measurement noise can be expressed in the reference frame of the object or target. The model was introduced in *paper two* and aligns the eigenvectors of the measurement covariance matrix with the main axes of the target. The measurement model can be expressed in a quasi linear form by the following equations.

$$\begin{aligned}\operatorname{cov}\left(w_k|\theta_k\right) &= E\left(w_k w_k^T|\theta_k\right) = \Theta_k R_k^O \Theta_k^T \\ &= \begin{bmatrix} \cos\theta_k & -\sin\theta_k \\ \sin\theta_k & \cos\theta_k \end{bmatrix} \begin{bmatrix} \sigma_a^2 & 0 \\ 0 & \sigma_t^2 \end{bmatrix} \begin{bmatrix} \cos\theta_k & \sin\theta_k \\ -\sin\theta_k & \cos\theta_k \end{bmatrix}\end{aligned} \tag{3.25}$$

Model 3P

The second new proposed model is a compromise between the two previous models, and was introduced in *paper three*. The measurement noise is assumed to have an angular component, but also a component that is correlated with the aspect angle of the target. The measurement noise is assumed to be composed of the sum of two independent Gaussian random variables, which again is a Gaussian random variable. The measurement model can be written in a quasi linear form as

$$\begin{aligned}\operatorname{cov}\left(w_k|\theta_k,\phi_k\right) &= E\left(w_k w_k^T|\theta_k,\phi_k\right) = \Theta_k R^O \Theta_k^T + \Phi_k R^{C*} \Phi_k^T \\ &= \begin{bmatrix} \cos\theta_k & -\sin\theta_k \\ \sin\theta_k & \cos\theta_k \end{bmatrix} \begin{bmatrix} \sigma_a^2 & 0 \\ 0 & \sigma_t^2 \end{bmatrix} \begin{bmatrix} \cos\theta_k & \sin\theta_k \\ -\sin\theta_k & \cos\theta_k \end{bmatrix} \\ &+ \begin{bmatrix} \cos\phi_k & -\sin\phi_k \\ \sin\phi_k & \cos\phi_k \end{bmatrix} \begin{bmatrix} 0 & 0 \\ 0 & \sigma_{\phi*}^2 \end{bmatrix} \begin{bmatrix} \cos\phi_k & \sin\phi_k \\ -\sin\phi_k & \cos\phi_k \end{bmatrix}\end{aligned} \tag{3.26}$$

3.3.7 Maximum likelihood estimation

The basic principle of ML estimation is to maximize a likelihood function $f\left(Z;x\right)$, which is a function of a set of measurements, Z, and a vector of parameters x. The likelihood function is then maximized with respect to the parameter vector, and the estimate is given by

$$\hat{x} = \arg\max_x f\left(Z;x\right)$$

The maximum likelihood estimate can in some cases be found by a closed form solution, while in other cases a search algorithm has to be applied to obtain a numerical solution. When the N independent measurements have a Gaussian distribution defined by

$$f_z\left(z\right) = \mathcal{N}\left(z;\bar{z},C\right) = \frac{1}{|2\pi C|}\exp\left(-\frac{1}{2}\left(z-\bar{z}\right)^T C_z^{-1}\left(z-\bar{z}\right)\right)$$

where $z_k = \left[z_k^x, z_k^y\right]^T$, then the ML estimates of the mean and covariance $\bar{z}$ and C_z are given by the sample mean and variance,

$$\widehat{\bar{z}} = \begin{bmatrix} \widehat{\bar{z}}^x \\ \widehat{\bar{z}}^y \end{bmatrix} = \begin{bmatrix} \frac{1}{N}\sum_{k=1}^N z_k^x \\ \frac{1}{N}\sum_{k=1}^N z_k^y \end{bmatrix} \tag{3.27}$$

$$\hat{C}_z = \frac{1}{N}\begin{bmatrix} \sum_{k=1}^N \left(z_k^x - \widehat{\bar{z}}^x\right)^2 & \sum_{k=1}^N \left(z_k^x - \widehat{\bar{z}}^x\right)\left(z_k^y - \widehat{\bar{z}}^y\right) \\ \sum_{k=1}^N \left(z_k^x - \widehat{\bar{z}}^x\right)\left(z_k^y - \widehat{\bar{z}}^y\right) & \sum_{k=1}^N \left(z_k^y - \widehat{\bar{z}}^y\right)^2 \end{bmatrix} \tag{3.28}$$

Replacing the factor $\frac{1}{N}$ by $\frac{1}{N-1}$ in equation (3.28) gives an unbiased estimator [12]. This estimator was applied when estimating the parameters of model C and O described in section 3.3.6.

When estimating the parameters of the model named 3P in section 3.3.6, a numerical search algorithm was applied. The log likelihood function is proportional to the following function

$$\log f_Z\left(Z|x\right) \sim \sum_{k=1}^{N} -\frac{1}{2}\left(z-\hat{z}\right)^T \hat{C}^{-1}\left(z-\hat{z}\right)$$

The log likelihood function was maximized with respect to the parameters σ_a^2, σ_t^2 and $\sigma_{\phi*}^2$ in order to obtain an estimate of the three parameters.

3.3.8 Distance measures

In order to obtain a measure of the distance between the generated measurements and the models, the symmetrized Kullback Leibler Divergence (KLD) was used. The KLD was used as a relative measure of the distance between the data set and the error models. The general symmetrized KLD is given by [39]

$$\begin{aligned}\mathcal{I}^{KLD}\left(f_p\left(x\right), f_q\left(x\right)\right) &= \mathcal{I}^{KL}\left(f_p\left(x\right), f_q\left(x\right)\right) + \mathcal{I}^{KL}\left(f_q\left(x\right), f_p\left(x\right)\right) \\ &= \int f_p\left(x\right)\log\frac{f_p\left(x\right)}{f_q\left(x\right)}dx + \int q\left(x\right)\log\frac{f_q\left(x\right)}{f_p\left(x\right)}dx\end{aligned}$$

The general KLD was not applied in this work because of the difficulties related to evaluation. However, the symmetrized KLD between two Gaussian distributions is given by [39]

$$\begin{aligned}&\mathrm{KLD}\left(\mathcal{N}_1\left(x;\mu_1,P_1\right),\mathcal{N}_2\left(x;\mu_2,P_2\right)\right) \\ &= \frac{1}{2}trace\left(P_1^{-1}P_2 + P_2^{-1}P_1\right) + \frac{1}{2}\left(\mu_2-\mu_1\right)^T\left(P_1^{-1}+P_2^{-1}\right)\left(\mu_2-\mu_1\right) - \dim\left(x\right)\end{aligned} \quad (3.29)$$

This measure was used to evaluate the distance between a parameterized likelihood function and the likelihood function constituted by a set of simulated measurements, following [40] where the symmetrized KLD distance is used to measure the distance between two posterior distributions. The measure KLD in equation (3.29) was used to rank the distances between the estimated error models and the generated data set.

The performance of a tracking filter applying an estimated measurement likelihood function was also applied as a distance measure, following the discussion in *paper four*. From the view of the end user, this may be the only relevant distance or performance measure. Using the framework described in the previous sections, a simulated target was moved around in Cartesian space. A radar image was simulated at each position, and fed to tracking algorithms applying error models previously derived for the same target by the methods described in this section. The

distance measures were then given RMS position, velocity and heading errors, defined by

$$RMSEp = \sqrt{\frac{1}{N}\sum_{k=1}^{N}\left(p_k^x - \hat{p}_k^x\right)^2 + \left(p_k^y - \hat{p}_k^y\right)^2} \tag{3.30}$$

$$RMSEv = \sqrt{\frac{1}{N}\sum_{k=1}^{N}\left(v_k^x - \hat{v}_k^x\right)^2 + \left(v_k^y - \hat{v}_k^y\right)^2} \tag{3.31}$$

$$RMSE_\theta = \sqrt{\frac{1}{N}\sum_{k=1}^{N}\left(\theta_k - \hat{\theta}_k\right)^2} = \sqrt{\frac{1}{N}\sum_{k=1}^{N}\left(\theta_k - \arctan\frac{\hat{v}_k^y}{\hat{v}_k^x}\right)^2} \tag{3.32}$$

3.3.9 Simulation results

Some additional simulation results extending the results that were presented in *paper two*, *paper three,* and *paper four* are presented in appendix A. The first part of the appendix includes some illustrations where the effect of small changes in aspect angle on the measurement errors was examined. It was illustrated how a small change in aspect angle could cause large fluctuations in the target image due to speckle noise. Five examples are then included, which showed that the measurement noise is a complex function of target size and shape, sampling rate, spatial resolution, and SNR.

The first included example is similar to the work in *paper three*, where the SNR of the target was kept constant while the range was varied. The KLD for each of the error models were calculated and plotted as function of range. The next example shows results for a target at fixed range, where the noise models were estimated as function of SNR, similar to the results shown in Table 1 of *paper three*. The KLD was calculated for all three error models, and the plots are included in the appendix.

Example three in the appendix shows results where the relationship between target size and the parameters of the error models were examined, while the position and SNR of the target were kept fixed. It was shown that the angular component of the 3P model is zero until the target reached a certain size, and that the estimated parameters depended on target size.

In example four, the influence on the measurement noise from sampling density in range and bearing as well as angular and range resolution were examined. This example is inherently linked to example three and the example shown in *paper four*. The tables given in the appendix show how the sampling rates in range and azimuth seem to have a larger influence on the measurement errors than the lobe width and pulse length.

In example five, the relationship between the shape of the target and the measurement noise models was examined. The area of the simulated target was kept fixed while the ratio between the dimensions was altered. The simulations showed that the dependency on aspect angle was zero when the ratio was one, which also was expected.

4

Discussion

THE parts of this thesis reported in papers one to four, as well as in the additional results presented in chapter 2 and 3, are all relevant for tracking in radar surveillance systems. The first part presented in paper one and chapter 2, focused on the most low level part of the tracking system, the detection part where measurements are extracted from raw radar data. This work showed how clutter density or instantaneous false alarm rate can be estimated in each scan at a given location for a CFAR system. The clutter density is an important input to the part of the system that performs track initiation, maintenance and termination. The main topics of paper two to four and chapter 3 were modeling the statistical error of the measurements obtained from the detection algorithm and applying these models in tracking algorithms in an optimal manner. A discussion on the main findings and conclusions in both parts of the thesis is given in the following sections.

4.1 Clutter density estimation in CFAR systems

The work presented in paper one and further analyzed in chapter 2, introduced several tools that may be used to analyze a CFAR detection system. The tools can be integrated into a tracking system in order to increase the knowledge about the number of false alarms being fed to the tracker at a given scan. The variance of the clutter density, σ_p^2, was derived for several CFAR configurations as an intermediate result, and it was shown how the variance is useful when analyzing a CFAR system. The system parameters should be chosen in order to minimize this variance. It was also discussed in section 2.1.2 that the derived variance can be used as a measure of CFAR loss. This measure would then be independent of the type of target considered, in contrast to other conventional definitions of CFAR loss. The derivation of the pdf and the variance of the clutter density or the instantaneous false alarm rate in section 2.1.1 have not been reported previously in any known literature. Previous studies have focused mainly on the mean false alarm rate $P_{FA} = E(p)$.

Linear Bayesian estimators were derived in paper one based on P_{FA} and σ_p^2 in order to estimate the mean clutter density, given the numbers of declared measurements as input. However, analytical expressions of P_{FA} and σ_p^2 are only possible to obtain in a few cases for some given

CFAR configurations and noise distributions. Numerical values for P_{FA} and σ_p^2 may be derived if the noise distribution is known, but exact knowledge or good estimates of the background distribution may not always be available.

Empirical Bayesian estimators were introduced in paper one in order to avoid the dependence on knowledge of the background noise. Empirical Bayesian estimation is not well known, and it is discussed how the method may be useful in cases where the prior distribution of the estimatee is unknown. The results presented in chapter 2 provided further analysis of the convergence properties of LEB estimators than presented in paper one. The plots in section 2.2.6 illustrated that the LEB estimators converged to the corresponding BLUE estimates, and that the rate of convergence depended on the system configuration and parameters. For CA-CFAR systems, a relatively large number of scans were needed when the mean false alarm rate was $P_{FA} = 10^{-4}$ or smaller.

From a system point of view it may be unrealistic to acquire over 1000 scans at the same location with the same distribution. Collecting a set of past data with the same distribution is one of the foundations of the nonparametric EB approach. The noise distribution may change as a result of change in weather conditions or other disturbances. Changes in the mean noise power for Rayleigh noise would not have any effect, but changes in scale factor γ for Weibull noise would influence the mean false alarm rate, the clutter density variance and hence also the estimator. In a radar surveillance system, a long history may be available, and calculating the sample mean and variance recursively is relatively inexpensive. A sliding average system may also be applied, where M of the previous samples is used to calculate the mean and variance, although such a system may be sensitive to abrupt change in conditions. On the other hand, the assumed P_{FA} would probably also be erroneous in this case.

Data obtained at the same scan could also be used to estimate the sample mean and averages, using spatial data instead of temporal data, as history. For instance, in many ocean surveillance radar systems one scan can hold several million of pixels. Assuming a slowly varying sea condition in space, the LEB estimator could be used to improve the knowledge of clutter density at each location.

The Bayesian estimators introduced in paper one all relied on the assumption that the number of false alarms was given by a binomial distribution. It was argued in section 2.2.1 that this assumption limits the number of systems where the method can be applied. Other properties of the system may also cause the number of false alarms to deviate from the binomial distribution, like for instance spatial or temporal correlation between the cells. Analysis of spatial correlation is often missing in analysis of CFAR systems, with the exception of [11] where CFAR in a system with K-distributed noise and spatial correlation was analyzed.

Provided that the binomial assumption holds, the results plotted in paper one clearly indicate that the BLUE estimator provides a better estimate of the clutter density in each scan than the conventional assumption that the clutter density is constant and equal to P_{FA}. The gain is shown to be largest for high mean false alarm rates and small sets of reference cells, when the variance of the clutter density is relatively high. The methods are also possible to extend to other distributions, like for instance the Poisson distribution which is commonly applied as a model for false alarms.

4.2 Monte Carlo simulations

The main aims of the performed Monte Carlo simulations were to investigate the correlation between aspect angle and position measurement noise for extended targets, and develop measurement models that could be applied in tracking filters in scenarios where this effect may

occur. The Monte Carlo simulations applied the framework described by [2], but the position measurement errors were investigated rather than the effective radar cross section, which is a novel approach. The results from the simulations given in paper two, three, and four as well as in appendix A of this thesis, show how a number of different parameters may influence the measurement noise, such as target size, applied waveform, aspect angle, sampling resolution in range and bearing as well as SNR. The plots included in paper four are the most relevant for a tracking scenario, as the SNR is modeled to be a function of range. The parameters of the C, O and 3P error models were estimated as target is moved from close range where it is extended with respect to the angular resolution of the system and the SNR is high, to long range where it has a low SNR and approaches a point target in bearing. The plots show how the parameters of each model are a function of range, and that 3P and O models are equivalent at short range.

The estimated parameters of the proposed measurement noise models were demonstrated to be sensitive to the parameters of the simulation setup, which means that to use a simulation setup like the one described in this thesis to derive the parameters in a real system may be unrealistic. Such predictions would require more detailed models of the signal-target geometry, the applied antennas and waveforms as well as the analog and digital signal processing. A real system will include nonlinearities and correlations that may be impossible to fully characterize. A discussion of the influence of some unmodeled effects can be found in the following subsections. On the other hand, the simulation results strongly indicate that there is a dependency between aspect angle, target size, angular resolution and the variance of the position measurement error. The simulations in paper four showed that the 3P which incorporates dependency on both bearing and heading angle had better RMSE performance than the O and the C models. The only way to fully verify the derived models directly would be from empirical data, obtaining measurements from a real target at varying ranges and aspect angles, similar to previous work on radar cross section for varying targets. This kind of experiment would first of all be costly and time consuming and secondly the results may not be easy to generalize to other targets and sensors. An alternative approach is therefore proposed, where the RMSE performance of a tracking filter applying the error models is used as a measure of the goodness of the models, following the approach applied in simulations in paper two and four. For instance, in maritime surveillance applications data from both radar measurements and measurements from GPS transponders are available for a large number of targets and trajectories. The performance of tracking filters with different measurement error models using the radar measurements as inputs could be compared to that of filters using GPS measurements as input. Care should then be taken in modeling the temporal correlation and error in the GPS measurements, and avoid using them as ground truth. A large number of trajectories covering all aspect angles and ranges are also needed in order to make the parameters of the differences between the noise models observable.

A large number of measurements from a single target or a class of targets could also potentially be used to tune the parameters of the measurement error models with respect to minimizing the RMSE of the estimation filters. This setup could also be used to estimate and verify the parameters of the state dependent bias models introduced in paper four, using for instance the real time approach described in [41] or a suitable batch approach.

A second approach could be to determine the parameters of the measurement equations based on the parameter estimates shown in paper four, combined with the plot shown in figure A.18 in this thesis. The angular component of the 3P model could then be set to zero until the angular sampling distance is larger than the largest dimension of the target. The values of σ_a, σ_t, and $\sigma_{\phi*}$ could then be selected based on a combination of analytical considerations and experience, which often is the case when tuning a real system. An alternative solution could be to apply only the C and the O models, switching between the models at a given range. The C and the O model

require somewhat lower computational resources than the 3P model.

The measurement error models were developed for surveillance system applications, based on the modeled target sensor geometries, waveforms and sampling structures. However, the derived models may also be applicable for other applications like for instance automotive radar systems where targets may be large compared to the resolution of the sensor, and where state dependent biases and correlations may be present. The simulation framework may in any case be adapted to this kind of application.

As mentioned in paper two, the derivations of the error statistics of the centroid of an optical image proposed in [34] can be extended by deriving the measurement cross correlation $C_{xz} = E(z_x z_y)$. The O model introduced in paper two could thus be applied directly in this case, if the velocity vector can be assumed to be aligned with one of the main axes of the target.

4.2.1 System model

As discussed in paper two as well as in chapter 3, simplified system models were applied in the simulations in order to generate radar images. The components that contributed to fluctuations in the generated measurements were simulated thermal noise, speckle noise in the radar images and the placement of the target relative to the sampling grid in range and bearing. A number of other sources of noise that may be present in a real system were not modeled, as for instance multipath effects, where the reflected signal from an object gets reflected by another surface and cause interference effects [7]. Multiple reflections within the target itself were also ignored in the simulations. Interference from other targets, signals from other radar transmitters, either in the main lobe or in one of the side lobes, may also effectively influence the measurements. The expected effect of all these sources of noise would be larger fluctuations in the target images, especially for high SNR cases. The magnitude of the variances of the noise models may thus increase.

Clutter, spurious returns from objects or surfaces close to the target, may also influence the target image. As discussed in paper four, clutter may become a part of the target image and hence directly cause biases or have a scaling effect on the position measurement noise. The clutter signal may also interfere with the target signal and hence generate speckle noise. The expected effect of the clutter is an increase in the magnitudes of the variances of the error models, as well as potentially causing state dependent biases if the generation of clutter depends on the state of the target.

In the performed simulations, it was assumed that the system applied a perfect matched filter on a rectangular waveform, which is impossible to implement in a real system. However, a suboptimal matched filter is also easily incorporated into the proposed framework; an ideal matched filter is assumed for generality purposes. The angular response function can also easily be adapted to any weighting function; the uniform weight function was implemented for simplicity giving a sinc angular response function.

4.2.2 Target models

The target model applied in the simulations was a simplified model, following the approach suggested in [32]. The method using a high number of conducting spheres simplified the calculations to the level that they could be used to generate a high number of measurement in the Monte Carlo simulations with reasonable computational resources. The simulations could easily be extended by including a more complex target model, using the simplest component quasi optical approach described in [2]. A ship or any other target could then be constructed by building a model of

simple geometrical planes and shapes. In this manner, the occlusion effects discussed in paper four and the correlation between measurements for small changes in aspect angles could be examined. However, a more complex target may also give a less general result, as the examination and modeling is done for a specific target or class of targets. The main aim of the investigations was to examine correlation between aspect angle and position measurement error for a general extended target, and this was achieved using the simple model. As argued in paper three, the assumption that a target consists of a large number of scattering objects uniformly distributed over a given area may be realistic for some scenarios, for instance in surveillance applications where the radar is elevated above the surface and the targets are large rectangular or ellipsoidal steel structures.

Corner reflectors and other objects that have an effective radar cross section that may vary strongly as function of aspect angle or elevation are expected to cause more fluctuations or speckle noise in the generated images compared to a model with conducting spheres. This may also increase the variance of the parameters of the noise models. Corner reflectors will most likely also cause large peaks in the signal image for some aspect ratios, which may influence the centroid position. On the other hand, this kind of peaks will often be clipped by the system amplifiers, which again eases this effect. Corner reflectors and similar objects may also contribute strongly to the occlusion and correlation effects which were discussed in section 3.2.2.

4.3 Trajectory generation and benchmarking

As discussed in paper two, the selection of trajectories in a simulation of a tracking system may have a significant effect on the performance of the algorithm under test. The presented solution was to define the system using a non linear jump Markov system, which generated random sequences of maneuvers. The velocity was limited by configuring the system such that the probability for further acceleration was zero when the velocity was higher than a given limit. In a similar manner, the velocity could be given a lower limit. The set of maneuvers consisted of three subsets, one set with constant velocity and turn rate where each member had different turn rates, one set of constant acceleration and heading where each member had different accelerations, and one state where the target moved with constant velocity and heading. The system was defined by the states included in the maneuver state space and the transition matrix of the non stationary Markov chain which determined the transition probabilities at each time.

The trajectory generator was used for simulation purposes, but the main idea introduced in paper two was to extract the Markov transition probabilities from previous data, and use the extracted system to generate trajectories in benchmark simulations. This approach eliminates the need to know the ground truth, as the trajectories can be extracted from noisy data. In paper two it was proposed to generate all trajectories using relatively few maneuvers, adding process noise in each dimension. However, when extracting the Markov chain transition probabilities, there is likely to be cases where the real maneuver is the middle two neighbor states, causing the extracted maneuver to toggle between the two states. This would influence the mean sojourn time of the two states, the average number of scans the system spends in a given state. In paper four, the setup was slightly modified, in the sense that a larger number of states was used to generate the trajectories, and in the simulations the probability that the system would jump to a neighbor state was higher than for other states. In this manner, less rigid maneuvers were generated, and the result was more similar to the expected result when extracted from historical data. A single maneuver could then be defined to last the time the system stayed in the same state or jumped to a neighbor state.

The main disadvantage of the presented approach is that it is dependent on that the real

trajectories can be divided into these classes of well defined maneuvers. This may be the case for cooperative, civilian ships, but may not be the case for other scenarios and target dynamics. Recently, the curvilinear dynamic model has been proposed for generating realistic trajectories with colored process noise and sudden accelerations [42].

Instead of relying on interpreting the performance of a tracking filter in a few selected maneuvers, the presented approach introduced the possibility to perform a systematic investigation of filter performances. As demonstrated in paper two and four, a long representative trajectory can be used if the measurement noise is constant in Cartesian space. This trajectory will thus contain a very large number of combinations of different maneuvers, and the RMSE performances of the estimation filters were demonstrated to converge towards constant values. In this manner, the average RMSE as a function velocity, turn rate, time after initialization of a new maneuver and a number of other parameters can be estimated. The performance of different estimation filters can also be compared using this tool, as demonstrated in paper two where the generator was used as a benchmark tool. In the case of a non uniform measurement noise, the approach can be used to generate a large number of trajectories within a given area, which was used to plot RMSE as function of range in both paper two and paper four. The use of a random trajectory generator is of course not limited to measuring RMSE performance, it could also be used in sensor fusion systems, to measure track loss, track initialization, and other important parameters in a target tracking system.

4.4 Estimation filter implementation

In paper two, the O and C models presented in paper three were applied in IMM estimation filters where the conditional noise covariance matrices were used as inputs to the estimation filters. The noise covariance then needed to be approximated based on an estimated or measured parameter, and the discussion in paper two indicated that the approach was suboptimal in cases where this parameter had a large variance. This problem was solved by the introduction of BLUE estimation filters in paper four. The work in paper four introduced several new features. Firstly, BLUE filters were introduced as optimal for state dependent measurement noise, where the general assumptions of the Kalman filter do not hold. Secondly, several state dependent measurement biases were proposed, and recursive BLUE filters were derived to provide optimal estimates of the target state in the presence of these biases. Thirdly, commonly applied measurement equations were reformulated using state dependent random matrices in order to express the measurement noise vector as unconditioned. Fourthly, it was shown how the commonly applied third order unscented transform fails to approximate the innovation covariance matrix in the case of transformations that involves rotation, and it was shown how the higher order, or fifth order, unscented transform could be used to resolve this problem. The HOUT was used to approximate the terms of the recursive BLUE filters that did not have closed form expressions. Fifthly, it was shown that the 3P model introduced in paper three had better RMSE performance than both the O and the C models at all ranges, using simulated radar measurements as input. Sixthly, it was demonstrated how the random trajectory generator introduced in paper two could be used to examine RMSE performance as a function of velocity.

It was shown how the BLUE filters had better RMSE performance than suboptimal filters based on the conditional covariance matrix. The gain of the BLUE approach compared to suboptimal Kalman filters was shown to be largest when the variance of the estimated variable used to approximate the conditional covariance was large. The simulations also revealed that the suboptimal filters performed equally well as the BLUE filters when the uncertainty in the estimated variable was small. This was specifically shown to be true for the case where the velocity was

large and the error covariance was conditioned on the predicted heading vector, which was defined as the direction of the velocity vector.

The work in paper three and in chapter 3 of this thesis derived the correlation between aspect angle and measurement error, while work presented in paper four assumed that the velocity vector was perfectly aligned with the heading angle. It is assumed that the relationship between heading angle and the velocity vector can be derived for cases where they fail to be parallel.

The BLUE filter is optimal in the sense that it can be shown to be the estimator which is a linear function of the measurement, $\hat{x} = Az + b$, that minimizes the cost function $J = E\left(\left(x - \hat{x}\right)^T \left(x - \hat{x}\right)\right)$. For the case where the measurement noise is Gaussian, the BLUE estimator can be shown to be the optimal estimator also in a general mean square error sense, not just the optimal linear estimator [12]. However, for the cases where the HOUT was used to approximate the terms of the BLUE estimator as well as for the cases where random biases were present, it can not be guaranteed that the BLUE estimator is optimal. Also, the system model used for state prediction will never be exact, as it is impossible to model the future motion of an unknown target, which again means that the system may be inconsistent at times. A comparison with optimal Bayesian estimator implemented using Monte Carlo methods could be done for verification, see for instance [27]. However, the Monte Carlo methods are not suited for implementation in a high target density surveillance system because of their high computational load and the real time demands of the surveillance system.

The framework described in paper four may be applied directly in a maritime surveillance system, without significant increase in computational cost compared to suboptimal linear estimation algorithms. Whether a BLUE filter is needed or a suboptimal filter is sufficient to handle the correlation between bearing angle, heading angle and measurement error may be determined dependent on the velocities of the targets, the measurement errors as well as the distance from the sensor.

The bias models proposed in paper four may also be highly relevant for this application. Firstly, for low grazing angles, a large part of a ship may be occluded when heading towards or from the radar, while a large part of the structure may be visible while moving in a transverse direction. Secondly, a ship may induce a significant wake which may generate clutter that becomes rendered as a part of the target image by the segmentation algorithm, as illustrated in chapter 3.

The measurement errors will be dependent on the target state in many practical applications, as for instance in SAR applications where the measurement error may be dependent on target velocity. These challenges have not received proper attention in previous literature, with some exceptions [43]. The proposed BLUE filter framework introduce a systematic manner to do optimal estimation in these cases.

Bibliography

[1] *International Convention for the Safety of Life at Sea (SOLAS) - chapter V.* International Maritime Organization (IMO), 2000.

[2] Y. D. Shirman, ed., *Computer Simulation of Aerial Target Radar Scattering, Recognition, Detection, and Tracking.* Norwood, MA: Artech House, 2002.

[3] Y. Bar-Shalom and X. R. Li, *Multitarget-multisensor tracking: Principles and techniques.* Storrs, Conn.: YBS, 1995.

[4] S. S. Blackman and R. Popoli, *Design and analysis of modern tracking systems.* Boston, MA: Artech House, 1999.

[5] D. Musicki, R. Evans, and S. Stankovic, "Integrated probabilistic data association," *IEEE Transactions on Automatic Control*, vol. 39, no. 6, pp. 1237–1241, 1994.

[6] X. R. Li and N. Li, "Integrated real-time estimation of clutter density for tracking," *IEEE Transactions on Signal Processing*, vol. 48, no. 10, pp. 2797–2805, 2000.

[7] D. K. Barton, *Modern radar system analysis.* Norwood, MA: Arthech House, 1988.

[8] H. Rohling, "Radar cfar thresholding in clutter and multiple target situations.," *IEEE Transactions on Aerospace and Electronic Systems*, vol. 19, no. 4, pp. 608–621, 1983.

[9] N. Levanon, *Radar Principles.* New York: John Wiley & Sons, 1988.

[10] N. Levanon and M. Shor, "Order statistics cfar for weibull background," *IEE Proceedings, Part F: Communications, Radar and Signal Processing*, vol. 137, no. 3, pp. 157–162, 1990.

[11] S. Watts, "The performance of cell-averaging cfar systems in sea clutter," in *The Record of the IEEE 2000 International Radar Conference*, pp. 398–403, 2000.

[12] Y. Bar-Shalom, X. R. Li, and T. Kirubarajan, *Estimation with applications to tracking and navigation.* New York, NY: Wiley, 2001.

[13] H. Robbins, "An empirical bayes approach to statistics," *Proceedings of the Third Berkeley Symposium on Mathematical Statistics and Probability*, vol. 1, pp. 157–164, 1955.

[14] J. S. Maritz and T. Lwin, *Empirical Bayes methods*. London: Chapman and Hall, 1989.

[15] X. R. Li, *Applied Estimation and Filtering*, vol. 3810. Course notes, University of New Orleans, 2005.

[16] H. Robbins, "Some thoughts on empirical bayes estimation," *The Annals of Statistics*, vol. 11, no. 3, pp. 713–723, 1983.

[17] H. Robbins, "Linear empirical bayes estimation of means and variances," *PNAS*, vol. 82, no. 6, pp. 1571–1574, 1985.

[18] B. J. Slocumb, "Surveillance radar range-bearing centroid processing," *Proceedings of SPIE - The International Society for Optical Engineering*, vol. 4473, pp. 74–85, 2001.

[19] M. J. Waxman and O. E. Drummond, "A bibliography of cluster (group) tracking," *Proceedings of SPIE*, vol. 5428, pp. 551–560, 2004.

[20] O. E. Drummond, S. S. Blackman, and G. C. Petrisor, "Tracking clusters and extended objects with multiple sensors," in *Proceedings of SPIE - The International Society for Optical Engineering*, vol. 1305, pp. 362–375, 1990.

[21] D. Lerro and Y. Bar-Shalom, "Interacting multiple model tracking with target amplitude feature," *IEEE Transactions on Aerospace and Electronic Systems*, vol. 29, no. 2, pp. 494–509, 1993.

[22] W. Koch and R. Saul, "A bayesian approach to extended object tracking and tracking of loosely structured target groups," in *The Proceedings of FUSION 2005, the 9th International Conference on Information Fusion*, 2005.

[23] J. W. Koch, "Bayesian approach to extended object and cluster tracking using random matrices," *IEEE Transactions on Aerospace and Electronic Systems*, vol. 44, no. 3, pp. 1042–1059, 2008.

[24] J. Dezert, "Tracking maneuvering and bending extended target in cluttered environment," in *Proceedings of SPIE - The International Society for Optical Engineering*, vol. 3373, pp. 283–294, 1998.

[25] T. J. Broida and R. Chellappa, "Estimating the kinematics and structure of a rigid object from a sequence of monocular images," *IEEE Transactions on Pattern Analysis and Machine Intelligence*, vol. 13, no. 6, pp. 497–513, 1991.

[26] D. Salmond and N. Gordon, "Group and extended object tracking," *IEE Colloquium (Digest)*, no. 90, pp. 72–75, 1999.

[27] B. Ristic, S. Arulampalam, and N. Gordon, *Beyond the Kalman filter: particle filters for tracking applications*. Boston, MA: Artech House, 2004.

[28] A. W. Rihaczek and S. J. Hershkowitz, "Choosing image intervals for small ships," in *Proceedings of SPIE - The Interntational Society of Optical Engineering*, vol. 3810, pp. 139–148, 1999.

[29] B. Ristic and D. J. Salmond, "A study of a nonlinear filtering problem for tracking an extended target," in *The Proceedings of FUSION 2004, the 7th International Conference on Information Fusion*, vol. 1, pp. 503–509, 2004.

[30] K. Gilholm and D. Salmond, "Spatial distribution model for tracking extended objects," in *IEE Proceedings on Radar, Sonar and Navigation*, vol. 152, pp. 364–371, 2005.

[31] Y. Boers, H. Driessen, J. Torstensson, M. Trieb, R. Karlsson, and F. Gustafsson, "Track-before-detect algorithm for tracking extended targets," in *IEE Proceedings on Radar, Sonar and Navigation*, vol. 153, pp. 345–351, 2006.

[32] R. V. Ostrovityanov and F. A. Basalov, *Statistical theory of extended radar targets*. Norwood, MA: Artech House, 1985. Translated from the Russian Statisticheskaya Teoriya Radiolokatsii Protyazhennyz Tselei by William F. Barton and David K. Barton.

[33] J. Romine and E. Kamen, "Modeling and fusion of radar and imaging sensor data for target tracking," *Optical Engineering*, vol. 35, no. 3, pp. 659–673, 1996.

[34] E. Oron, A. Kumar, and Y. Bar-Shalom, "Precision tracking with segmentation for imaging sensors," *IEEE Transactions on Aerospace and Electronic Systems*, vol. 29, no. 3, pp. 977–986, 1993.

[35] J. Romine, E. Kamen, and C. Sastry, "Fusion of radar and imaging sensor data for target tracking," in *Proceedings of SPIE - The International Society for Optical Engineering*, vol. 2235, pp. 558–569, 1994.

[36] S. O. Rice, "Mathematical analysis of random noise," *Bell Systems Tech. J.*, vol. 23, pp. 282–332, 1944.

[37] B. J. Slocumb and W. D. Blair, "Maximum likelihood narrowband radar data segmentation and centroid processing," *Proceedings of SPIE - The International Society for Optical Engineering*, vol. 5204, pp. 648–661, 2003.

[38] X. R. Li and V. P. Jilkov, "A survey of maneuvering target tracking - part iii: Measurement models," in *Proceedings of SPIE - The International Society for Optical Engineering*, vol. 4473, pp. 423–446, 2001.

[39] C. Arndt, *Information measures*. Springer Verlag, 2001.

[40] G. Hendeby and R. Karlsson, "Target tracking performance evaluation - a general software environment for filtering," in *Proceedings of the IEEE Aerospace Conference*, 2007.

[41] M. Stakkeland, G. Prytz, W. E. Booij, and S. T. Pedersen, "Characterization of accelerometers using nonlinear kalman filters and position feedback," *IEEE Transactions on Instrumentation and Measurement*, vol. 56, no. 6, pp. 2698–2704, 2007.

[42] E. Brekke, O. Hallingstad, and J. H. Glattetre, "Performance of pdaf-based tracking methods in heavy-tailed clutter," in *The Proceedings of FUSION 2009, the 12th International Conference on Information Fusion*, 2009.

[43] Z. Zhao, X. R. Li, and V. P. Jilkov, "Best linear unbiased filtering with nonlinear measurements for target tracking," *IEEE Transactions on Aerospace and Electronic Systems*, vol. 40, no. 4, pp. 1324–1336, 2004.

[44] A. Rødningsby and Y. Bar-Shalom, "Tracking of divers using a probabilistic data association filter with a bubble model," *To appear in IEEE Transactions on Aerospace and Electronic Systems*, 2009.

[45] S. Julier and J. Uhlmann, "A consistent, debiased method for converting between polar and cartesian coordinate systems," in *The Proceedings of AeroSense: The 11th International Symposium on Aerospace/Defense Sensing, Simulation and Controls*, 1997.

[46] S. Julier and J. Uhlmann, "Unscented filtering and nonlinear estimation," *Proceedings of the IEEE*, vol. 92, no. 3, pp. 401–422, 2004.

[47] J. Garcia, J. Molina, J. Besada, and G. de Miguel, "Model-based trajectory reconstruction using imm smoothing and motion pattern identification," in *The Proceedings of FUSION 2007, the 10th International Conference on Information Fusion*, 2007.

[48] J. D. Parker and W. D. Blair, "Use of target-oriented process noise in tracking maneuvering targets," tech. rep., Naval Surface Warfare Center, 1992.

[49] A. Papoulis, *Probability, random variables, and stochastic processes.* New York, NY: McGraw-Hill, 3 ed., 1991.

[50] W. D. Blair and B. M. Keel, *Multitarget-Multisensor Tracking: Applications and Advances Volume III*, ch. Radar Systems Modeling for Tracking, pp. 321–393. Norwood, MA: Artech House, 2000.

[51] J. O. Berger, *Statistical decision theory and Bayesian analysis.* New York, NY: Springer, 1985.

[52] B. Efron and C. Morris, "Stein's estimation rule and its competitors–an empirical bayes approach," *Journal of the American Statistical Association*, vol. 68, no. 341, pp. 117–130, 1973.

5

Paper one

Notation paper one

Notation	Definition
$\hat{x}^{LMMSE} = \hat{x}^{BLUE}$	LMMSE notation used in *paper one*, BLUE notation in rest of thesis

Estimating instantaneous false alarm rate in a CFAR system by Bayesian and empirical Bayesian methods

Morten Stakkeland
UniK University Graduate Center
Kjeller, Norway
Telephone: +47 64 84 47 00
Fax: +47 63 81 81 46
Email: mst@unik.no

X. Rong Li
Department of Electrical Engineering
University of New Orleans
New Orleans, LA 70148
Email: XLi@uno.edu

***Abstract*— In this paper it is shown that the instantaneous false alarm rate in a Constant False Alarm Rate (CFAR) system fluctuates from scan to scan and that Bayesian and Empirical Bayesian estimators can be applied to decrease the error between the actual and the assumed false alarm rate. The instantaneous false alarm rate is a random variable and its probability density function is derived for different system configurations. Bayesian estimators are applied in cases where analytical expressions of the mean and variance of the instantaneous false alarm rate can be derived. The mean square error in the estimated false alarm rate is shown to be less than the mean square variations of the instantaneous false alarm rate. Empirical Bayesian estimators are introduced and applied to cases where statistical properties of the false alarm rate are unknown. Empirical Bayesian estimators rely on past data to estimate the current false alarm rate and it is shown that they will converge asymptotically to the equivalent Bayesian estimators as the amount of past data gets large.**

I. Introduction

To have an accurate estimate of the clutter rate is important in target tracking, as more accurate knowledge of the clutter density can improve the performance of the tracking algorithm significantly. The nonparametric probabilistic data association filter (PDAF), a popular and cost-effective tracking and data association algorithm, estimates the clutter density using a diffuse prior [1]. In the integrated PDAF (IPDAF) [2], an expression which includes the track probability, the volume of the gate, the probability of a target being in the gate, the probability of detection and the predicted track quality is used to estimate the clutter density at each step. [3] extends these results and presents several estimators of the false alarm rate with both conditional mean estimation and maximum likelihood estimation.

None of these studies take into account that the thresholded measurements often are preprocessed by a CFAR clutter suppression algorithm whose goal is to keep the number of false alarm as constant as possible. This implies that the diffuse prior assumption in [1] is too pessimistic.

The false alarm rate of a radar signal processing system applying CFAR is well studied in the literature, an early example being given in [4]. A novel idea in this paper is to consider the average number of false alarms at each time as a random variable (rv), while the traditional approach has been to consider only the mean false alarm rate, $P_{FA} = \int_0^\infty \int_T^\infty f_x(x) f_T(T) dx dT$, where T is the threshold with probability density function (pdf) $f_T(T)$ and $f_x(x)$ is the pdf of the measured radar signal intensity of the cell under test.

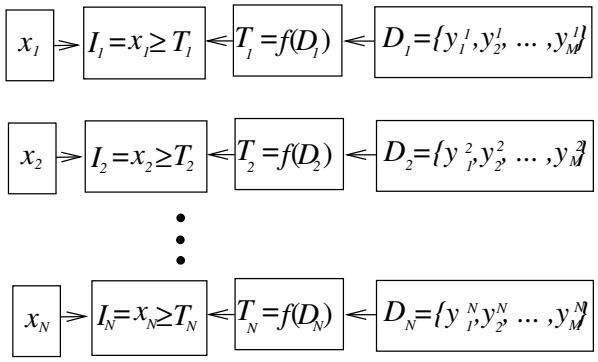

Fig. 1. Schematic setup of a general CFAR system

An estimate of the instantaneous false alarm rate at each scan can be made using the number of declared measurements from the CFAR system as input.

Section II contains background information and derivations regarding CFAR systems as well as an introduction to Bayesian and empirical Bayesian estimators. Some results are presented in section III while section IV concludes the study.

II. Background

A. CFAR systems

A CFAR system is often applied in order to detect targets in a noise background in systems where the statistics of the background may be unknown or changing over time or space. A schematic drawing of a general CFAR system is shown in fig. 1. N cells are under test, whose measured radar signal intensities are denoted $x_1, x_2, ..., x_N$. These cells are random variables with distributions $f_1, f_2, ..., f_N$ at each scan. The

distributions depend on the application, the radar system, and the applied signal processing. In a radar system the Rayleigh, Weibull, K-distribution and log-normal distributions are common models.

Each cell x_i is compared with a set of reference cells D_i via the function $T_i = f(D_i)$. If x_i is larger than T_i then $I_i = 1$ and a measurement in cell i is declared.

The function f is often a weighted sum, which classifies the system as a Cell Averaging CFAR (CA-CFAR). A CA-CFAR system is characterized by

$$f(D_i) = \frac{\alpha}{M} \sum\nolimits_{k=1}^{M} y_k^i \tag{1}$$

where α is a design parameter commonly used to control the mean false alarm rate P_{FA} and $y_1 ... y_M$ are the set of reference cells used to generate the threshold.

An Ordered Statistics CFAR (OS-CFAR) system is characterized by the ordered set $B^i = \left\{ y_{(1)}, y_{(2)}, ..., y_{(M)} \right\}$ which consists of the elements of D^i arranged such that $y_{(1)}^i \leq y_{(2)}^i \leq ... \leq y_{(M)}^i$. Then $f(D_i)$ is determined by an integer parameter $1 \leq K \leq M$ and the parameter α such that

$$f(D_i) = \alpha y_{(K)}^i. \tag{2}$$

Other variants of CFAR exist in the literature, but are not examined in this study. The results can easily be extended to other configurations and densities.

In systems where any structure or trends can be ignored or has been removed from the cells such that they have approximately similar statistical properties, the same threshold $T_i = T$ may be used for all i. This threshold may then be calculated as a function of all cells X or as a function of another set of cells with the same statistics.

1) CFAR instantaneous false alarm rate as a random variable: At each scan the threshold T_i is a function of a set of random variables and is thus itself a random variable. Given T_i and f_i the probability of false alarm in cell i is given exactly by the equation

$$p_i(T_i, f_i(x)) = \int_{T_i}^{\infty} f_i(x) dx$$

where $p_i \in [0, 1]$. This means that $p_i = P(I_i = 1)$ which is the probability for false alarm in cell i will change from time to time and is a random variable as well. As shown in example a) and b) below it may be possible in some cases to express the pdf of p_i analytically as $f_p(x)$.

2) The distribution of the number of false alarms: The following approximations and assumptions are made in order to obtain analytical expressions of the probability mass function (pmf) of the number of false alarms given a false alarm rate.

- The output from the N cells are independent both in time and space.
- The same threshold is applied to all the cells, $T_i = T = f(D)$ for all i.
- The correlation between x_i and T is zero or small enough to be ignored, for all k and i.
- No targets are present, the inclusion of these methods in the IPDAF algorithm is left for the future. Thus all measurements are false alarms.

If the approximations above hold then the number of false alarms at each scan will have a binomial distribution with parameter p_k because the sum $z = \sum_{i=1}^{N} I_i$ of N independent Bernoulli trials has a binomial distribution. The parameter p_k is here defined as the *instantaneous false alarm rate*, and is the estimatee in this study. The index $_k$ is omitted for simplicity in the rest of the study.

Thus given p, the number of false alarms z has the pmf

$$P(z = k|p) = \binom{N}{k} p^k \left(1 - p\right)^{N-k} \tag{3}$$

The mean and variance are given by $E(z|p) = Np$ and $\mathrm{var}(z|p) = Np(1-p)$.

a) Example: Assume that the clutter in the cells all are Rayleigh distributed and are passed through a square law detector, such that x_i has an exponential distribution,

$$f_i(x) = f_x(x) = \frac{1}{\lambda} \exp\left(-\frac{x}{\lambda}\right)$$

A CA-CFAR system is then used for clutter suppression. Using (1) and that the sum of N independent exponentially distributed rvs has a Gamma distribution, the threshold T has the density

$$f_T(x) = \frac{x^{N-1} \exp\left(\frac{-x}{\left(\frac{\alpha\lambda}{N}\right)}\right)}{\left(\frac{\alpha\lambda}{N}\right)^N \Gamma(N)}$$

and the cumulative distribution function (cdf)

$$F_T(x) = P(T \leq x) = \frac{\Gamma\left(N, \frac{x}{\left(\frac{\alpha\lambda}{N}\right)}\right)}{\Gamma(N)}$$

where $\Gamma(x)$ is the Gamma function and $\Gamma(x, y)$ is the incomplete Gamma function. Note that

$$\begin{aligned} F_p(x) &= P(p \leq x) = P\left(\int_{T_i}^{\infty} f_i(y) dy \leq x\right) \\ &= P\left(\int_{T}^{\infty} \frac{1}{\lambda} \exp\left(-\frac{y}{\lambda}\right) dy \leq x\right) \\ &= P\left(\exp\left(-T/\lambda\right) \leq x\right) = P\left(T \geq \lambda \ln x\right) \\ &= 1 - \frac{\Gamma\left(N, -\frac{N}{\alpha} \log x\right)}{\Gamma(N)} \end{aligned}$$

The pdf of the rv p is the derivative of $F_p(x)$.

$$f_p(x) = \frac{dF_p(x)}{dx} = \frac{N^N \left(\log \frac{1}{x}\right)^{N-1} x^{-\frac{\alpha - N}{\alpha}}}{\alpha^N \Gamma(N)} \tag{4}$$

where x is defined on the interval $[0, 1]$. This gives

$$\bar{p} = E(p) = P_{FA} = \int_0^1 x f_p(x) dx = \left(1 + \frac{\alpha}{N}\right)^{-N} \tag{5}$$

$$\sigma_p^2 = var(p) = \int_0^1 (x - E(p))^2 f_p(x) dx$$
$$= \left(\frac{2\alpha}{N} + 1\right)^{-N} - \left(\frac{\alpha}{N} + 1\right)^{-2N} \quad (6)$$

Equation (5) is a well known result in the literature. Note that the pdf $f_p(x)$ is independent of the noise power λ.

b) Example: In this example the clutter has the more general Weibull distribution, and the signal processing apply linear detection and an OS-CFAR configuration. The density and distribution of the cells x_i are then given by

$$f_x(x) = \frac{\gamma}{\mu}\left(\frac{x}{\mu}\right)^{\gamma-1} \exp\left(-\left(\frac{x}{\mu}\right)^{\gamma}\right)$$
$$F_x(x) = 1 - \exp\left(-\left(\frac{x}{\mu}\right)^{\gamma}\right)$$

Using that in an ordered set, cell number K has the pdf [5]

$$f_{y_{(K)}}(x) = K\binom{N}{K} F_x(x)^{K-1} \left(1 - F_x(x)\right)^{N-K} f_x(x)$$

$T = \alpha y_{(K)}$ then has pdf $f_T(x) = \frac{1}{\alpha} f_{y_{(K)}}(\frac{x}{\alpha})$. Given that $p = g(T) = \int_T^\infty f_x(x)dx$ and let $\tilde{T}$ be the solution of $p = g(T)$ with respect to T, then the pdf of p is given by the transformation

$$f_p(x) = \frac{f_T(\tilde{T})}{|g'(\tilde{T})|}$$
$$= \frac{K}{\alpha^\gamma}\binom{N}{K}\left(1 - x^{\alpha^{-\gamma}}\right)^{K-1} x^{\alpha^{-\gamma}(N-K+1)-1}$$

This gives

$$E(p) = \frac{\Gamma(N+1)\Gamma(N-K+\alpha^\gamma+1)}{\Gamma(N-K+1)\Gamma(N+\alpha^\gamma+1)}$$

$$\sigma_p^2 = (\Gamma(N+1)\Gamma(N-K+2\alpha^\gamma+1)\Gamma(N-K+1) \quad (7)$$
$$\cdot \Gamma(N+\alpha^\gamma+1)^2 - \Gamma(N+1)^2\Gamma(N-K+\alpha^\gamma+1)$$
$$\cdot\Gamma(N+2\alpha^\gamma+1)) \,/\, \left(\Gamma(N-K+1)^2\Gamma(N+2\alpha^\gamma+1)^2\right.$$
$$\left.\cdot\, \Gamma(N+\alpha^\gamma+1)^2\right)$$

See that the pdf $f_p(x)$ is independent of the scale parameter μ, but depends on the shape parameter γ as well as the system design parameters α and K.

c) Notes on σ_p^2: As shown above the instantaneous false alarm rate is a rv. The name Constant false alarm rate reflects the fact that the mean false alarm rate P_{FA} is independent of the mean clutter power/amplitude in some applications. The variance σ_p^2 can be seen as a measure of the fluctuations in the instantaneous clutter rate from scan to scan, and could be useful information. The larger σ_p^2 is the more the number of false alarms will fluctuate from scan to scan and the system designer of may want to control the variance in addition to P_{FA}.

In addition σ_p^2 can be used as a measure of the CFAR loss. Previous definitions include the increase of signal to clutter ratio needed to maintain a given P_D for a specific target, and the variations in the parameter α as defined by [6]. Using σ_p^2 has the advantage of not being dependent on a specific target and in addition being a more intuitive measure than the variations in α.

B. Bayesian estimation

In classical estimation the estimatee is considered to be an unknown constant which is estimated from a set of noisy data. Bayesian estimation differs fundamentally from this in the way that the estimatee is modeled as a random variable, with a prior probability density function $f(x)$. Given the estimatee x, the measurements are then assumed to be distributed according to a likelihood function denoted $f(z|x)$. The estimate is based on the the posterior density $f(x|z)$ which is the pdf of the estimatee given a set of measurements. This pdf can be obtained using Bayes' law

$$f(x|z) = \frac{f(z|x)f(x)}{f(z)} = \frac{f(z|x)f(x)}{\int f(z|x)f(x)dx}$$

Once the posterior density has been calculated, an estimate can be obtained using several different approaches. One possibility is the conditional mean defined by

$$\hat{x}^{MMSE} = E\left(x|z\right) = \int x f(x|z) dx \quad (8)$$

The conditional mean is called the Minimum Mean Square Error (MMSE) because it can be shown to minimize the mean square error of the estimator [7]. The Maximum A Posteriori (MAP) estimator is another possible candidate and is defined by $\hat{x}^{MAP} = \arg\max_x f(x|z)$.

C. LMMSE estimation

The linear MMSE (LMMSE) estimator is given by [7]

$$\hat{x}^{LMMSE} = \bar{x} + C_{xz}C_z^{-1}(z - \bar{z}) \quad (9)$$

$$\hat{P} = MSE(\hat{x}) = C_x - C_{xz}C_z^{-1}C_{zx} \quad (10)$$

$\bar{x} = E(x)$ is the mean of the estimatee, $C_{xz} = E\left(\left(x - \bar{x}\right)\left(z - \bar{z}\right)^T\right)$ is the covariance between the estimatee and the measurements, $C_z = \left(\left(z - \bar{z}\right)\left(z - \bar{z}\right)^T\right)$ is the measurement covariance, and $\bar{z} = E(z)$ is the measurement mean. $MSE(\hat{x})$ is the Mean Square Error of the estimator

To obtain a closed form expression of the conditional mean in equation (8) is often hard. The LMMSE estimator is easier to implement because it is linear and only depends on the first two moments of x and z. Among its important properties is that it is unbiased $E(x - \hat{x}) = 0$ and the best estimator in the mean square error sense within the class of linear Bayesian estimators [7].

1) Instantaneous false alarm rate LMMSE estimate: Assume that the instantaneous false alarm rate is a random variable with pdf

$$x \sim \begin{cases} 0 & x < 0 \\ f_x(x) & 0 \leq x \leq 1 \\ 0 & 1 < x \end{cases} \tag{11}$$

Assume $E(z|x) = Nx$ and $\text{var}(z|x) = Nx(1-x)$. Then,

$$\bar{z} = E[z] = E[E(z|x)] = E[Nx] = N\bar{x}$$
$$E[(z-\bar{z})|x] = E[z|x] - \bar{z} = Nx - N\bar{x}$$

$$\begin{aligned} C_{zx} &= E[(z-\bar{z})(x-\bar{x})] = E[E[(z-\bar{z})(x-\bar{x})|x]] \\ &= E[E[(z-\bar{z})|x](x-\bar{x})] = E[(Nx-N\bar{x})(x-\bar{x})] \\ &= N\,\text{var}(x) = NC_x \end{aligned} \tag{12}$$

Using that $C_z = E[\text{var}(z|x)]+\text{var}[E(z|x)]$ [8] gives

$$\begin{aligned} C_z &= E[\text{var}(z|x)] + \text{var}[E(z|x)] = E[Nx(1-x)] + \text{var}[Nx] \\ &= N\bar{x} - N(C_x + \bar{x}^2) + N^2 C_x \\ &= N[\bar{x}(1-\bar{x}) + (N-1)C_x] \end{aligned} \tag{13}$$

Inserting equation (12) and (13) into (9) and (10) gives

$$\begin{aligned} \hat{x}(k) &= \bar{x} + C_{xz}C_z^{-1}(z-\bar{z}) \\ &= \bar{p} + \frac{\sigma_p^2}{\bar{p}(1-\bar{p}) + (N-1)\sigma_p^2}(k - N\bar{p}) \end{aligned} \tag{14}$$

$$\begin{aligned} MSE(\hat{x}) &= C_x - C_{xz}C_z^{-1}C_{zx} \\ &= \sigma_p^2 \left(\frac{\bar{p}(1-\bar{p}) - \sigma_p^2}{\bar{p}(1-\bar{p}) + (N-1)\sigma_p^2} \right) \end{aligned} \tag{15}$$

Fig. 2 gives an illustration of the effect of the linearization. The plot shows the difference between the MMSE and LMMSE estimates of the instantaneous clutter density for a given measurement. The MMSE estimates are obtained using numerical integration of (8). The probability that k is greater than 30 is on the order of 10^{-4}, giving that the deviation between the two estimators is relatively small within the interval where the measurements are most likely to be found. Note that the LMMSE estimator minimizes the average mean square error over all possible measurements in the class of linear estimators, not the mean square error for each possible z.

D. Empirical Bayesian estimation

The term Empirical Bayes (EB) estimation was introduced by Robbins [9], and can be described as a compromise between classical and Bayesian estimation. The main classical criticism against Bayesian estimation is that choosing a prior distribution may be difficult, and that the choice may be highly subjective. On the other hand classical estimation ignores the existence of any prior information about the estimatee, and does inference based entirely on current measurements.

The main idea behind EB estimation is to use past data to estimate the prior density of the estimatee $f(x)$. Assume that

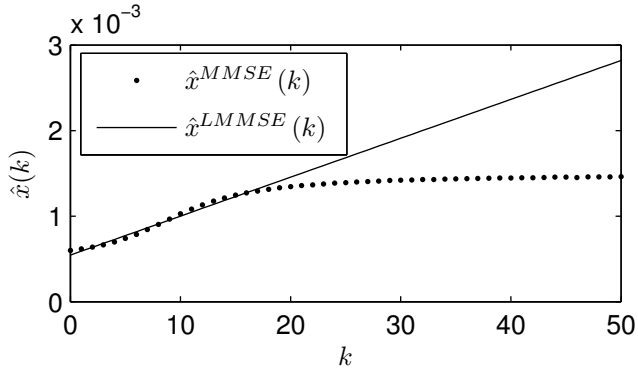

Fig. 2. Difference between LMMSE estimate and MMSE estimate, p uniformly distributed on $[0.5, 1.5]10^3$, $P_{FA} = 10^3$, and $N = 10^4$.

	Past data			**Current data**
Realizations	x_1	...	x_{l-1}	x_l
Measurements	z_2	...	z_{l-1}	z_l

all past data $x_1, x_2, ..., x_{l-1}$ and the current x_l are independent and distributed according to the unknown density $f(x)$, and are observed through the measurements z_1 to z_l.

EB estimators are sometimes divided into two classes, parametric and nonparametric [10]. The parametric approach makes the assumption that the prior belongs to a family of densities, and then seeks to estimate which member of this family the prior belongs to. For example the prior can be assumed to be a Gaussian distribution, and the mean and variance is estimated using past data. These methods are often attributed to Efron and Morris [11].

In the nonparametric approach, the previous realizations $x_{1\to l-1}$ are often assumed to be independent and identically distributed (i.i.d). The empirical density of the past measurements $\hat{f}(z)$ is estimated, and then an estimate of the prior density $\hat{f}(x)$ is determined such that $\hat{f}(z) \approx \int f(z|x)\hat{f}(x)dx$ with the property $\hat{f}(x) \to f(x)$ as $l \to \infty$. This is usually not easy, but in many cases it may not be necessary to obtain an explicit expression of $\hat{f}(x)$ in order to obtain an estimate $\hat{x}_l$.

In general as the amount of data gets large, empirical Bayesian estimators will converge to the corresponding Bayesian estimator. See for instance [12] for a discussion of the asymptotical convergence of EB estimators.

The assumption that the past realizations of x are i.i.d, implies that the correlation between each scan needs to be zero and that the pdf of p needs to be constant over time. For instance this implies that a change in the shape parameter of the Weibull distribution means that a new set of past data should be collected.

E. Linear empirical Bayesian estimation (LEB)

A scalar general linear nonparametric EB estimator is described by Robbins [13]. This estimator can be extended to the more general vector case. In cases where the likelihood

function $f(z|x)$ satisfies

$$E(z|x) = x \tag{16}$$

$$\mathrm{cov}(z|x) = A + bx^T + xb^T + ax^T x \tag{17}$$

where A, b and a are constants, then the LEB estimator is given by

$$\hat{x}^{LEB} = \hat{z} + \frac{1}{1+a}\left(I - \left(\hat{\sigma}^2\right)^{-1}\left(A + b\hat{z}^T + \hat{z}b^T + a\hat{z}^T\hat{z}\right)\right) \cdot (z_k - \hat{z})$$

where $\hat{z}$ and $\hat{\sigma}^2$ is the sample mean and covariance of the past data. The LEB estimator is the empirical equivalent of the LMMSE estimator, and the LEB estimator will converge to the LMMSE estimator in a MSE sense as the number of measurements gets large.

1) Instantaneous false alarm rate LEB estimation [8]: Defining the measurements as $z_i = k_i/N$ where k_i is the measured number of false alarms in each scan gives $E(z|p) = E(\frac{k}{N}|p) = \frac{1}{N}E(k|p) = \frac{1}{N}Np = p$ and $var(z|p) = var\left(\frac{k}{N}|p\right) = \frac{1}{N^2}Np\left(1-p\right) = p\left(1-p\right)/N$. Thus the two conditions in equation (16) and (17) hold with $A = 0$, $b = 1/2N$, $a = -1/N$. This gives

$$\hat{p}^{LEB} = \hat{z} + \frac{N}{N-1}\left(1 - \frac{\hat{z}\left(1-\hat{z}\right)}{N\hat{\sigma}^2}\right)(z - \hat{z})$$

where z is the current measurement, and $\hat{z}$ and $\hat{\sigma}^2$ are the sample mean and variance of the past measurements.

Another scalar false alarm rate LEB estimator which has better properties for small l and allows variations in the size of the set of cells at each scan is derived in [14]. The estimator is given by

$$\hat{p}^{LEB} = \bar{z} + \frac{\left(\left(1-\frac{v}{L}\right)\hat{\sigma}^2 - v\hat{z}(1-\hat{z})\right)^+}{\left(\left(1-\frac{v}{L}\right)\hat{\sigma}^2 - v\hat{z}(1-\hat{z})\right)^+ + \frac{1}{N_l}\left(\hat{z}(1-\hat{z}) - \left(1-\frac{1}{L}\right)\hat{\sigma}^2\right)^+} \cdot (z_l - \hat{z}) \tag{18}$$

where $z_i = k_i$, $(A)^+ = \max(0, A)$, L is the number of past measurements, N_i is the size of the set of cells, $v = \frac{1}{L}\sum_{i=1}^{L}\frac{1}{N_i}$, and $\hat{z}$ and $\hat{\sigma}^2$ are the sample mean and variance. The two estimators coincide for fixed N_i and large L.

III. Results

As shown in fig. (3), the Root Mean Square Error (RMSE) of the LEB estimator converges to the RMSE of the LMMSE estimator. However, the rate of convergence varies with the parameter of the system, and may have to be tested by simulations for a given system, specifically the product $N \cdot P_{FA}$. This makes intuitive sense, as it would take a long time to obtain a good estimate of the statistics of the false alarm rate when false alarms occur rarely.

As argued in section II-A.2.c, σ_p^2 can be used as a measure of the fluctuations in the instantaneous clutter rate from scan to scan. The mean square error of considering the instantaneous clutter rate as a constant is thus equal to σ_p^2 which is given

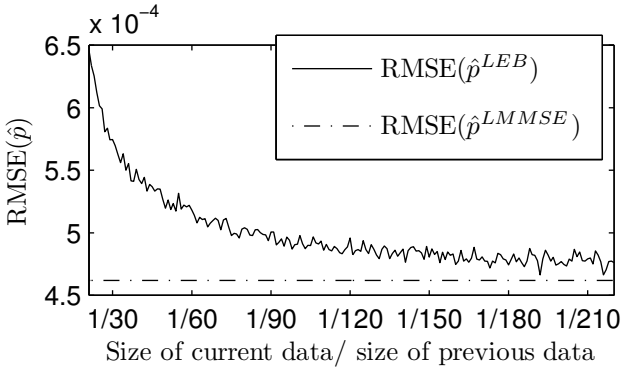

Fig. 3. Root Mean Square Error of the LEB estimator, where p has a truncated Rayleigh distribution with $P_{FA} = 10^{-3}$ in a CA-CFAR system with $N = 10^3$ cells compared with the RMSE of the LMMSE estimator. Mean over 10^4 Monte Carlo runs.

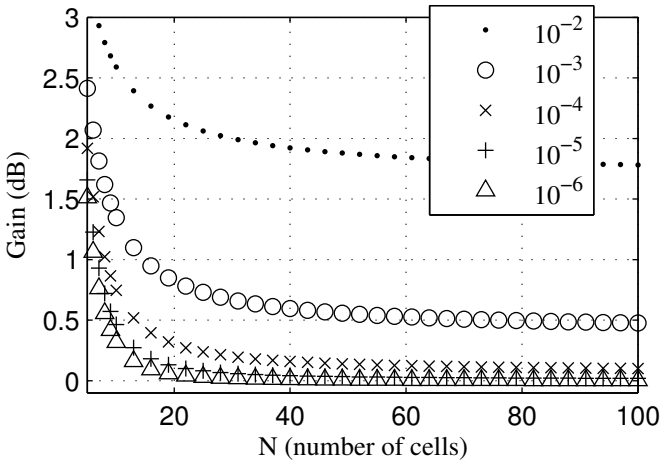

Fig. 4. Gain as a function of the number of cells, N. CA-CFAR system, P_{FA} kept constant by adjusting a for different P_{FA}'s. Cells with Rayleigh distribution.

in (6) and (7) for the two system configurations previously considered. The mean square error in the LMMSE estimator is given by equation (15), denoted $MSE(\hat{x}^{LMMSE})$. In order to compare the two errors, defined

$$G = \left[\frac{\sigma_p^2}{MSE(\hat{x}^{LMMSE})}\right]_{dB}$$

as a measure of the gain in the system when the clutter rate is treated as a known constant, rather than estimated by the LMMSE estimator (or the LEB estimator with a large amount of past data).

The results for the CA-CFAR configuration in section II-A.2.a generates the results shown in fig. 4. The gain is seen to depend on the mean false alarm rate, P_{FA}, and the estimation gives more gain for a higher P_{FA}. It is also clear from the figure that the gain in estimating the clutter rate gets smaller as the number of cells increases and thus σ_p^2 decreases.

Fig. 5 shows an analysis of how the gain depends on the

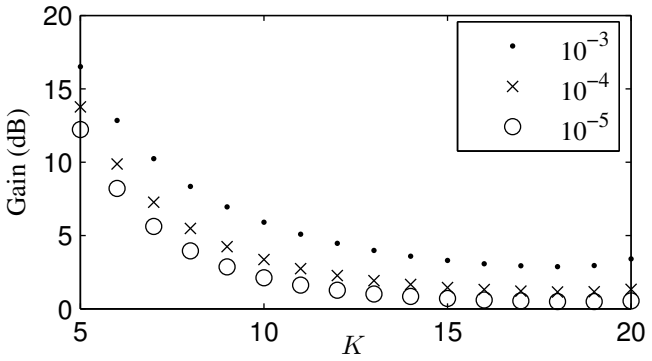

Fig. 5. Gain as function of the choice of system parameter K for different false alarm rates, P_{FA}. OS-CFAR system, $N = 20$. Cells with Weibull distribution, result independent of shape parameter γ

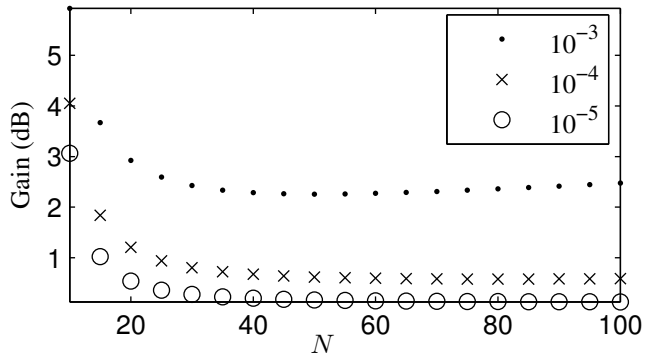

Fig. 6. Gain as a function of the number of cells, N. OS-CFAR, $K = N-3$. Cells with Weibull distribution, result independent of shape parameter γ

choice of system parameter K in an OS-CFAR system where $f_x(x)$ is the Weibull distribution. The variance σ_p^2 can be shown to be independent of the choice of the Weibull shape parameter when P_{FA} is kept constant by adjusting α, thus L depends only on P_{FA} and K.

Fig. 6 is an analysis of how L depends on the number of cells N in a OS-CFAR system. As for the CA-CFAR configuration in fig. 4, the gain decreases as N gets larger, and higher for lower P_{FA}. The parameter K is chosen to be $N-3$ for a given N, but other choices of K will give different results.

IV. Conclusion

The derivations in section II.A have shown that the instantaneous false alarm rate in a CFAR system is a random variable, not a constant. The mean false alarm rate may on the other hand be constant and independent of the mean power of the background for some configurations and distributions, for instance a CA-CFAR system when the background has the Rayleigh distribution.

The examples in section II.A show that it in some cases is possible to obtain closed form expressions of the first and second moments of the instantaneous false alarm rate, $\bar{p} = P_{FA}$ and σ_p^2. LMMSE estimators can then be applied to decrease the error between the real and the assumed false alarm rate. The mean square error obtained in the system when assuming that the false alarm rate is constant and equal to its mean P_{FA}, is given by the variance σ_p^2. It is shown that the mean square error of the estimated instantaneous false alarm rate is smaller than σ_p^2. The gain by estimating the instantaneous false alarm rate from scan to scan is shown to depend on the CFAR system configuration. In general the gain is high for large P_{FA} and σ_p^2.

In cases where P_{FA} and σ_p^2 are unknown, LEB estimators can be applied to the problem and asymptotically achieve the same mean square error as the LMMSE estimator. P_{FA} and σ_p^2 may be unknown because the distribution of the background $f_x(x)$ is unknown, or because it may be impossible to solve the necessary equations analytically.

We are not aware of any previous applications of Empirical Bayesian estimation in engineering, but it is shown here how the method can be applied when the prior distribution of the estimatee is unknown. Empirical Bayesian estimators in general converges to the corresponding Bayesian estimator, but the rate of convergence depends on the application.

V. Acknowledgement

Dr. Øyvind Overrein from Applied Radar Physics is thanked for valuable discussions and feedback on CFAR systems and configurations.

References

[1] Y. Bar-Shalom and X. R. Li, *Multitarget-multisensor tracking : Principles and techniques*. Storrs, Conn.: YBS, 1995.

[2] D. Musicki, R. Evans, and S. Stankovic, "Integrated probabilistic data association," *IEEE Transactions on Automatic Control*, vol. 39, no. 6, pp. 1237–1241, 1994.

[3] X. R. Li and N. Li, "Integrated real-time estimation of clutter density for tracking," *IEEE Transactions on Signal Processing*, vol. 48, no. 10, pp. 2797–2805, 2000.

[4] H. Rohling, "Radar cfar thresholding in clutter and multiple target situations." *IEEE Transactions on Aerospace and Electronic Systems*, vol. AES-19, no. 4, pp. 608–621, 1983.

[5] A. Papoulis, *Probability, random variables, and stochastic processes*, 3rd ed. New York: McGraw-Hill, 1991.

[6] S. Watts, "The performance of cell-averaging cfar systems in sea clutter," in *The Record of the IEEE 2000 International Radar Conference*, 2000, pp. 398–403.

[7] Y. Bar-Shalom, X. R. Li, and T. Kirubarajan, *Estimation with applications to tracking and navigation*. New York: Wiley, 2001.

[8] X. R. Li, *Applied Estimation and Filtering*. Course notes, University of New Orleans, 2005.

[9] H. Robbins, "An empirical bayes approach to statistics," *Proceedings of the Third Berkeley Symposium on Mathematical Statistics and Probability*, vol. 1, pp. 157–164, 1955.

[10] J. O. Berger, *Statistical decision theory and Bayesian analysis*. New York: Springer, 1985.

[11] B. Efron and C. Morris, "Stein's estimation rule and its competitors–an empirical bayes approach," *Journal of the American Statistical Association*, vol. 68, no. 341, pp. 117–130, mar 1973.

[12] J. S. Maritz, *Empirical Bayes methods*, T. Lwin, Ed. London: Chapman and Hall, 1989.

[13] H. Robbins, "Some thoughts on empirical bayes estimation," *The Annals of Statistics*, vol. 11, no. 3, pp. 713–723, Sep. 1983.

[14] ——, "Linear empirical bayes estimation of means and variances," *PNAS*, vol. 82, no. 6, pp. 1571–1574, 1985.

6

Paper two

Notation paper two

Notation	Definition
m_k	State of Markov chain at time t_k in *paper two*, number of kinematic measurements in chapter 2 and *paper one*.

Tracking and fusion of surveillance radar images of extended targets

Morten Stakkeland, Oddvar Hallingstad
UniK University Graduate Center
Kjeller, Norway
mst@unik.no, oh@unik.no

Øyvind Overrein
Applied Radar Physics
Kjeller, Norway
overrein@arp.no

Abstract – Range and angle measurement errors may be correlated when centroid image processing is applied on radar images of extended targets. This paper describes how a model of the correlation between target heading and measurement error can be used to improve the accuracy of tracking filters. The performance of the presented tracking algorithms is tested using a trajectory generator based on jump Markov nonlinear systems.

Keywords: target tracking, extended targets, measurement models, surveillance radar

1 Introduction

The targets in a radar surveillance system may in some applications be located very close to the radar. The spatial resolution of a radar is increasing as r gets small, which means that a target close to the radar may be larger than the resolution of the sensor. A target is in this paper called extended if its extent covers several resolution cells both in range and angle.

A common assumption when including radar measurements in a tracking system is that range and angle measurements are uncorrelated. However the work in [1] shows that this assumption may fail when centroid processing is applied to extract a position measurement from raw 2D radar images. It is shown how the assumption is true for point targets, but may fail for extended targets. There may be correlation between the heading of the object and the measurement error statistics. It may in some cases be reasonable to assume that the eigenvectors of the measurement matrix are aligned with the main axes of the target.

In order to utilize this information in tracking filters, this paper introduces a new measurement model. Several different filters based on the IMM framework given by [2] are implemented with the new measurement model. The performance of the proposed filters is compared to that of filters that ignore the correlation between target heading and measurement error.

A trajectory generator which can generate realistic simulated target movements is developed in order to compare the performance of the different estimators. The generator is based on a jump Markov nonlinear system (JMNLS) and switches randomly between different modes of movement.

Section two contains descriptions of the applied measurement models and the proposed trajectory generator. It also contains background information about surveillance radar images and Jump Markov (JM) systems. Some simulation results are shown in section three, section four contains a discussion, while section five concludes the study.

2 Background

2.1 Surveillance radar images

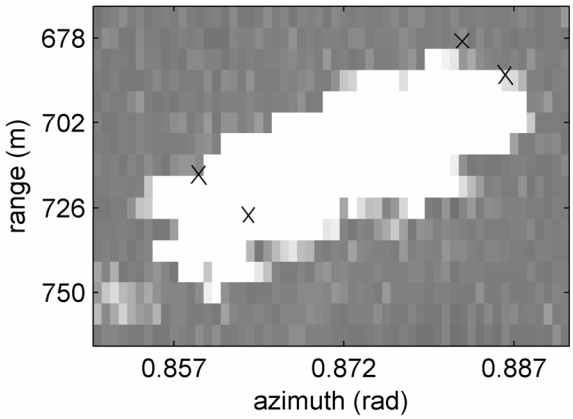

Figure 1 Grayscale representation of radar image of a ship with dimensions 40 x 9 m. Corners indicated by x. 6m sampling rate in range, rectangular pulse, pulse length ~25 m. $2\pi/4096$ sampling rate in azimuth, 0.5 deg beam width.

The number of scattering points and planes that contribute to the electromagnetic field measured by the radar is determined by the resolution of the system as well as the geometry of the target. Figure 1 shows a 2D surveillance radar image of a commercial ferry located about 700 m from the sensor. The figure shows how the system is unable to resolve individual scattering objects on the ferry.

The resolution of a system which apply a rectangular pulse waveform is determined by the pulse length and the lobe width of the antenna. Figure 1 shows how the

sampling in range and azimuth may be more spatially dense than the actual resolution of the system. The number of pixels covered by the target image is determined by the sampling frequency in range and azimuth as well as the resolution.

Identification of some individual strong reflectors on the target like for instance corner reflectors could be possible, given that the resolution was high enough. The individual objects could then be tracked as a group described by for instance [3]. However, in addition to the limitations on spatial resolution, the ability to resolve individual scattering objects may also be limited by the dynamic range of the system and poor resolution in the ADCs. These effects can be seen in Figure 1 where the dynamic range of the systems is sampled with 8 bit ADCs as it is commonly done in the civilian sector. Many pixels are saturated on the highest bit level. The dynamic range of the system may often be optimized with respect to detection of dim targets, not in order to accurately measure the reflected amplitude from the strongest reflectors on extended targets.

Because of the limitations described above and the high demand on computational efficiency often encountered in a surveillance system, the centroid image processing described in section 2.2 is a commonly chosen solution.

2.2 Centroid image processing

An overview of the signal processing setup often applied in 2D surveillance radar systems [4], is shown in Figure 2.

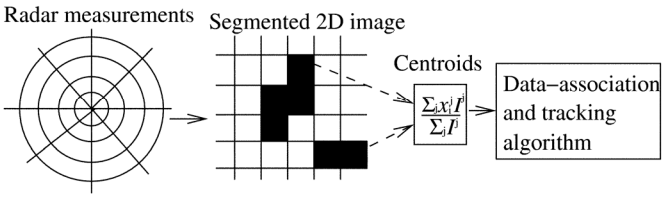

Figure 2 Signal processing chain

The signal measured in each pixel may have fluctuations from scan to scan due to interference between the returned fields from each scattering object in the resolution cell. This phenomenon is sometimes called speckle noise, and its distribution tends to Gaussian as the number of scatterers increases.

Each pixel also contains a contribution of thermal noise introduced by the analog signal processing. The amplitude is sometimes modeled to have a Ricean distribution [5]. Many other sources contribute to image noise as well, as for instance multi path, interfering reflecting objects in the side lobes, and solar/galactic noise.

The 2D centroid position measurements are given by

$$z_x = \sum_j x^j I^j \Big/ \sum_j I^j \qquad (1)$$

$$z_y = \sum_j y^j I^j \Big/ \sum_j I^j \qquad (2)$$

where j runs over all the pixels covered by the target image and I^j is the value measured in pixel number j. It is clear from (1) and (2) that the two centroids z_x and z_y are not independent because the non-deterministic intensities I^j appear in both equations. They are however in some cases uncorrelated.

2.3 Error statistics of centroid measurements

The work in [6] derives the statistics of the centroid of a random cluster under the assumption that the pixels are independent. It is shown that the variance of the measurement in each coordinate is given by

$$\mathrm{var}\left(z_x\right) = \frac{\sum_{j=1}^{N} x^j \,\mathrm{var}\left(I^j\right)}{\left(\sum_{j=1}^{N} E\left(I^j\right)\right)^2},\ \mathrm{var}\left(z_y\right) = \frac{\sum_{j=1}^{N} y^j \,\mathrm{var}\left(I^j\right)}{\left(\sum_{j=1}^{N} E\left(I^j\right)\right)^2} \qquad (3)$$

Equation (3) is derived using a Taylor expansion, following [7]. By doing a Taylor expansion in the same manner, the results in [6] could be extended with the following equation,

$$C_{xy} = \mathrm{cov}\left(z_x, z_y\right) = \frac{\sum_{j=1}^{N} x^j y^j \,\mathrm{var}\left(I^j\right)}{\left(\sum_{j=1}^{N} E\left(I^j\right)\right)^2} \qquad (4)$$

Equation (3) and (4) will in general not be valid for radar measurements because neighbor pixels often are correlated. Approximations of $E\left(I^j\right)$ and $\mathrm{var}\left(I^j\right)$ will also be hard to derive in cases where the target image is dominated by speckle noise.

2.3.1 Radar measurement error statistics

When radar measurements are included in a tracker, it is common to assume that range measurement errors are independent from angle errors [8, 9]. In 2D this can be written as

$$\begin{bmatrix} z_r \\ z_\phi \end{bmatrix} = \begin{bmatrix} r \\ \phi \end{bmatrix} + \begin{bmatrix} v_r \\ v_\phi \end{bmatrix} \qquad (5)$$

where $E\left(v_r^2\right) = \sigma_r^2$, $E\left(v_\phi^2\right) = \sigma_\phi^2$ and $E\left(v_r v_\phi\right) = 0$.

The work in [1] shows how this assumption fails when centroid processing is applied and the target is extended with respect to the resolution of the sensor. [1] applies Monte Carlo simulations and simplified models of both the target and the analog signal processing. It is shown how there may be correlation between the measurement error covariance and the heading of the target.

Figure 3 shows a set of simulated measurements where the target is kept fixed with respect to the radar. The range errors in each measurement lies on the x-axis with a deterministic bias of one half pulse length, while

the errors along the y-axis are $r \cdot \Delta\phi$. The plot shows that there is correlation between angular and range measurement errors. The figure also indicates that there is correlation between the heading of the target and measurement errors.

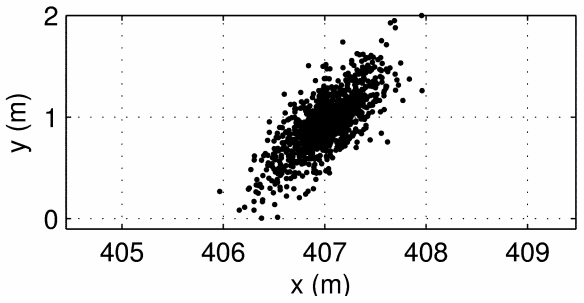

Figure 3 One batch of simulated position measurements. Radar located at origo, 40x9 m rectangular target located at (x,y)=(400,0) m. Range resolution 12 m. Target heading 45°.

Using modeled targets with rectangular shape and a high numbers of reflecting scatterers distributed uniformly over the target, [1] shows that for short ranges when targets are extended in range and azimuth, the following equation is a good approximation. The measurement error covariance matrix can be approximated in Cartesian coordinates by

$$R_k = E\left(v_k v_k^T\right) = \Theta_k R_0 \Theta_k^T = \begin{bmatrix} \cos\theta_k & -\sin\theta_k \\ \sin\theta_k & \cos\theta_k \end{bmatrix} \begin{bmatrix} \sigma_a^2 & 0 \\ 0 & \sigma_t^2 \end{bmatrix} \begin{bmatrix} \cos\theta_k & \sin\theta_k \\ -\sin\theta_k & \cos\theta_k \end{bmatrix} \quad (6)$$

The matrix Θ_k is the rotation matrix defined by the heading of the target θ_k. v_k is the additive measurement noise, $z_k = h(x_k) + v_k$.

The variances σ_a^2 and σ_t^2 can then be viewed as the variances along and in transverse direction of the main axes of the target. σ_a^2 and σ_t^2 are shown to depend on the distance to the target, the signal to noise ratio (SNR), the resolution of the system and the target geometry. For a square target, $\sigma_a^2 = \sigma_t^2$

Figure 4 shows values of σ_a and σ_t calculated from a series of simulation. The simulated target had dimensions of 40 x 9 m and the system had a range resolution of 6 m and an angular resolution of 0.5°. Figure 5 shows the measurement uncertainties expressed in polar coordinates, based on the same data set. Notice how σ_r increases with *r,* while it is commonly assumed to be constant.

As the target approaches a point target at long range, the work in [1] show that the correlation between target heading and measurement uncertainty goes to zero. This means that equation (5) is true as *r* gets large and the target becomes a point target in azimuth.

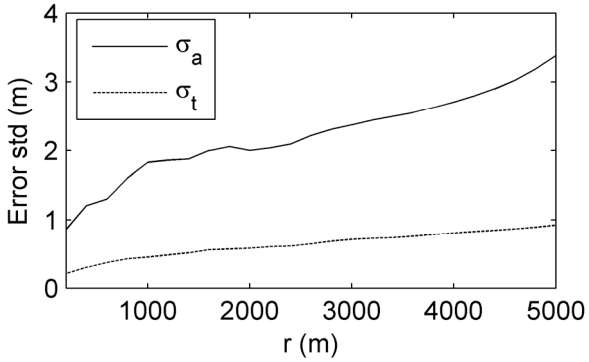

Figure 4 Estimated standard deviations along the main axis and the transverse axis of the target.

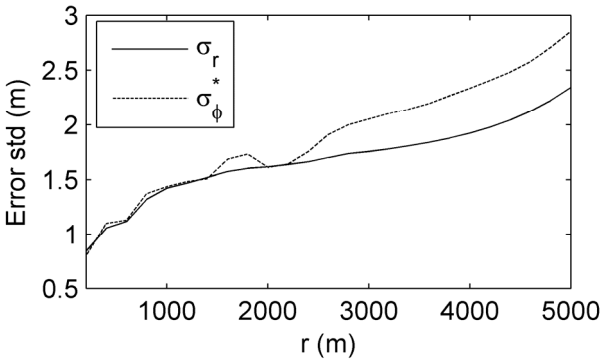

Figure 5 Estimated standard deviations in polar coordinates, where $\sigma_\phi^* = r\sigma_\phi$.

2.4 Measurement modeling and fusion

In some applications it is necessary to fuse radar measurements with other measurements, for instance with data from imaging sensors as described by [10]. Fusion of radar measurements may also be possible, when several radars cover the same target. Correct statistical models of the measurement errors are needed to do optimal measurement fusion.

Thus at short ranges, knowledge of the heading of the target can be used together with equation (6) to do better measurement fusion. The measurement uncertainty can be approximated by the normal distribution. As shown in Figure 4, the measurement uncertainties along and in transverse direction of the heading of the target is a function of range. This means that σ_a^2 and σ_t^2 in equation (6) should be functions of the distance from the sensor, $\sigma_a(r)$ and $\sigma_t(r)$.

Equation (5) can be used at long ranges. When *r* is large, the work in [1] show that the range and angle error are uncorrelated, which means that equation (5) is a good approximation. Note however from Figure 5 that σ_r is a function of *r*.

In cases where the heading is unknown, equation (6) can be replaced by the marginal distribution

$$f_z(z) = \int f(z \mid \theta) f(\theta) d\theta \tag{7}$$

where it is assumed that θ is uniformly distributed between 0 and 2π.

2.5 Trajectory generator

2.5.1 Background

Applying radar measurements in a tracking system makes it hard to do analytical a priori analysis of the accuracy of the system. This is because of the nonlinearities introduced by the polar measurements. Monte Carlo methods are needed in order compare the performance of different tracking algorithms. The performance of the estimator depends on the kinematics of the targets, it depends on the choice of trajectories and velocities.

One possible approach is described in [11]. The target trajectories are simulated with decoupled motion in x and y. The movement in each dimension is generated by a Singer model or by modeling the acceleration as integrated white noise. The performance of the tested algorithms tends to vary as a function of the covariance of the generated random acceleration. In addition this method generates velocities and movements that are unrealistic, especially in naval applications where the velocities are relatively small and coupled in x-and y.

A second approach is described and applied by for instance [11, 2]. One or more of deterministic maneuvers consisting of periods of constant velocity, constant acceleration, and turns is predefined. A different set of measurements and process noise is then generated for each Monte Carlo run. However the results obtained when using this approach tend to vary with the choice of predefined maneuvers.

The trajectory generator presented in this paper is based on the second approach. The trajectories are constructed from segments which are based on realistic maneuver models. The movement of many civilian vehicles can crudely be divided into two phases; straightforward motion with constant thrust, and movement with constant velocity and constant rudder. Independent of the dynamics of the targets, it seems reasonable to divide the motion with constant thrust into two phases, constant acceleration in the time after a new level of thrust has been set, and a phase of stable constant velocity. Movement with constant rudder can be represented by the constant turn rate model.

The main structure is shown in Figure 6. The idea is to model the movement of a simulated target as a JM system, a system that jumps between the different maneuver modes in a random manner. The transition probabilities can be extracted from empirical data in order to generate paths that are close to reality. Using this methodology, an unlimited number of different paths can be generated with dynamics that are close to what is seen in the considered application. The generated trajectories can be used to evaluate all aspects and phases of a tracking system. In this study it is applied to evaluate gain of applying the new measurement models introduced in [1].

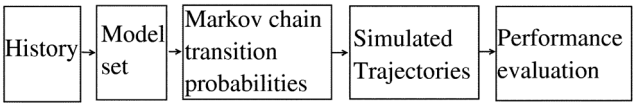

Figure 6 Main structure of trajectory generator

2.5.2 Jump Markov systems

A general JM system can be described as a dynamic system that can be formulated in state space form, where the system dynamics change over time and these changes form a Markov chain.

A jump Markov nonlinear system (JMNLS) can be defined by

$$x_{k+1} = f(t_k, x_k, m_k, w_k) \tag{8}$$

$$P(m_{k+1} = i \mid m_k = j) = \left[M(t_k) \right]_{ij} \tag{9}$$

$$z_k = h(t_k, x_k, m_k, v_k) \tag{10}$$

where m_k is a finite state Markov chain, x_k is the state vector at time t_k, w_k is process noise, and v_k is measurement noise.

2.5.3 System models

The system state at time t_k was modeled by the vector

$$x_k = \begin{bmatrix} p_k^x & h_k^x & n_k^x & p_k^y & h_k^y & n_k^y & \theta_k \end{bmatrix}^T \tag{11}$$

where θ_k was the heading of the target. The velocity of the system at a time was given by

$$v_k = \begin{bmatrix} \dot{p}_k^x & \dot{p}_k^y \end{bmatrix}^T = \begin{bmatrix} h_k^x + n_k^x & h_k^y + n_k^y \end{bmatrix}^T \tag{12}$$

n_k^x and n_k^y were modeled as a piecewise constant Markov processes with exponential autocorrelations, such that the velocites in x and y direction were perturbations about a mean velocity vector $h = \begin{bmatrix} h^x, h^y \end{bmatrix}^T$

The system dynamics had three different modes, constant acceleration (CA), constant turn rate (CT) and constant velocity (CV).

The dynamics of the system in the CA mode were given by the following equations

$$x_{k+1} = \Phi(m_k) x_k + \Lambda(m_k, x_k) u_k + w_k \tag{13}$$

$$\Phi(m_k) = \begin{bmatrix} 1 & T & T & 0 & 0 & 0 & 0 \\ 0 & 1 & 0 & 0 & 0 & 0 & 0 \\ 0 & 0 & -\beta & 0 & 0 & 0 & 0 \\ 0 & 0 & 0 & 1 & T & T & 0 \\ 0 & 0 & 0 & 0 & 1 & 0 & 0 \\ 0 & 0 & 0 & 0 & 0 & -\beta & 0 \\ 0 & 0 & 0 & 0 & 0 & 0 & 1 \end{bmatrix} \tag{14}$$

$$\Lambda(m_k, x_k) u_k = a_k T \begin{bmatrix} 0 & \cos\theta_k & 0 & 0 & \sin\theta_k & 0 & 0 \end{bmatrix}^T \tag{15}$$

$$w_k = \begin{bmatrix} 0 & 0 & w_k^x & 0 & 0 & w_k^y & 0 \end{bmatrix}^T \tag{16}$$

The acceleration vector was chosen such that it was aligned with the heading of the target, θ_k. When the system was in the CV mode, the system equation was equation (13) where $a_k = 0$ in equation (15).

The CT mode system model was given by

$$x_{k+1} = \Phi(m_k)x_k + \Lambda(m_k, u_k) + w_k \quad (17)$$

where

$$\Phi = \begin{bmatrix} 1 & \frac{\sin(\omega T)}{\omega} & T & 0 & -\frac{1-\cos(\omega T)}{\omega} & 0 & 0 \\ 0 & \cos(\omega T) & 0 & 0 & -\sin(\omega T) & 0 & 0 \\ 0 & 0 & -\beta & 0 & 0 & 0 & 0 \\ 0 & \frac{1-\cos(\omega T)}{\omega} & 0 & 1 & \frac{\sin(\omega T)}{\omega} & T & 0 \\ 0 & \sin(\omega T) & 0 & 0 & \cos(\omega T) & 0 & 0 \\ 0 & 0 & 0 & 0 & 0 & -\beta & 0 \\ 0 & 0 & 0 & 0 & 0 & 0 & 1 \end{bmatrix} \quad (18)$$

$$\Lambda(m_k, u_k) = \begin{bmatrix} 0 & 0 & 0 & 0 & 0 & 0 & \omega T \end{bmatrix}^T \quad (19)$$

This system model means that the heading of the target to always be aligned with the mean velocity vector *h*., except when *h*=0. In some applications this may not be the case, but this can be compensated for if the relationship between the two vectors can be modeled deterministically.

2.5.4 Mode selection and transition probabilities

The chosen state space consisted of the following set

$$m_k \in S = \begin{Bmatrix} -\omega_N, -\omega_{N-1}, \ldots, -\omega_1, \omega_1, \omega_2, \ldots, \omega_N, \\ -a_M, -a_{M-1}, \ldots, -a_1, a_1, a_2, \ldots, a_M, CV \end{Bmatrix} \quad (20)$$

The magnitudes of the maximum maneuvers a_M and ω_N are determined by the dynamics of the application, while the values of *N* and *M* can be chosen based on the amount of available empirical data.

The process of choosing the model set *S* and extracting the transition matrix *M* based on empirical data is left for the future. An important element in this process will be to determine *M* such that the mean sojourn time in each mode corresponds to the average time the real system stays in each maneuver mode.

The maximum and minimum velocities were restricted by modifying the transition matrix $M(t_k)$ such that

$$P\left(m_{k+1} \in \{-a_1, -a_2, \ldots, -a_M\} \mid v_k > v_{\max}\right) = 1 \quad (21)$$

$$P\left(m_{k+1} \in \{a_1, a_2, \ldots, a_M\} \mid v_k < v_{\min}\right) = 1 \quad (22)$$

2.5.5 Example

The results in Figure 7 and Figure 8 were generated using the model set $S = \{\omega_s, a_s, CV\}$, where

$$a_s = \{-0.3, -0.22, -0.13, -0.05, 0.05, 0.13, 0.22, 0.3\} \frac{m}{s^2} \quad (23)$$

$$\omega_s = \{-8, -6.66, -5.33, -4, 4, 5.33, 6.66, 8\} 10^{-2} \frac{rad}{s} \quad (24)$$

The mean sojourn times were chosen such that the average distance traveled in the constant velocity state was 200 m, and the mean velocity increase in the $a_{\max}$ state were chosen to be 4 m/s, and $|\Delta v_i| = 4|a_i / a_{\max}|$ (m/s) in the other states. The mean turn were chosen to be $|\Delta\theta_i| = (3/8)\pi|\omega_i / \omega_{\max}|$. The velocity of the target was restricted by $v_{\min} = 3$ m/s and $v_{\max} = 15$ m/s.

The trajectory generator could then be used to generate a large number of realistic trajectories within a restricted area as seen in Figure 7. An example of a long path which could be a useful tool for filter tuning in cases with spatially constant measurement noise is shown in Figure 8.

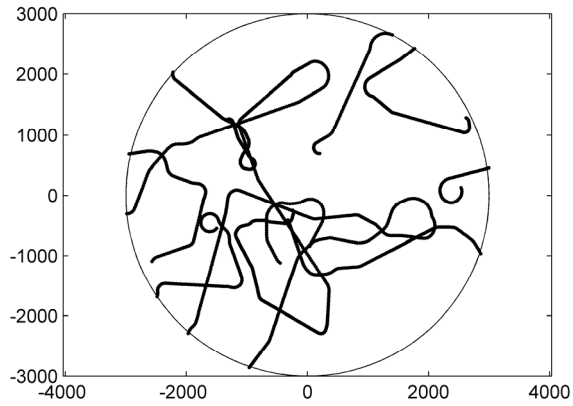

Figure 7 Ten generated paths restricted to the range $r \in [10, 3000]$ m.

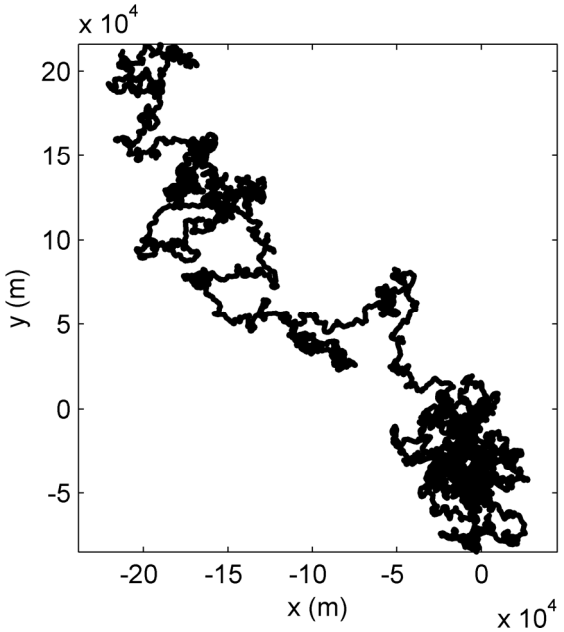

Figure 8 One long generated trajectory using the same system model as in Figure 7.

2.6 Estimators

The tracking filters applied in this study were IMM estimators based on different kinematic models. The estimators included different combinations of the Continuous White Noise Acceleration system model (CWNA) [2] and Coordinated Turn (CT) models.

The CWNA models were configured with low process noise to model movement with constant velocity (CV) and with high process noise to model constant acceleration (CA). A third order IMM estimator was tested consisting of a CV model, a CA model and a CT model (IMM-CV-CA-CT). Some second order filters were also tested; IMM-CA-CV and IMM-CA-CT. A first order Kalman filter (KF) was included for comparison.

2.6.1 Measurement models

Since the exact heading is not available in reality, equation (6) had to be approximated using the estimated or measured target heading. When a measurement of the target heading $\hat{\theta}_k$ is available, equation (6) can be approximated by

$$\hat{R} = \hat{\Theta} R_0 \hat{\Theta}^T = \begin{bmatrix} \cos\hat{\theta}_k & -\sin\hat{\theta}_k \\ \sin\hat{\theta}_k & \cos\hat{\theta}_k \end{bmatrix} \begin{bmatrix} \sigma_a^2 & 0 \\ 0 & \sigma_t^2 \end{bmatrix} \begin{bmatrix} \cos\hat{\theta}_k & \sin\hat{\theta}_k \\ -\sin\hat{\theta}_k & \cos\hat{\theta}_k \end{bmatrix} \quad (25)$$

In other cases equation (6) can be approximated using the predicted target heading, $\bar{\theta}_k$. The direction of the predicted velocity vector may also be used if it is approximately parallel to the heading of the target

$$\bar{\theta}_k = \arctan\left(\frac{\bar{v}_y}{\bar{v}_x}\right) \quad (26)$$

The second measurement model applied in filters in this paper was based on a first order of Taylor expansion of equation (5), such that

$$\hat{R}^u = \Phi R_1 \Phi^T = \begin{bmatrix} \cos\phi & -\sin\phi \\ \sin\phi & \cos\phi \end{bmatrix} \begin{bmatrix} \sigma_r^2 & 0 \\ 0 & \left(\sigma_\phi^*\right)^2 \end{bmatrix} \begin{bmatrix} \cos\phi & \sin\phi \\ -\sin\phi & \cos\phi \end{bmatrix} \quad (27)$$

ϕ in the equation above is the position of the target in polar coordinates which had to be approximated by a predicted or measured value.

3 Simulations and results

In all simulations the Root Mean Square Error in position and velocity were used as measures of the performance of the estimators. The measures are defined by

$$RMSE(p) = \sqrt{\frac{1}{N}\sum_{k=1}^{O}\left(\left(\hat{p}_k^x - p_k^x\right)^2 + \left(\hat{p}_k^y - p_k^y\right)^2\right)} \quad (28)$$

$$RMSE(v) = \sqrt{\frac{1}{N}\sum_{k=1}^{O}\left(\left(\hat{v}_k^x - v_k^x\right)^2 + \left(\hat{v}_k^y - v_k^y\right)^2\right)} \quad (29)$$

where the index k runs over all trajectories in all Monte Carlo runs.

All results in this section were obtained using the system parameters described in section 2.5.5.

3.1 Spatially constant measurement errors

Some simulations were done with spatially constant measurement errors, which meant that σ_a and σ_t in equation (6) were independent of r. The performance of the estimators for a given target dynamic could thus be evaluated using one long representative trajectory as seen in Figure 8. In this manner the effect of filter initialization was minimized, and the performance measures converged to a scalar as the size of the trajectory increased.

In order to evaluate the gain of using equation (6), the performance was compared to that of an estimator which erroneously assumed that there was no correlation between heading and measurement errors. The measurement error equation was thus given by equation (27) with $\sigma_r = \sigma_\phi^* = \sigma_v$ In order to do a fair comparison, σ_v was chosen such that $\sigma_v = \sqrt{\sigma_a \sigma_t}$. The estimators were either based on a measured target heading or the predicted target heading, as described in the two following subsections.

3.1.1 Measured heading

In these simulations it was assumed that the heading of the target was measured and that the measured heading error was normally distributed

$$z_\theta \sim N\left(\theta, \sigma_\theta^2\right) \quad (30)$$

The results seen in Figure 9 and Figure 10 compare the RMSE(p) and RMSE(v) of the filters assuming correlated measurement error to the uncorrelated filter.

The IMM-CV-CA-CT filter was used for both models. The system parameters of the measurement equations were such that $\sigma_v^2 = \sigma_a \sigma_t = 25$ and $\sigma_a = 3\sigma_t$. The update time was T=3 s.

3.1.2 Heading approximated by predicted velocity vector

The results in Table 1 and Table 2 compare the performance of filters assuming correlation ($R = \hat{R}^c$) and the uncorrelated filter ($R = R^u$). The heading of the target was approximated by the predicted velocity vector at each time step. The system parameters were T=3 s and measurement noise of $\sigma_a \sigma_t = \sigma_v^2 = 9$. The first column ($C_z$) indicates whether the estimator assumes correlation between heading and measurement noise ($\hat{R}^c$) or uncorrelated (R^u).

The factor $\rho = \sigma_a / \sigma_t$ was used as a measure of the correlation between the target heading and measurement uncertainty.

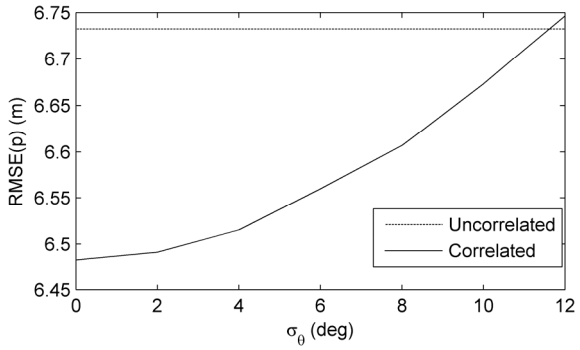

Figure 9 RMSE(p) as a function of standard deviation of measured heading.

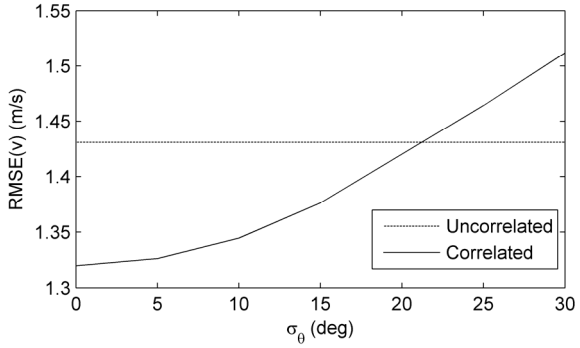

Figure 10 RMSE(v) as a function of error in measured heading.

3.2 Measurement noise as a function of *r*

In the following simulations it was assumed that σ_a and σ_t were a function of the distance from the radar. The radar was located at origo.

All the measurements were generated using equation (6) and Figure 4, while the uncorrelated filter assumed the models in equation (27) and Figure 5 were true. The RMSE(p) and RMSE(v) as a function of *r* were calculated using a histograms and are shown in Figure 11 and Figure 12.

The algorithms were tested within the sector $200\,\mathrm{m} < r < 5000\,\mathrm{m}$. A large number of paths were generated within this area using the trajectory generator as seen in Figure 7. The trajectories were generated uniformly over the area and terminated when out of bounds.

Each tracker was initialized with a Gaussian perturbation of the true state.

4 Discussion

The results in section 3 show that inclusion of the measurement model in equation (6) can increase the accuracy of a tracking filter. The results are based on the work in [1], and are limited to systems that apply centroid

Table 1 RMSE(p) (m) estimated using one long trajectory for different tracking algorithms

C_z	ρ	IMM-CV-CV	IMM-CV-CT	IMM-CA-CV-CT	KF
$\hat{R}^c$	2	3.83	3.76	3.72	3.90
R^u	2	4.09	3.88	3.78	4.15
$\hat{R}^c$	3	4.25	4.18	4.16	4.31
R^u	3	4.65	4.44	4.33	4.71
$\hat{R}^c$	5	5.13	5.05	5.06	5.19
R^u	5	5.70	5.50	5.39	5.76
$\hat{R}^c$	10	7.23	7.11	7.18	7.25
R^u	10	7.77	7.56	7.48	7.86

Table 2 RMSE(v) (m/s^2) estimated using one long trajectory for different tracking algorithms.

C_z	ρ	IMM-CV-CV	IMM-CV-CT	IMM-CA-CV-CT	KF-
$\hat{R}^c$	2	1.30	1.09	1.05	1.31
R^u	2	1.44	1.17	1.09	1.45
$\hat{R}^c$	3	1.26	1.08	1.06	1.27
R^u	3	1.50	1.24	1.14	1.52
$\hat{R}^c$	5	1.26	1.12	1.11	1.27
R^u	5	1.64	1.40	1.30	1.68
$\hat{R}^c$	10	1.38	1.28	1.30	1.39
R^u	10	1.99	1.76	1.67	2.06

signal processing on 2D radar images. A radar tracking system that is able to resolve individual scattering objects on an extended target will most likely apply other signal processing methods. .

The JM trajectory generator described in section 2.5 proved to be a useful tool for evaluating estimator performance. The generator generated random path with dynamics that were similar to trajectories seen in the considered application.

The JM trajectory generator could also for instance be used to examine estimator performance as a function of target maneuverability. The maneuverability of the target is easily adjusted by changing the transition matrix *M*.

The model and parameter selection in the JM system can be extracted using empirical data, or by choosing models and transition probabilities based on the subjective belief of the designer. However, the method limits the results to one kind of target dynamics, the estimator may perform different for a different class of targets. On the other hand, the trajectory generator can easily be modified to generate paths with different system dynamics.

The process noise added to the trajectories were defined as independent in x and y direction. In future

work, the process noise will be defined in the target frame and other noise models will be examined.

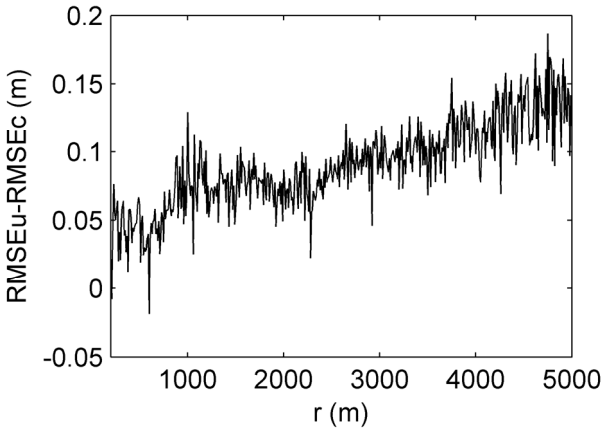

Figure 11 RMSE(p) as function of range, difference between filter that assumes correlation between heading and measurement covariance (RMSEc) and filter that assumes uncorrelated (RMSEu).

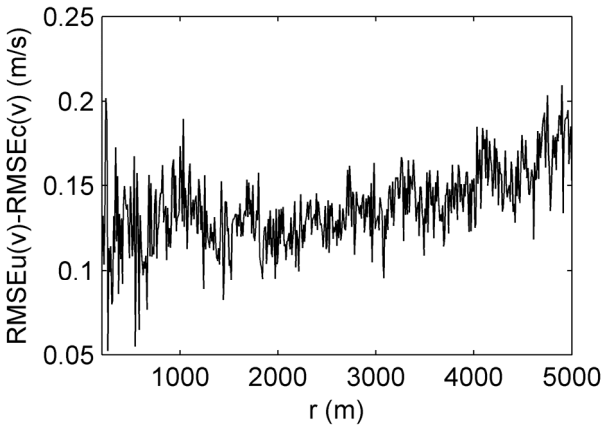

Figure 12 RMSE(v) as function of range, difference between filter that assumes correlation between heading and measurement covariance (RMSEc) and the uncorrelated estimator (RMSEu).

5 Conclusion

The work in [1] shows how there may be correlation between target heading measurement uncertainty when centroid image processing is applied to radar images of extended targets. This paper shows how a model of this correlation can be used to increase the accuracy of target tracking algorithms. The gain in accuracy is verified by simulations.

A trajectory generator based on jump Markov nonlinear systems was introduced and applied to evaluate the performance of the estimators introduced in this paper. This trajectory generator jumps in a random manner between periods of movement with constant velocity, constant acceleration, and constant turn rate. The generated trajectories resemble real target trajectories in many applications. The trajectory generator is a flexible tool and can be used to evaluate the performance of many aspects of a target tracking system.

Acknowledgments

Rune O. Stemland from Norcontrol IT is thanked for providing technical assistance and insight. All faculty and students at the ISL laboratory at the University of New Orleans are also thanked.

References

[1] M. Stakkeland, Ø. Overrein, and O. Hallingstad, "The error statistics of surveillance radar position measurements," to be presented at IET Radar 2007, The International Conference on Radar Systems, Edinburgh, UK, 2007

[2] Y. Bar-Shalom, X. R. Li, and T. Kirubarajan, *Estimation with applications to tracking and navigation*. New York: Wiley, 2001.

[3] J. Dezert, "Tracking maneuvering and bending extended target in cluttered environment," presented at Proceedings of SPIE - The International Society for Optical Engineering, 1998.

[4] B. J. Slocumb, "Surveillance radar range-bearing centroid processing," *Proceedings of SPIE - The International Society for Optical Engineering*, vol. 4473, pp. 74--85, 2001.

[5] D. K. Barton, *Modern radar system analysis*: Artech House, 1988.

[6] E. Oron, A. Kumar, and Y. Bar-Shalom, "Precision tracking with segmentation for imaging sensors," *IEEE Transactions on Aerospace and Electronic Systems*, vol. 29, pp. 977--986, 1993.

[7] A. Papoulis, *Probability, random variables, and stochastic processes*, 3 ed. New York: McGraw-Hill, 1991.

[8] X. R. Li and V. P. Jilkov, "A survey of maneuvering target tracking - Part III: Measurement models," *Proceedings of SPIE - The International Society for Optical Engineering*, vol. 4473, pp. 423-446, 2001.

[9] W. D. Blair and B. M. Keel, "Radar Systems Modeling for Tracking," in *Multitarget-Multisensor Tracking: Applications and Advances Volume III*, Y. Bar-Shalom and W. D. Blair, Eds. Norwood, Ma: Artech House, 2000, pp. 321-393.

[10] J. B. Romine and E. W. Kamen, "Modeling and fusion of radar and imaging sensor data for target tracking," *Optical Engineering*, vol. 35, pp. 659 - 73, 1996.

[11] S. S. Blackman and R. Popoli, *Design and analysis of modern tracking systems*. Boston, MA: Artech House, 1999.

7

Paper three

Is not included due to copyright

8

Paper four

Tracking of targets with state dependent measurement errors using recursive BLUE filters

Morten Stakkeland
University Graduate Center
Kjeller, Norway
mst@unik.no

Øyvind Overrein
Applied Radar Physics ASA
Kjeller, Norway
overrein@arp.no

Edmund F. Brekke
University Graduate Center
Kjeller, Norway
edmund@unik.no

Oddvar Hallingstad
University Graduate Center
Kjeller, Norway
oh@unik.no

Abstract − *In this paper, optimal best linear unbiased estimation (BLUE) filters are derived for cases where measurement errors depend on the state of the target. The standard Kalman filter fails to provide optimal estimates in these cases. Previously applied measurement models are reformulated in order to apply BLUE filters, and two new measurement models with state dependent biases are proposed. It is shown how the higher order unscented transform may be used to approximate the terms in the BLUE filter when they are not available analytically. The BLUE filters are shown by Monte Carlo simulations to have better performance than other suboptimal filters.*

Keywords: Target tracking, extended targets, measurement models, BLUE filters, jump Markov models

1 Introduction

Position measurements that are converted from range and azimuth in polar coordinates to x and y in Cartesian coordinates is an example of measurement errors that are dependent on the state of the targets. This problem is well studied in the literature, an overview can be found in [1]. One approach is to estimate the mean measurement and measurement covariance conditioned on either the measurements or the predicted state. The approximated measurement mean and covariance are then used in a standard Kalman filter. However, in [2] it was shown how this approach violates several of the fundamental assumptions of the Kalman filter, which for instance assumes that the measurement noise covariance is unconditional. They proposed to apply recursive best linear unbiased estimator (BLUE) filters to resolve these fundamental problems.

The work in [3] proposed two new measurement models where radar position measurement errors depended on the aspect angle as well as the position of the target. One of these models were implemented in a tracking framework in [4], where the measurement covariance was approximated by the conditional covariance. This paper extends the work in [4] by implementing recursive BLUE filters. The measurement models proposed in [3] are reformulated in order to express the measurement noise as unconditional. Two additional measurement models with biases that depend on the state of the target are proposed, and some additional results extending the work in [3] is included. It is shown how the recursive BLUE filters have better performance than suboptimal filters, using the Root Mean Square Error (RMSE) of the tracking filters as performance measure. Unscented transforms (UT) and higher order unscented transforms (HOUT) are used to approximate the terms of the BLUE filters in cases where they are not available as closed form expressions. It is shown how an UT using the symmetric set [5] provides insufficient accuracy when the approximated nonlinear function involves rotation. A HOUT may be used for this case. The methodology is also applied on the system model introduced in [6], where the process noise is state dependent.

This paper starts with a description of the different measurement models in section 2, where several measurement models that include state dependent measurement errors are formulated. Section 3 then derives BLUE filters for each of the measurement models, and describes how UT can be used to approximate the terms of BLUE filter that do not have a closed form expression. A description of the applied estimation filters and simulation tools as well as some simulation results is presented in section 4. The conclusion can be found in section 5.

2 Measurement models

2.1 State dependent measurement noise

The work described in [3] examined the correlation between the aspect angle of a target and measurement

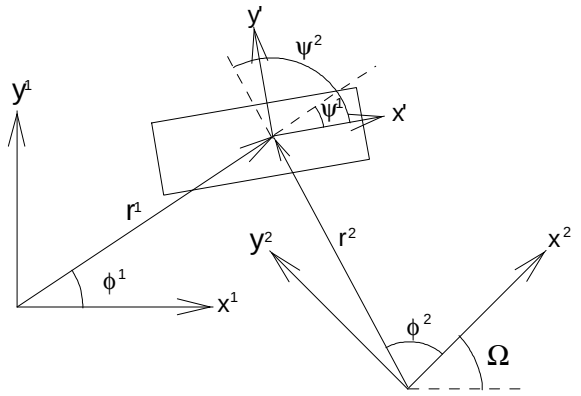

Figure 1: Multi sensor 2D target sensor geometry. $[r^{1,2}, \phi^{1,2}]$ = position of the target expressed in the reference frames of sensor 1 and 2. $\psi^{1,2}$= aspect angles. Ω=rotation of the reference frame of sensor 2 with respect to sensor 1.

error for radar measurements of extended targets. The investigations were performed in a Monte Carlo simulation framework. Simplified physical target and system models were used to simulate radar images, using the simplest component quasi optical method described in [7]. Three measurement models were presented.

The first model was the standard model which can be derived by a Taylor expansion of uncorrelated range and azimuth measurements [1]. The model is in this paper named C as the noise covariance depends on the position of the target in Cartesian space. By introducing the variance $\sigma^2_{\phi*} = (r\sigma_\phi)^2$, the measurement noise covariance given the bearing angle ϕ_k can be written as

$$\mathrm{cov}\left(w_k|\phi_k\right) = E\left(w_k w_k^T|\phi_k\right) = \Phi\left(x_k\right) R_k^C \Phi^T\left(x_k\right) \quad (1)$$

$$\Phi\left(x_k\right) = \begin{bmatrix} \cos\left(\phi_k\right) & -\sin\left(\phi_k\right) \\ \sin\left(\phi_k\right) & \cos\left(\phi_k\right) \end{bmatrix} \quad (2)$$

$$R_k^C = E\left(w_k w_k^T\right) = \begin{bmatrix} \sigma_r^2 & 0 \\ 0 & \sigma_{\phi*}^2 \end{bmatrix} \quad (3)$$

The angular variance $\sigma^2_{\phi*}$ here has units m^2. This measurement model is frequently formulated as linear with additive noise, $z_k = Hx_k + w_k$, where the noise covariance matrix is approximated by the conditional matrix $R_k = E\left(w_k w_k^T\right) \approx E\left(w_k w_k^T|\phi_k\right)$. Given a state vector defined by $x_k = \begin{bmatrix} p_k^x & v_k^x & p_k^y & v_k^y \end{bmatrix}^T$, then it is in this paper proposed to formulate the measurement model as nonlinear in order to avoid the conditional covariance.

$$z_k = h\left(x_k, w_k\right) = Hx_k + \Phi\left(x_k\right) w_k \quad (4)$$

In this expression, $E\left(x_k w_k^T\right) = 0$, $E\left(w_k\right) = 0$, and H is given by

$$H = \begin{bmatrix} 1 & 0 & 0 & 0 \\ 0 & 0 & 1 & 0 \end{bmatrix} \quad (5)$$

$\Phi\left(x_k\right)$ is then a random matrix with non Gaussian entries.

The second proposed model, here named model O as the covariance depends on the state of the object, assumed that the measurement errors were perfectly correlated with the aspect angle of the target. Using that the aspect angle shown as ψ in figure 1 is given as the difference between the heading and bearing $\psi = \theta - \phi$, the measurement noise covariance conditioned on the heading θ_k can be written as

$$\mathrm{cov}\left(w_k|\theta_k\right) = E\left(w_k w_k^T|\theta_k\right) = \Theta_k\left(x_k\right) R_k^O \Theta^T\left(x_k\right) \quad (6)$$

$$\Theta\left(x_k\right) = \begin{bmatrix} \cos\left(\theta_k\right) & -\sin\left(\theta_k\right) \\ \sin\left(\theta_k\right) & \cos\left(\theta_k\right) \end{bmatrix} \quad (7)$$

$$R_k^O = E\left(w_k w_k^T\right) = \begin{bmatrix} \sigma_a^2 & 0 \\ 0 & \sigma_t^2 \end{bmatrix} \quad (8)$$

σ_a^2 and σ_t^2 are the measurement noise variances along and in transverse direction of the main axis of the target respectively. This model is also reformulated in this paper by introducing the random matrix $\Theta\left(x_k\right)$.

$$z_k = h\left(x_k, w_k\right) = Hx_k + \Theta\left(x_k\right) w_k \quad (9)$$

The simulation results presented in [4] indicated that the first model is a better fit at long range where the target approaches a point target, while the second model is a better fit at short ranges where the target is extended. The two models were extended by a third model [3], 3P, which can be viewed as a compromise between the two previous models. This model preserves both the correlation with the object heading as well as the bearing. The covariance of the noise of this model conditioned on heading and bearing angle is given by

$$\begin{aligned} R_k^{3P} &= \mathrm{cov}\left(w_k|\theta_k, \phi_k\right) = E\left(w_k w_k^T|\theta_k, \phi_k\right) \\ &= \Theta\left(x_k\right) R_k^O \Theta^T\left(x_k\right) + \Phi\left(x_k\right) R_k^C \Phi^T\left(x_k\right) \end{aligned} \quad (10)$$

The random matrices $\Theta\left(x_k\right)$ and $\Phi\left(x_k\right)$ are defined in equation (7) and (2) respectively, and R_k^C and R_k^O are defined in equations (3) and (8). Extending the work in [3], this can also be formulated as a nonlinear measurement equation.

$$z_k = Hx_k + \Theta\left(x_k\right) w_k^O + \Phi\left(x_k\right) \begin{bmatrix} 0 \\ 1 \end{bmatrix} w_k^C \quad (11)$$

$$E\left(w_k^C \left(w_k^C\right)^T\right) = \sigma_{\phi*}^2,\ E\left(w_k^O \left(w_k^O\right)^T\right) = R_k^O \quad (12)$$

$$E\left(x_k \left(w_k^O\right)^T\right) = 0,\ E\left(x_k \left(w_k^C\right)^T\right) = 0 \quad (13)$$

The added measurement noise conditioned on ϕ_k and θ_k is the sum of two Gaussian random variables and hence Gaussian. However the products $\Theta\left(x_k\right) w_k^O$ and $\Phi\left(x_k\right) \begin{bmatrix} 0 & 1 \end{bmatrix}^T w_k^C$ are not necessarily Gaussian.

Note that the 3P model could be reformulated as a C model plus a component that is correlated with aspect

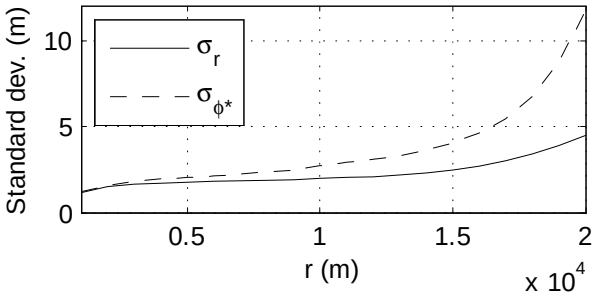

Figure 2: Parameter estimates for model C as function of range. SNR of of target function of range.

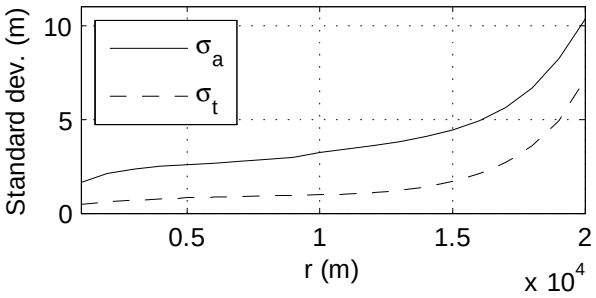

Figure 3: Parameter estimates for model O as function of range.

angle. The conditional covariance can then be written as

$$R_k = \Phi(x_k) R_k^C \Phi^T(x_k) + \Theta(x_k) R_k^A \Theta^T(x_k)$$

R_k^C is given by equation (3) and $R_k^A = diag(\sigma_a^2, 0)$.

The results plotted in figures 2, 3, and 4, show parameters estimates for each of the three models based on a generated data set. The figures further extend the results presented in [3] by modeling the SNR of the target as a function of range. The position of the target was known, and the parameters of the Gaussian distribution were estimated using maximum likelihood methods. A rectangular target consisting of 1000 objects distributed over a 40 m ×10 m was used.

Figure 3 and 4 show how the 3P model and the O model are equivalent up to $r = 10$ km, where the angular component of the 3P model starts to increase. The symmetrized Kullback Leibler Divergence (KLD) between the data set and each of the models under a Gaussian assumption is plotted in figure 5. The symmetrized KLD for two Gaussian distributions is given

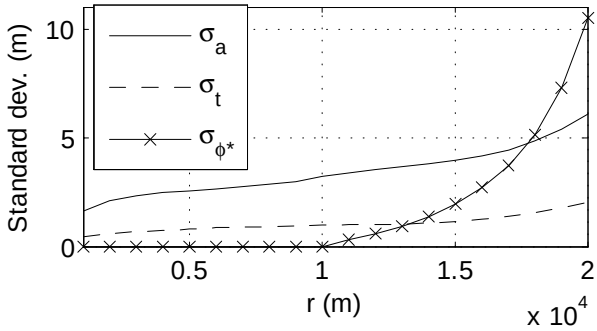

Figure 4: Parameter estimates of model 3P as function of range

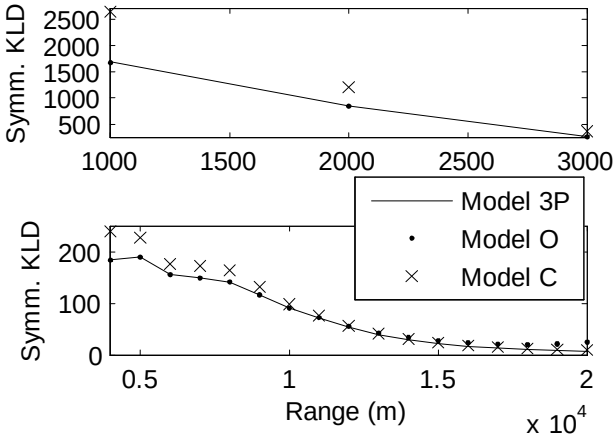

Figure 5: Estimated KLD between generated data set and parameterized Gaussian error models as function of range. SNR of target function of range.

by [8]

$$\begin{aligned} &D(\mathcal{N}_1(\mu_1, P_1), \mathcal{N}_2(\mu_1, P_2)) \\ &= \frac{1}{2} trace\left(P_1^{-1} P_2 + P_2^{-1} P_1\right) - \dim(x) \\ &+ \frac{1}{2}(\mu_2 - \mu_1)^T \left(P_1^{-1} + P_2^{-1}\right)(\mu_2 - \mu_1) \end{aligned} \quad (14)$$

Figure 5 shows that the 3P model has the smallest KLD for all ranges. The KLDs of the 3P and O models are equal and smaller than the C model until $r \approx 13$ km, after which the C model has a smaller KLD than the O model. Figures 2, 3, and 4 show how the parameters in each model vary as a function of range. Extensive simulations indicate that the parameter values are a complex function of target size, target shape, SNR, spatial resolution defined by lobe width and pulse length, and sampling density defined by sampling rates in range and bearing. For a circular or square target, σ_a is equal to σ_t for all ranges. The angular component of the 3P model is shown to increase firstly when the target be-

comes smaller than the lobe width and secondly when the target becomes smaller than the angular resolution. An extended target may be defined by the target size relative to one of these two parameters.

At close range, the dominating noise component in the target images was speckle noise. Speckle noise is caused by interference between the signals from individual scattering objects. The generated measurements for a given aspect angle or over a small range of aspect angles were then far from Gaussian, and the marginalized noise over all aspect angles was in some cases also far from Gaussian. This may explain the trend seen in the KLDs shown in figure 5, where the KLD for each model declines with range. Noise effects not modeled in the idealized simulations may add more normality to the measurement noise, but on the other hand multipath and reverberation effects which were not included in the simulation may also add non Gaussian components.

2.2 Biased measurements

In some cases there may be a bias in the measurements that is a function of the velocity vector of the target. An example is tracking applications where clutter generated behind a target may be included as a part of the target image and thus cause a bias. The clutter may be for instance induced by a wake generated by a ship or plane, or in a bubble stream generated by a diver [9]. Measurement errors caused by sensor biases, such as range, bearing, and elevation biases, are also dependent on the state of the target. However, the error obtained by ignoring the state dependency of sensor biases can in many cases be ignored as the range usually is much larger than the magnitude of the biases.

Assume that a measurement bias can be approximated as a linear function of the velocity vector, as $b_k^1 = \alpha \cdot v_k = \alpha \cdot \left[\begin{array}{cc} v_k^x & v_k^x \end{array} \right]^T$ where α is a known constant. This bias may be handled by a standard Kalman filter with measurement equation given by

$$\begin{aligned} z_k &= Lx_k + w_k \\ L &= \left[\begin{array}{cccc} 1 & \alpha & 0 & 0 \\ 0 & 0 & 1 & \alpha \end{array} \right] \end{aligned} \tag{15}$$

A similar type of bias may also be defined, where the bias is a constant vector parallel to the velocity vector.

$$\begin{aligned} b_k^2 &= \alpha \cdot v_k / |v_k| = \alpha \cdot \frac{1}{|v_k|} \left[\begin{array}{cc} v_k^x & v_k^x \end{array} \right]^T \\ &= \alpha \cdot \left[\begin{array}{cc} \cos\theta_k & \sin\theta_k \end{array} \right]^T \end{aligned} \tag{16}$$

A bias in range, dependent on the aspect angle of the target is also proposed. This bias can be caused by reflective objects on the target being occluded by other objects, which may for instance be the case for radar position measurements of a ship. These kind of biases may for some sensor target geometries be larger when moving in a radial direction than in a transverse direction. This bias can be formulated as

$$\begin{aligned} b_k^3 &= \alpha \cdot |\cos(\psi_k)| \cdot r_k / |r_k| \\ &= \alpha \cdot |\cos(\theta_k - \phi_k)| \cdot \left[\begin{array}{cc} \cos\phi_k & \sin\phi_k \end{array} \right]^T \end{aligned} \tag{17}$$

2.3 Marginalized noise models

If the correlation between the aspect angle ψ and the measurement noise is unknown or unmodeled, the measurement likelihood function may be expressed as the marginal probability density function (pdf), $f(z|x) = \int f(z|\psi, x) f(\psi) d\psi$. It is in many cases reasonable to assume that the aspect angle is uniformly distributed over the interval $[0, 2\pi]$. The C model may thus be considered as the 3P model marginalized over all aspect angles. In a similar manner, the O model may obtained by marginalizing the azimuth angle ϕ of a 3P model over $[0, 2\pi]$.

The conditional 3P likelihood function is Gaussian, with measurement covariance R_k^{3P} defined in equation (10). The 3P model marginalized over all aspect angles can be shown by numerical integration to be zero mean, and to have a conditional covariance given by $\Phi_k(x_k) R_k^{mC} \Phi^T(x_k)$, where

$$R^{mC} = \left[\begin{array}{cc} \frac{1}{2}\left(\sigma_a^2 + \sigma_t^2\right) & 0 \\ 0 & \frac{1}{2}\left(\sigma_a^2 + \sigma_t^2\right) + \sigma_{\phi*}^2 \end{array} \right] \tag{18}$$

This likelihood function can thus be written as a C model with covariance given by equation (18). In the same manner, an O model can be obtained by marginalizing the 3P model over all bearing angles. The conditional covariance of this marginalized O model is given by $\Theta_k(x_k) R_k^{mO} \Theta^T(x_k)$, where

$$R^{mO} = \left[\begin{array}{cc} \sigma_a^2 + \frac{1}{2}\sigma_{\phi*}^2 & 0 \\ 0 & \sigma_t^2 + \frac{1}{2}\sigma_{\phi*}^2 \end{array} \right] \tag{19}$$

The dependency on either aspect or bearing angle is ignored when using a marginalized filter, which would make the filter suboptimal. However, the marginal covariance may be the best option for cases where the dependency on the state vector is unknown or unmodeled.

2.4 Correlated measurements

The correlation between two sequential measurements $R_{k,k+1} = E\left(w_k w_{k+1}^T\right)$ is in general assumed to be zero, which is also one of the fundamental assumptions of the standard Kalman filter. However, this may in many cases fail to be true for a radar measurement of an extended real target. Occlusion effects may cause that a given scattering object is visible for some aspect angles, but invisible in other cases. This effect causes measurements to be correlated. The correlation will be highly target dependent, and there may be large variations in the correlation for different aspect angles. This correlation effect will also be state dependent in the sense

that it depends on the ratio of change in aspect angle. Correlated measurements may be compensated for, as for instance outlined in [10], but this requires that the correlation is quantified. In most cases this will be hard to derive.

In [11] this is handled by assuming that there may be an offset between the geometric center of the target and the center of the part of the target that contributes to the radar image. This offset is assumed to be constant for small changes in aspect angle, modeled as a Wiener process and estimated at each scan. However, the simulations used to derive the error models presented in section 2.1 also showed that changes in aspect angle as small as 0.05° may induce significant speckle noise and completely change the target image. The offset may therefore not be observable. The proposed solution is therefore to compensate for correlation by biases as state dependent biases as described in section 2.2, and ignore the correlation from scan to scan.

3 BLUE filters

As discussed in section 1, the Kalman filter assumes that the measurement noise covariance is unconditional. Recursive BLUE filters were thus derived and applied on all the measurement models described in the previous section. Consider a measurement z_k with mean $\bar{z}_k$, and a state vector with prior mean and covariance given by $\bar{x}_k$ and $\bar{P}_k$, The BLUE (or LMMSE) estimator is then given by

$$\begin{aligned}\hat{x}_k &= \bar{x}_k + C_{xz}C_z^{-1}\left(z_k - \bar{z}_k\right)\\ \hat{P}_k &= \bar{P}_k - C_{xz}C_z^{-1}C_{xz}^T\end{aligned}$$

$C_{xz} = E\left(\left(x_k - \bar{x}_k\right)\left(z_k - \bar{z}_k\right)^T\right)$ is the cross covariance and $C_z = E\left(\left(z_k - \bar{z}_k\right)\left(z_k - \bar{z}_k\right)^T\right)$ is the innovation mean square error (MSE) [10]. In the case that C_{xz}, C_z, $\bar{z}_k$, $\bar{P}_k$ $\bar{x}_k$ are exactly available through $\hat{x}_{k-1}$ and $\hat{P}_{k-1}$, then the BLUE filter becomes truly recursive [2]. The BLUE estimation update together with a system model for state prediction thus provide a framework for recursive filtering. These equations become the standard Kalman filter equations for a linear system with white and additive noise.

3.1 BLUE filter for equation (11)

Following [4], it is in this paper assumed that the heading vector is aligned with the velocity vector, or that the misalignment between these vectors is known and can be compensated for. The heading angle in equation (7) is thus given by $\theta_k = \arctan(v_k^y/v_k^x)$, and its covariance depends on the pdf of the velocity vector.

The BLUE filters for the nonlinear measurement equations (4) and (9) are implicitly given by developing an estimator for equation (11). Using that $E\left(x_k\left(w_k^O\right)^T\right) = E\left(x_k\left(w_k^C\right)^T\right) = 0$, the state measurement correlation matrix is given by

$$C_{xz} = E\left(\left(x_k - \bar{x}_k\right)\left(z_k - \bar{z}_k\right)^T\right) = \bar{P}_k H^T$$

and $\bar{z}_k = E\left(z_k\right) = H\bar{x}_k$. In a similar manner, the innovation covariance matrix C_z is given by the following equation, where the index k is left out for simplicity.

$$\begin{aligned}C_z &= H\bar{P}H^T + B + D \qquad (20)\\ B &= E\left(\Gamma\Theta\left(x\right)w^O\left(w^O\right)^T\Theta^T\left(x\right)\Gamma^T\right)\\ D &= E\left(\Gamma\Phi\left(x\right)\begin{bmatrix}0\\1\end{bmatrix}w^C\left(w^C\right)^T\begin{bmatrix}0\\1\end{bmatrix}^T\Theta^T\left(x\right)\Gamma^T\right)\end{aligned}$$

The matrices $\Theta\left(x_k\right)$ and $\Phi\left(x_k\right)$ are here random. In order to derive expressions for B and D, consider the following simple system, where ω is an angular variable.

$$z = h\left(x\right) = \Omega x \qquad (21)$$

$$\Omega = \begin{bmatrix}\cos\omega & -\sin\omega\\ \sin\omega & \cos\omega\end{bmatrix}, x = \begin{bmatrix}a & b\end{bmatrix}^T \qquad (22)$$

$$E\left(\omega\right) = \bar{\omega},\ E\left(x\right) = \begin{bmatrix}0 & 0\end{bmatrix}^T,\ E\left(x\omega\right) = \begin{bmatrix}0 & 0\end{bmatrix}^T \qquad (23)$$

$$Q = E\left(xx^T\right) = \begin{bmatrix}\sigma_a^2 & 0\\ 0 & \sigma_b^2\end{bmatrix},\ E\left(\omega^2\right) = \sigma_\omega^2 \qquad (24)$$

The measurement covariance is here given by $C_z = E\left(\Omega x x^T \Omega^T\right)$. The terms of C_z are derived in the following paragraphs.

$$C_z^{1,1} = E\left(a^2\cos^2\left(\omega\right) + b^2\left(1 - \cos^2\left(\omega\right)\right) - ab\sin\left(2\omega\right)\right) \qquad (25)$$

$$= \sigma_a^2 E\left(\cos^2\left(\omega\right)\right) + \sigma_b^2 E\left(1 - \cos^2\left(\omega\right)\right) \qquad (26)$$

$$= \frac{1}{2}\left(\sigma_a^2 + \sigma_b^2\right) + \frac{1}{2}\left(\sigma_a^2 - \sigma_b^2\right)\cos\left(2\bar{\omega}\right)\exp\left(-2\sigma_\omega^2\right) \qquad (27)$$

The expectation of $\cos^2\left(\omega\right)$ is derived by assuming that ω is Gaussian and expressing $\omega = \bar{\omega} + \tilde{\omega}$. This gives $E\left(\cos^2\left(\omega\right)\right) = \cos\left(2\bar{\omega}\right)\exp\left(-2\sigma_\omega^2\right)$. The same approach gives

$$C_z^{2,2} = \frac{1}{2}\left(\sigma_a^2 + \sigma_b^2\right) + \frac{1}{2}\left(\sigma_a^2 - \sigma_b^2\right)\cos\left(2\bar{\omega}\right)\exp\left(-2\sigma_\omega^2\right) \qquad (28)$$

By deriving $E\left(\sin 2\omega\right)$ in a similar manner, the following equation can be derived.

$$C_z^{1,2} = C_z^{2,1} = E\left(\left(\frac{a^2}{2} - \frac{b^2}{2}\right)\sin\left(2\omega\right) + ab\cos\left(2\omega\right)\right)$$

$$= \frac{1}{2}\left(\sigma_a^2 - \sigma_b^2\right)E\left(\sin\left(2\omega\right)\right) \qquad (29)$$

$$= \frac{1}{2}\left(\sigma_a^2 - \sigma_b^2\right)\sin\left(2\bar{\omega}\right)\exp\left(-2\sigma_\omega^2\right) \qquad (30)$$

The random variable ω has a rounding effect on C_z. If σ_ω^2 is large, the matrix becomes the marginal matrices discussed in section 2.3. This intuitively also makes sense, as the dependency on the angle ω should be lower if the uncertainty in ω is large. This also indicates that the error induced by approximating $\mathrm{cov}\,(z)$ by $\mathrm{cov}\,(z|\omega)$ may be significant if σ_ω^2 is large.

Returning to equation (20), if σ_θ^2 was known, then equations (27), (28), and (30) could be used directly to estimate the B term. However, as discussed previously, σ_θ^2 is a function of target state. The proposed solution is thus to estimate the B term using a HOUT. The rotation matrix $\Phi\left(x_k\right)$ is a function of the position of the target through $\phi = \arctan p^y/p^x$. For many tracking applications the range will be larger than the variances of the position errors. $\Phi\left(x_k\right)$ can then be approximated by $\Phi\left(\bar{x}_k\right)$, where $\bar{\phi}_k = \arctan\left(\bar{p}_k^y/\bar{p}_k^x\right)$. The D term equation (20), thus becomes

$$D = \Phi\left(\bar{\phi}_k\right) R_k^C \Phi^T\left(\bar{\phi}_k\right)$$

where R_k^C is defined in equation (3). Possible exceptions include tracking of a target close to the radar, or during initialization of a new track, in which case the estimation covariance may be very large.

3.1.1 UT approximations

The unscented transform using the symmetric set is here shown to be unable to handle nonlinear transforms in the form of rotation. Consider again the system in equations (21)-(24), and define the augmented system given by the following equation.

$$x^a = \begin{bmatrix} 0 \\ 0 \\ 0 \end{bmatrix}, P^a = \begin{bmatrix} \sigma_a^2 & 0 & 0 \\ 0 & \sigma_b^2 & 0 \\ 0 & 0 & \sigma_w^2 \end{bmatrix}$$

The UT applying the symmetric set can easily be shown to give $\hat{C}_z = Q = diag\left(\sigma_a^2, \sigma_b^2\right)$. However, assuming that both x and ω are Gaussian, C_z was shown by derivations in the previous paragraph to be equal to the matrix which entries are given by equation (27), (28), and (30).

The proposed solution was to apply the higher order unscented transform (HOUT) introduced in [12]. The HOUT consists of $2N_x^2 + 1$ points and approximates up to the fifth order terms of the pdf. The transform is defined by a number of sigma points that can be divided into three classes. The first point is located at the origin and has weight w_0. One class of points have weights w_1 and are located on the axes, at $[\pm s_1, 0, ..., 0]^T$, $[0, \pm s_1, ..., 0]^T$,..., $[0, 0, ... \pm s_1]^T$. Another class of points with weights w_2 are located at all possible permutations of $[\pm s_2, \pm s_2, 0, \ldots, 0]^T$. For instance if $N_x = 3$ this set is given by $[s_2, s_2, 0]^T$, $[-s_2, s_2, 0]^T$, $[-s_2, -s_2, 0]^T$, $[s_2, -s_2, 0]^T$, $[s_2, 0, s_2]^T$, $[-s_2, 0, s_2]^T$, $[-s_2, 0, -s_2]^T$, $[s_2, 0, -s_2]^T$, $[0, s_2, s_2]^T$, $[0, -s_2, s_2]^T$, $[0, -s_2, -s_2]^T$, $[0, s_2, -s_2]^T$. Given a covariance matrix P and a mean vector m, the sigma points of the transformation are calculated by $y^i = m + \sqrt{P}x^i$. The constants w_0, w_1, w_2, s_1, and s_2 are given as solutions to the equations

$$w_0 + 2N_x w_1 + 2N_x\left(N_x - 1\right) w_2 = 1$$
$$2w_1 s_1^2 + 4\left(N_x - 1\right) w_2 s_2^2 = 1$$
$$2w_1 s_1^4 + 4\left(N_x - 1\right) w_2 s_2^4 = 3,\ 4w_2 s_2^4 = 1$$

The general solution to these equations is

$$w_0 = \frac{(N^3 + N^2 - 4s_2^2N^2 - 2N + 4s_2^2N + 4s_2^4N - 8s_2^4)}{2(N-4)s_2^4}$$

$$w_1 = \frac{(-N + 1 + s_2^2)^2}{2(4-N)s_2^4}, w_2 = \frac{1}{4s_2^4}, s_1 = \sqrt{\frac{s_2^2\left(N-4\right)}{N-1-s_2^2}}$$

In [12] it is proposed to select the solution that minimizes the sixth order moment

$$\left|2w_1 s_1^6 + 4\left(N_x - 1\right) w_2 s_2^6 - 15\right|$$

For $N_x = 3$, the solution is $s_2 = \frac{1}{2}\sqrt{18 - 2\sqrt{21}}$, and $N_x = 2$ gives $s_2 = \sqrt{6 - \sqrt{21}}$. Note that when $N_x = 4$, the only solution is given by $s_2 = \sqrt{3}$, $w_0 = \frac{1}{3}$, $w_1 = 0$, $w_2 = \frac{1}{36}$, and the number of points then reduces to 25. For $N_x = 5$, the solution is $s_2 = \sqrt{3}$. A plot of the approximation of the system in equation (21)-(24) is shown in figure 6. The approximation is good up to $\sigma_\omega^2 = \frac{\pi}{2}$, which corresponds to ω being widely distributed on $[-\pi, \pi]$. The HOUT may be extended to even higher orders to improve the approximation seen in figure 6. The number of points would increase significantly, but the computational load may still be lower than that of a particle filter or similar Monte Carlo methods.

The B term in equation (20), $E\left(\Gamma_k \Theta\left(x_k\right) w_k^O w_k^{OT} \Theta^T\left(x_k\right) \Gamma_k^T\right)$, can be approximated in several ways. The straightforward solution

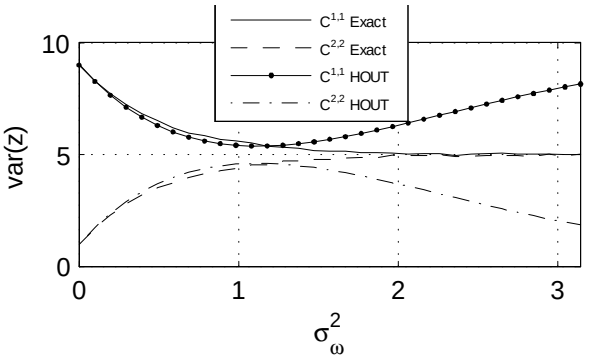

Figure 6: Plot of HOUT approximation of $C_z^{1,1}$ and $C_z^{2,2}$ of equation (27) and (28). $\sigma_a^2 = 3^2$, $\sigma_b^2 = 1$.

is to use the HOUT with $N_x = 4$, using the following augmented system.

$$x^a = \left[v_k^x, v_k^y, w_k^O\right]^T, \; h\left(x^a\right) = \Theta\left(\arctan\left(\frac{v_k^y}{v_k^x}\right)\right) w_k^O$$

$$P^a = \begin{bmatrix} P_k^{'} & 0 \\ 0 & R_k^O \end{bmatrix}, \; P_k' = \mathrm{cov}\left(\left[v_k^x, v_k^y\right]^T\right)$$

P_k' can be extracted from the prior covariance matrix $\bar{P}_k$. This solution requires 25 sigma points of dimension 4. A more computationally efficient method would be to estimate σ_θ^2 at each step and insert directly into equation (27), (28), and (30). The angular variance can be estimated using an UT on the system

$$x^a = \left[v_k^x, v_k^y\right]^T, \; h\left(x\right) = \arctan\left(\frac{v_k^y}{v_k^x}\right)$$

$$P^a = \mathrm{cov}\left(\left[v_k^x, v_k^y\right]^T\right)$$

where P^a is extracted from the prior state covariance matrix $\bar{P}_k$. However, the selected solution was to approximate the terms $E\left(\cos^2\theta\right)$ and $E\left(\sin 2\theta\right)$ in equations (26) and (29) respectively using a HOUT with N=2. Using that $\cos^2 \arctan y/x = x^2/(x^2+y^2)$ and $\sin 2y/x = 2xy/(x^2+y^2)$, the terms $E\left(\cos^2\left(\omega\right)\right)$ and $E\left(\sin 2\theta\right)$ can be estimated by a UT on the following system

$$x^a = \left[v_k^x, v_k^y\right]^T, \; P^a = \mathrm{cov}\left(\left[v_k^x, v_k^y\right]^T\right)$$

$$h_1\left(x\right) = \frac{v_x^2}{v_k^{x2} + v_k^{y2}}, h_2\left(x\right) = \frac{2v_k^x v_k^y}{v_k^{x2} + v_k^{y2}}$$

The B term can then be approximated by inserting the estimated terms into equations (26) and (29).

3.2 Biased measurements

The treatment of the bias b_k^1 proposed in section 2.2 is left out in this paper, as it poses no problem to the estimator. For the biases defined in equations (16) and (17), it was not possible to find a closed form solution of C_{xz} and C_z, and the proposed solution was to approximate the nonlinear expressions in the BLUE filter using HOUTs.

4 Simulations

4.1 Trajectory generator

The target trajectories in the MC simulations were generated using a Jump Markov Non Linear structure, as introduced in [4]. The main idea of the trajectory generator is to generate random sequences of maneuvers with similar dynamics to what is encountered in the considered application. The trajectories are generated by a non stationary Markov chain, and a set of discrete system models are used to calculate the target state during each maneuver. Following [4], the model set consisted of a nearly constant velocity state, a set of states with positive acceleration and a set of states with negative acceleration, a set of states with counterclockwise turns, and a set of states with clockwise turns. In this paper, the model was used mainly for simulation purposes and was constructed without the use of real trajectories. However, as discussed in [4] the setup could be used to extract the dynamics of targets from historical data, for instance by using the approach described in [13]. The extracted dynamics can then be used to generate trajectories which can be used for benchmark test and simulations.

The system model in the simulations was built up as presented in [4]. However, in this paper, the transition matrix M and the model set was modified. Firstly, the number of possible maneuvers were higher. Secondly, M was constructed such that the Markov chain had a higher probability of jumping to a neighbor state than to other states when it was in an acceleration or turn state. A neighbor state was defined as the state with turn rate or acceleration rate closest to the current state. In this manner, less rigid maneuvers were generated. A maneuver was then defined to last as long as the system remained in the same state or jumped to a neighbor state.

4.2 Estimation filters

The estimation filter were interacting multiple models (IMM) filters applying different combinations of kinematic models. The kinematic system models applied to generate the results shown in this paper were a nearly constant velocity model and a coordinated turn model. In addition, a kinematic model introduced in [6] was implemented using BLUE filters and included into the IMM framework. This model is described in the following subsection.

4.2.1 State prediction

In the direct discrete nearly constant velocity kinematic model, the velocity in each dimension is modeled as integrated white noise. In the coordinated turn model, the turn rate is modeled as a Wiener process and implicitly estimated at each time step. A formulation of the equation of both these system models can also be found for instance in [10]. The nonlinear coordinated turn model was implemented using an HOUT, as the coordinated turn model implicitly includes a rotation of the state vector. Simulations showed that the HOUT gave a significantly better approximation than the symmetric set, but that the symmetric set still showed better performance than an extended Kalman filter implementation.

In [6] a system model was presented where the process noise is defined in the reference frame of the target. The model was applied for targets that were assumed to have higher lateral acceleration than thrust acceleration. However, for the system considered in this pa-

per, the model was applied to model constant thrust acceleration. The coordinated turn model was shown in simulations to have better RMSE performance during turns than the proposed model. The model was formulated for three dimensions in [6], but adapted to two in this work. In [6], the system equation was given by the linear equation $x_{k+1} = F_k x_k + \Gamma_k v_k$, but process noise covariance was assumed to be given by

$$E\left(w_k w_k^T\right) = \Theta(x_k) Q_k \Theta^T(x_k) \tag{31}$$

where

$$Q_k = \begin{bmatrix} q_a^2 & 0 \\ 0 & q_t^2 \end{bmatrix}$$

q_a^2 is proportional to thrust accelerations and q_t^2 is proportional to lateral accelerations. The process noise matrix was approximated using $\Theta(x_k) \approx \Theta(\hat{\theta}_k)$ where $\hat{\theta}_k = \arctan\left(v_k^y / v_k^x\right)$, and the predicted covariance matrix was approximated by

$$\bar{P}_{k+1} = F_k \hat{P}_k F_k^T + \Gamma_k \Theta(\hat{x}_k) Q_k \Theta^T(\hat{x}_k) \Gamma_k^T \tag{32}$$

It is in this paper proposed to reformulate this system by the following equation.

$$x_{k+1} = f_k\left(x_k, w_k\right) = F_k x_k + \Gamma_k \Theta\left(x_k\right) w_k \tag{33}$$

The process noise is then uncorrelated with the state vector. The predicted state and covariance is thus given by

$$\bar{x}_{k+1} = F_k \hat{x}_k \tag{34}$$

$$\bar{P}_{k+1} = F_k \hat{P}_k F_k^T + \Gamma_k E\left(\Theta\left(x_k\right) v_k v_k^T \Theta^T\left(x_k\right)\right) \Gamma_k^T \tag{35}$$

The term $\hat{Q} = E\left(\Theta\left(x_k\right) v_k v_k^T \Theta^T\left(x_k\right)\right)$ was approximated using a HOUT. Approximating the process noise covariance by the conditional process noise covariance may induce errors in the system, in the same manner as approximating the measurement covariance by its conditional covariance. The effect of the HOUT approximation is to round the process noise covariance matrix. If the uncertainty in heading angle is large, $\hat{Q}$ becomes a diagonal matrix with equal entries on the diagonal. The model is then effectively a nearly constant velocity model.

4.2.2 Implementation

The recursive BLUE filters were implemented using unscented transforms when necessary. The structure proposed in [5], where each term in the recursive BLUE filter is estimated by unscented transforms, was not implemented. For instance for the case where the dynamic model was given by equation (33), then a HOUT was applied to estimate $E\left(\Theta\left(x_k\right) v_k v_k^T \Theta^T\left(x_k\right)\right) \Gamma_k^T$, while the terms $F_k \hat{P}_k F_k^T$ and $\bar{x}_{k+1}$ were calculated directly. The predicted covariance $\bar{P}_{k+1}$ was then estimated as the sum of these two terms. In the same manner, if the measurement model was given by $z_k = Hx + b_k + w_k$ where w_k was white additive noise and b_k was a state dependent bias, then $E\left(x_k\left(Hx_k + b_k^T\right)\right)$, $E\left(\left(Hx_k + b_k\right)\left(Hx_k + b_k\right)^T\right)$ as well as $\bar{z}_k$ was estimated using a HOUT. $E\left(w_k w_k^T\right) = R_k$ and $E\left(x_k x_k^T H^T\right) = \bar{P}_k H^T$ could be evaluated directly. The matrices in the BLUE filter were then estimated by $C_{xz} = E\left(x_k\left(Hx_k + b_k^T\right)\right)$ and $C_z = E\left(\left(Hx_k + b_k\right)\left(Hx_k + b_k\right)^T\right) + R_k$. Using an HOUT on the block diagonal augmented system proposed in [5] would require 65 sigma points of dimension eight for this case. The computational load at each step may be significantly decreased using the approach proposed here, which requires two HOUTs of dimension four.

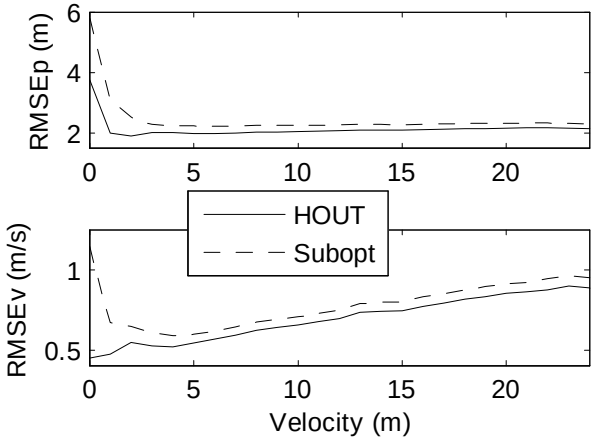

Figure 7: RMS position and velocity errors for HOUT estimation filter vs suboptimal filter plotted as function of target velocity. Biased measurements generated by equation (16) with $\alpha = 10$.

4.3 Simulation results

4.3.1 Bias estimates

The setup described in section 4.1 was used to generate random trajectories. The parameters of the trajectory generator were chosen such that the system spent 44% of the time in the constant velocity state, 30% in a turn and 26% in a state of acceleration. The mean distance traveled in the constant velocity state was 400 m, the mean turn was $\Delta\theta = \frac{3\pi}{16}$, and the mean acceleration was $\Delta v = 2\,\mathrm{m/s}$. The system consisted of 32 acceleration states with thrusts uniformly distributed on the interval $[-0.3, 0.3]\ \frac{m}{s^2}$, and 32 turn states with turn rates uniformly distributed on the interval $[-0.08, 0.08]\ \frac{\mathrm{rad}}{\mathrm{s}}$. The velocity was constrained to be in the interval $v \in [0, 25]\ \frac{\mathrm{m}}{\mathrm{s}}$. The added process noise in each dimension had a variance of $\sigma_q^2 = 0.01$. The biased measurement for the simulations were generated using equation (16) and (17), with additive and Gaussian noise with $R_k = E\left(w_k w_k^T\right) = diag\left(5^2, 5^2\right)$. The

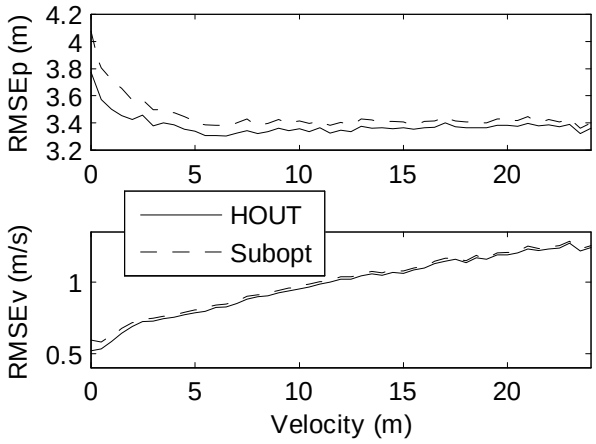

Figure 8: RMS position and velocity errors for HOUT estimation filter vs suboptimal filter plotted as function of target velocity. Biased measurements generated by equation (17) with $\alpha = 10$.

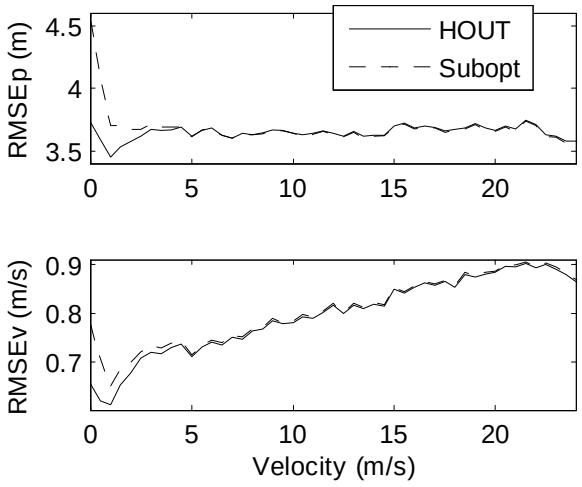

Figure 9: Comparison between HOUT BLUE filter and suboptimal filter plotted as function of target velocity. State dependent measurement noise generated by equation (9) with $R = diag(5, 1)$.

recursive filter was implemented as an IMM filter. The IMM filter consisted of a constant velocity model, a coordinated turn model and an acceleration model. The results in figure 7 show the RMSE errors of two estimations filter plotted against velocity. The performance of the BLUE filter was compared to a suboptimal filter which estimated the bias at each scan using the predicted state vector. The RMSE was plotted as a function of velocity using a histogram approach, where the mean RMSE within bins of 0.5 m / s were calculated. The plot shows how the BLUE filter clearly has better accuracy for low velocities, when the uncertainty in the estimated heading angle is large. This is expected given the discussion in section 3. Figure 8 shows an example where the measurements were generated using the bias model in equation (17). The plot shows the same effect for low velocities, but not as significant as for equation (16).

4.3.2 Correlated measurement noise and aspect angle

In this simulation, the measurements were generated using equation (9), where the eigenvectors of the conditional measurement error covariance matrix is aligned with, and normal to the velocity vector. A HOUT BLUE filter was compared to a suboptimal filter, which approximated the measurement noise covariance by the error covariance conditioned on the predicted state vector. The plot in figure 9 shows how the BLUE filter again outperformed the suboptimal filter at low velocities. The figure also indicates that the suboptimal filter is approximately optimal in cases where the error in the heading angle is low, which may be the case for scenarios with large velocities and relatively low measurement errors.

4.3.3 Tracking an extended target

In the following example, the performances of estimation filters applying the measurement models in equations (4), (9) and (11) were compared. The measurements were generated by the simulation framework from [3], using the same target model that was used to generate the parameter estimates shown in figure 2, 3 and 4. The parameter estimates were used as input to the estimation filters. The dependency on range was assumed to be small enough to be ignored, such that the measurement errors in range could be conditioned on the predicted range. A large number of trajectories were generated within the range $r \in [1, 20]$ km, and a simulated radar measurement was generated at each scan. Figure 10 shows the RMSE performance of the 3P model, and figure 11 shows how the 3P model performs better than the two other models for all ranges. It also indicates that the C model is a better fit than the O model for $r > 15$ km. This is higher, but comparable, to 13 km where the KLD of the O model becomes higher than the C model.

5 Conclusion

Optimal BLUE filters have been derived for several different measurement models. A measurement model that assumes that the process noise error covariance is dependent on both the position and aspect angle of the target has been incorporated in a BLUE filter, and the goodness of the model has been evaluated using RMS position and velocity errors as performance measures. Using simulated radar measurements as input to IMM tracking filter applying the BLUE measurement models, it is shown how the new model is best both at short and

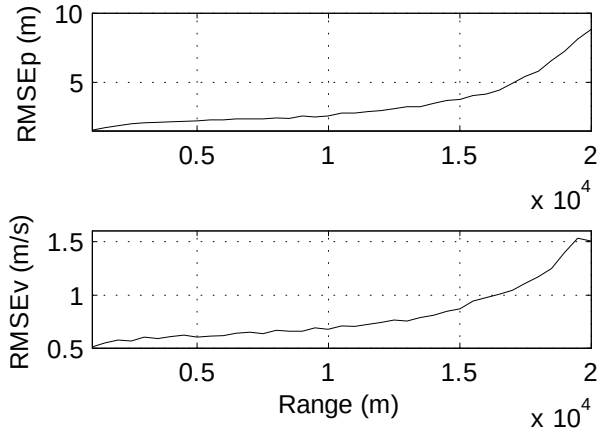

Figure 10: Position and velocity performance for IMM estimation filter applying a BLUE filter on the 3P measurement model.

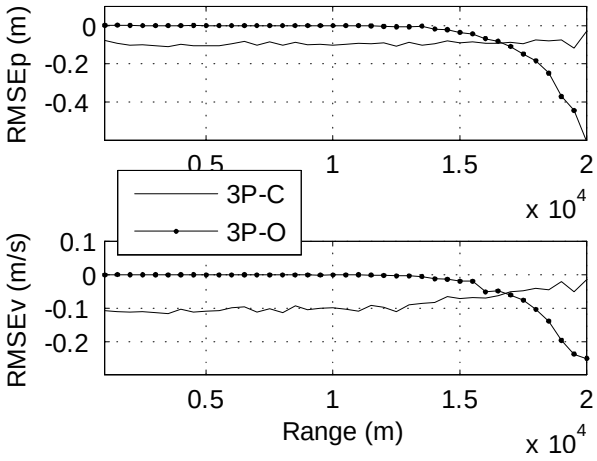

Figure 11: Difference between RMSE performance of BLUE filter applying the 3P model and BLUE filters applying the O and C models.

long range. Some target dependent biases were also introduced, and it is shown in simulations how the derived BLUE filters have better performance than suboptimal filters for state dependent measurement errors.

The work has also shown how higher order unscented transforms may be used to approximate the terms in the BLUE filters, and that a higher order transform is needed for cases where the measurements or process noise is transformed by a rotation.

References

[1] X. R. Li and V. P. Jilkov, "A survey of maneuvering target tracking - part iii: Measurement models," in *Proceedings of SPIE - The International Society for Optical Engineering*, vol. 4473, 2001, pp. 423–446.

[2] Z. Zhao, X. R. Li, and V. P. Jilkov, "Best linear unbiased filtering with nonlinear measurements for target tracking," *IEEE Transactions on Aerospace and Electronic Systems*, vol. 40, no. 4, pp. 1324–1336, 2004.

[3] M. Stakkeland, Ø. Overrein, and O. Hallingstad, "The error statistics of surveillance radar position measurements," in *The Proceedings of Radar 2007, the IET International Conference on Radar Systems*, 2007.

[4] ——, "Tracking and fusion of surveillance radar images of extended targets," in *The Proceedings of FUSION 2007, the 10th International Conference on Information Fusion*, 2007.

[5] S. Julier and J. Uhlmann, "Unscented filtering and nonlinear estimation," *Proceedings of the IEEE*, vol. 92, no. 3, pp. 401–422, 2004.

[6] J. D. Parker and W. D. Blair, "Use of target-oriented process noise in tracking maneuvering targets," Naval Surface Warfare Center, Tech. Rep., 1992.

[7] Y. D. Shirman, Ed., *Computer Simulation of Aerial Target Radar Scattering, Recognition, Detection, and Tracking*. Norwood, MA: Artech House, 2002.

[8] C. Arndt, *Information measures*. Springer Verlag, 2001.

[9] A. Rødningsby and Y. Bar-Shalom, "Tracking of divers using a probabilistic data association filter with a bubble model," *To appear in IEEE Transactions on Aerospace and Electronic Systems*, 2009.

[10] Y. Bar-Shalom, X. R. Li, and T. Kirubarajan, *Estimation with applications to tracking and navigation*. New York, NY: Wiley, 2001.

[11] J. Romine and E. Kamen, "Modeling and fusion of radar and imaging sensor data for target tracking," *Optical Engineering*, vol. 35, no. 3, pp. 659–673, 1996.

[12] S. Julier and J. Uhlmann, "A consistent, debiased method for converting between polar and cartesian coordinate systems," in *The Proceedings of AeroSense: The 11th International Symposium on Aerospace/Defense Sensing, Simulation and Controls*, 1997.

[13] J. Garcia, J. Molina, J. Besada, and G. de Miguel, "Model-based trajectory reconstruction using imm smoothing and motion pattern identification," in *The Proceedings of FUSION 2007, the 10th International Conference on Information Fusion*, 2007, pp. 1–2.

Appendices

A

Additional results: Monte Carlo simulations of extended targets

A.1 Generation of measurements

A typical target that was used in the simulations is shown in figure A.1. The targets were modeled as a large number of scattering objects that were uniformly distributed over a given area. The radar cross sections of the scatterers were modeled to be equal in most of the simulations. The positions of the point scatterers were kept fixed relative to each others, while the position and orientation of the target varied.

The methods and simplified system models described in section 3 and paper three were applied to generate high resolution target images, as shown for instance in figure A.2. The magnitude on the z-axis of the plot is not significant, given that noise was added to the target images to match a specified SNR.

A target image with realistic sampling grid and noise could then be generated, by sampling the high resolution target image and adding noise in each pixel. An image sampled from figure A.2 is shown in figure A.3. For each generated high resolution (HR) image, the sampling grid was located in a number of different locations in order to take the influence of the placement of

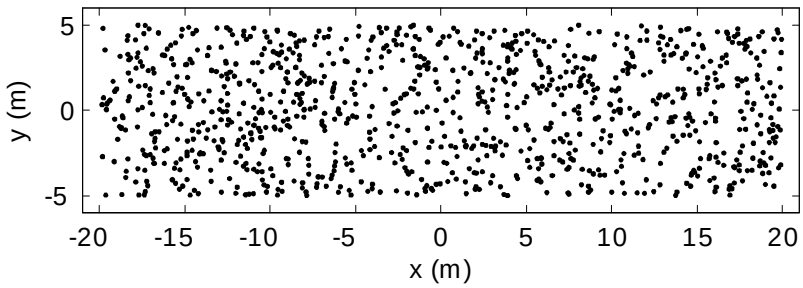

Figure A.1: *Target constructed by 1000 point scatterers.*

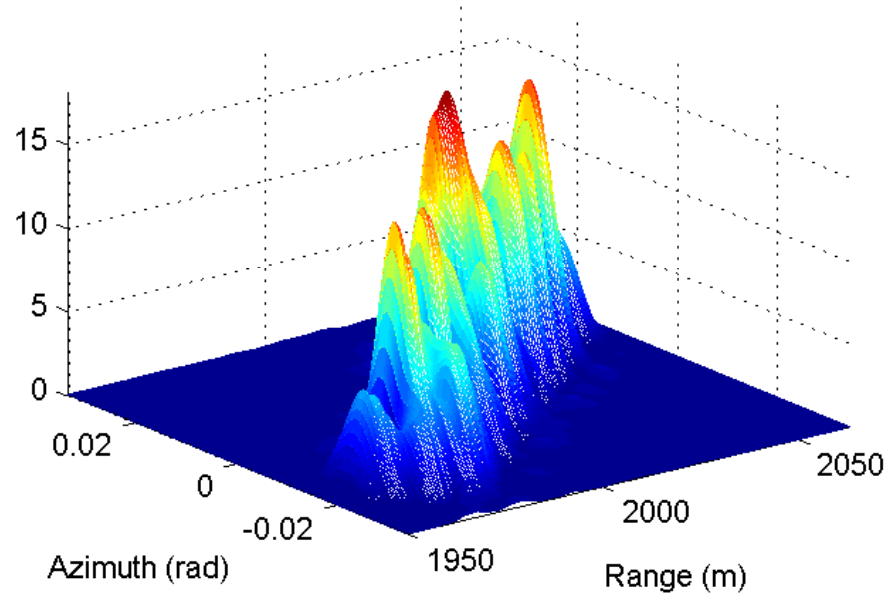

Figure A.2: *Simulated high resolution radar image. Target consisting of 4000 point targets. Target center located at 2000 m range, with a 45° aspect angle.*

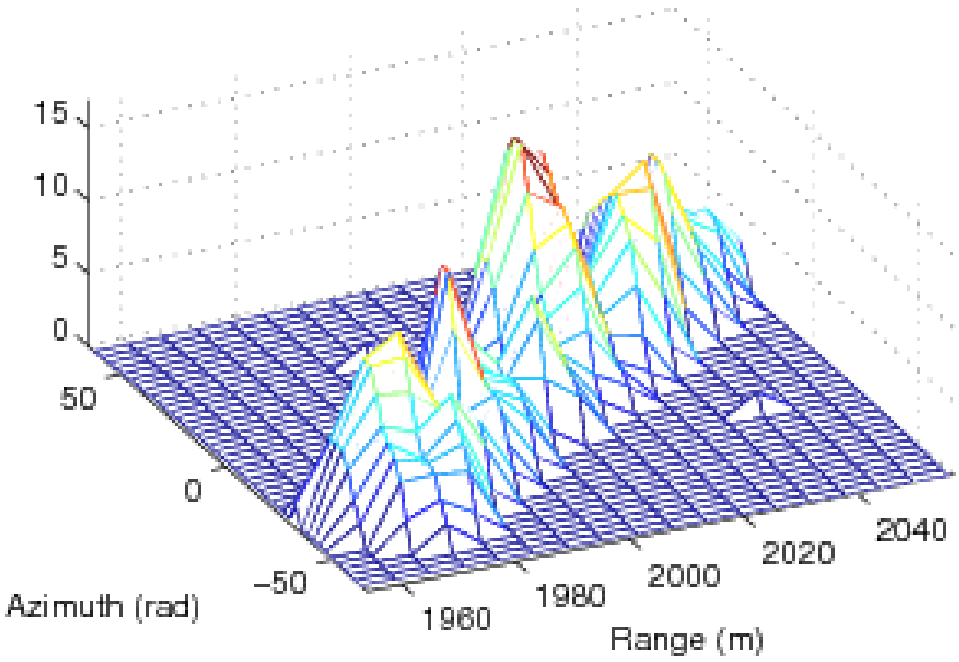

Figure A.3: *Target image, with sampling grid of 6* m *in range and* $\frac{2\pi}{4096}$ rad *in azimuth, and 15 dB SNR.*

the sampling grid into account.

A close to ideal segmentation procedure was performed before adding Ricean noise and generating centroid measurements. Firstly, the radar image was cropped 2 lobewidths outside the target limits in bearing. The radar image is finite in range, but is in principle infinite in bearing because of the sidelobes of the aperture function. Secondly, the SNR input parameter was used to calculate the noise parameter to the Ricean distribution, before a threshold was set such that the false alarm rate was set to 10^{-3}. The thresholded image was then used to generate the centroid measurements. The position of each pixel was transformed to Cartesian coordinates before a centroid was calculated.

Figure A.4 and A.5 show images generated by the same target, but with a $0.05\,^{\circ}$ difference in aspect angle. Figure A.4 is a contour plot of the data shown in figure A.2. The plots clearly show how a very small change in sensor target geometry may induce significant changes in the target image, which is defined as speckle noise. The figures A.6 and A.7 show 2000 generated measurements from the corresponding figures A.4 and A.5. The measurements were generated with an SNR of 20 dB.

The results illustrate several properties of these simulations. First and most important, they illustrate how there is a correlation between aspect angle and measurement error, as the generated centroids are aligned along the heading of the target. The second point which is illustrated is how the measurement error here is the sum of a components generated by the noise in each pixel, the influence of the placement of the sampling grid, and the speckle noise in the target images. Measurements thus have to be generated over several aspect angles in order to obtain estimates of

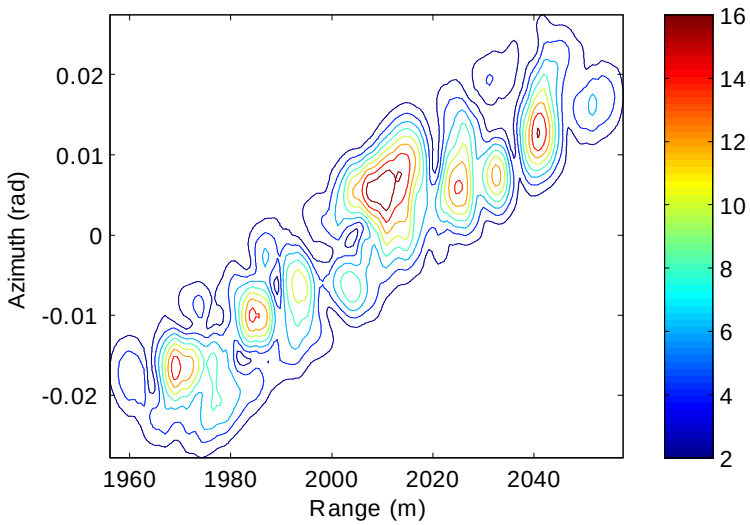

Figure A.4: *Contour plot of generated radar image, aspect angle 45.00°.*

the measurement error statistics. A third point is that the measurements for a given position and aspect angle may deviate from the commonly assumed Gaussian distribution. The simulations showed that they were more close to a Gaussian distribution for low SNRs.

A.2 ML estimation

The following subsections contain five examples where Monte Carlo simulations were used in order to examine the influence of one or more parameters on the estimated error models.

A.2.1 Example 1 - Parameter estimation for a target with constant SNR

The target model used in this example consisted of 1000 point targets uniformly distributed over a rectangular area with dimensions 40x10 m. The system was modeled as described in chapter 3, with a rectangular pulse waveform with pulse length of 12 m, and with the angular response function given by equation (3.15). The lobewidth was 0.5°, where the width was defined as the interval between maximum and first zero. The sampling intervals in range and azimuth were 6 m and $\frac{2\pi}{4096}$ rad respectively.

In the simulations, the target was placed on the x-axis and moved from a distance of 200 m to 100 km. The target was rotated around its center in 360 steps, and 98000 measurements were generated for each aspect angle. A total of 670 million simulated measurements were thus used for parameter estimation. The SNR of the target was kept constant at 20dB for all distances.

The parameters of model C, O and 3P given in section 3.3.6 were estimated based on the set of generated centroids. For model C, the estimation consisted of calculating the sample mean and covariance matrix of all the generated measurements in the Cartesian frame. The corresponding estimate for model O was obtained by rotating all the generated measurements into the reference

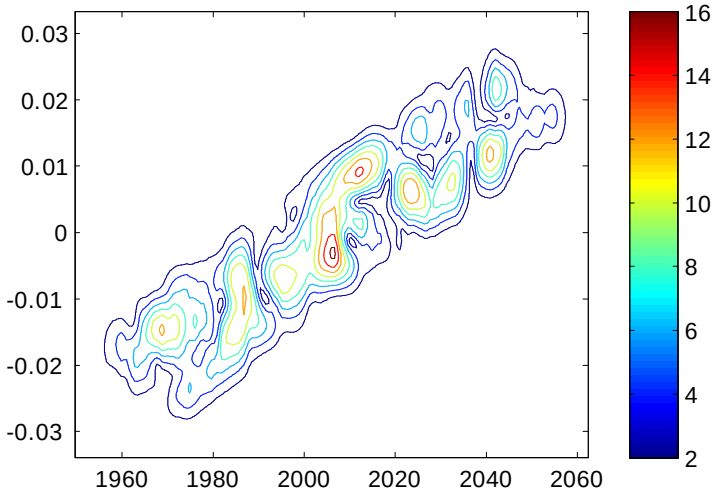

Figure A.5: *Contour plot of generated radar image, aspect angle 45.05°.*

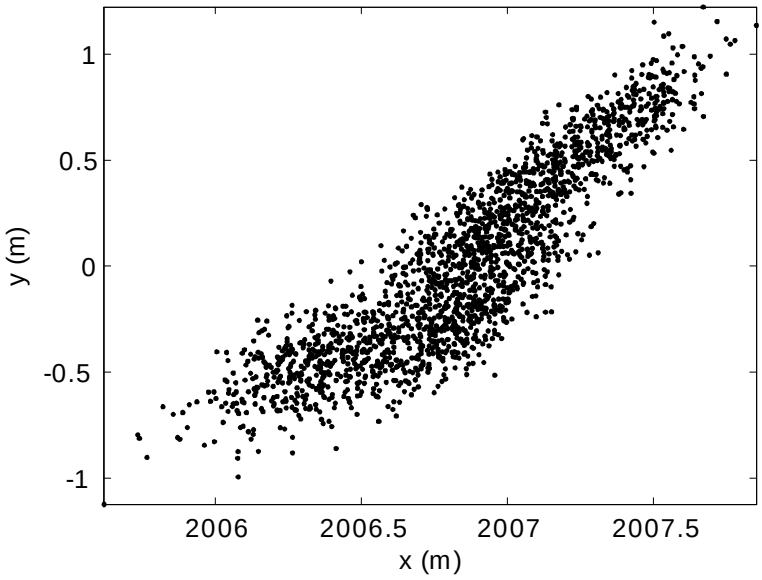

Figure A.6: *One batch of generated measurements, aspect angle 45.00°.*

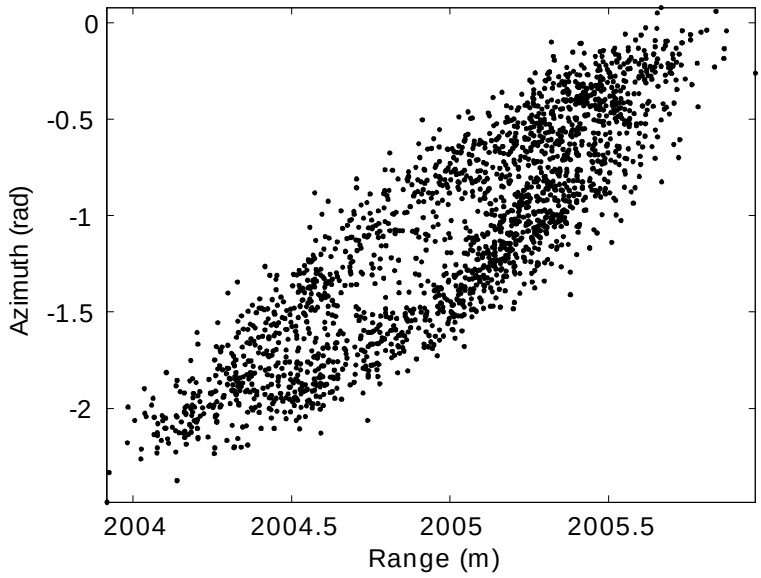

Figure A.7: *One batch of generated measurements, aspect angle 45.05°.*

frame of the target, and then calculating the sample mean and covariance matrix. The fmincon() numerical search algorithm in MATLAB was used to estimate the parameters for model 3P.

The ML estimates for the parameters of the three measurement models are shown in figure A.8, A.9 and A.10. Figures A.8 indicate that the common model applied in tracking systems, to assume that σ_r is constant and that $\sigma_{\phi*} = r\sigma_\phi$ where σ_ϕ is a constant may be plausible in cases where the SNR is constant. Figure A.10 shows how the angular parameter of model 3P is approximately linear with range.

The estimated symmetrized KLD is shown figure A.11. The KLD was estimated as a mean value over all the 360 aspect angles for each specific distance, using equation (3.29), and by calculating the sample mean and covariance of the measurements generated for each of the aspect angle. The figure show how model 3P has the smallest KLD for all distances, but that it is equal to the distance of model O at short range, and similar to model C at long range. This result indicates that model O is a better approximation than model C at short range, while model C is a good approximation at long range when the target approaches a point target in bearing.

A.2.2 Example 2 - Parameter estimation with fixed position and varying SNR.

In this example, a target was located at a fixed position and the SNR was varied in order to examine the parameters of the error models as a function of SNR. The target which was used in the simulations was modeled to consist of 4000 point scatterers distributed uniformly over a 120x20 m area. The target was located at $r = 20\,\mathrm{km}$. The target was rotated around its geometrical center in 0.05° increments when the SNR was 120 dB, in 0.01° increments for SNR=90 and 60 dB, and 1° increments for SNR$\leq$30 dB. A set with more than one million measurements was generated as input to the parameter estimation algorithms for each SNR value.

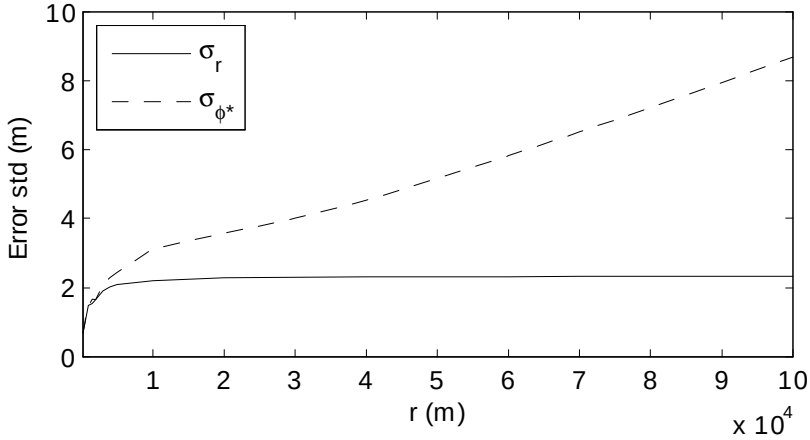

Figure A.8: *Maximum likelihood of the parameters of model C as function of range for a target with constant SNR*

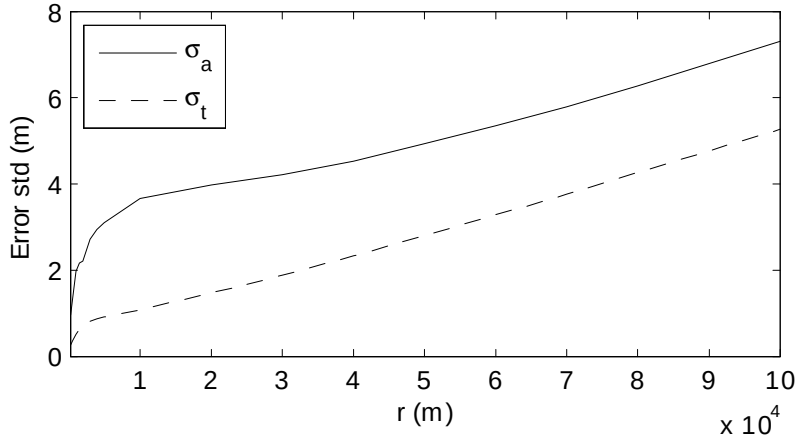

Figure A.9: *Maximum likelihood estimation of the parameters of model O as function of range for a target with constant SNR.*

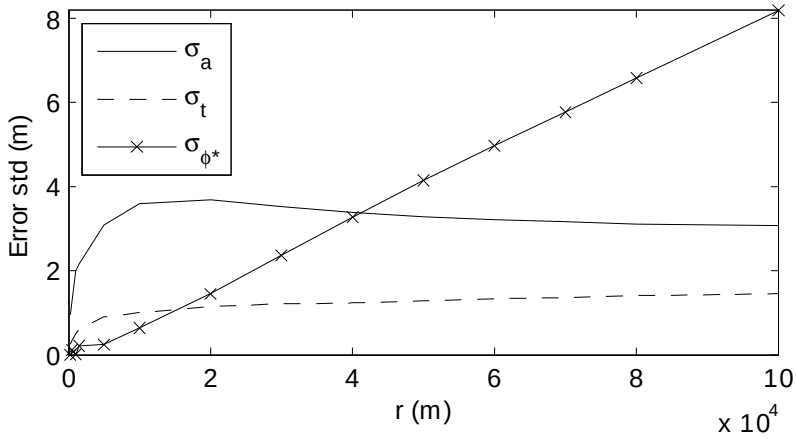

Figure A.10: *Maximim likelihood estimates of the parameters of model 3P as function of range for a target with constant SNR.*

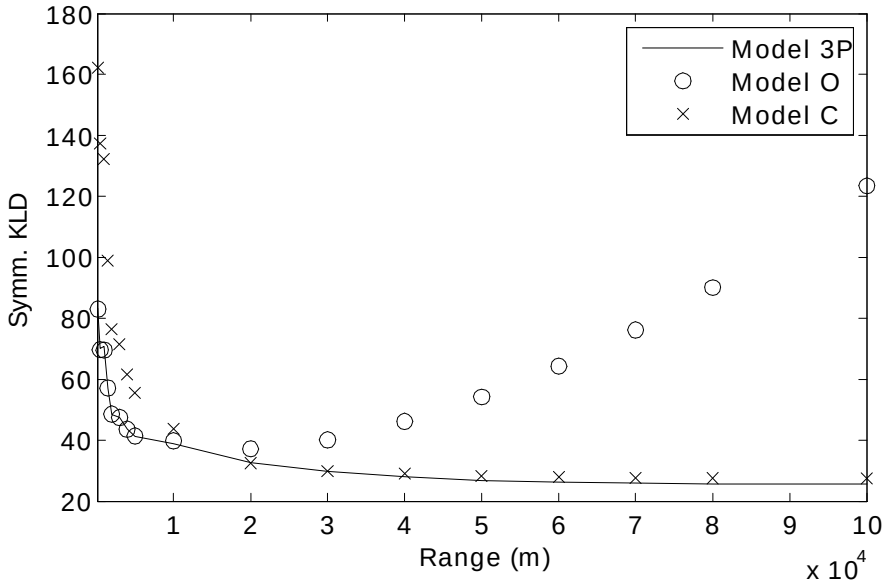

Figure A.11: *Estimated symmetrized Kullback Leibler distance between generated measurements and error models as a function of range.*

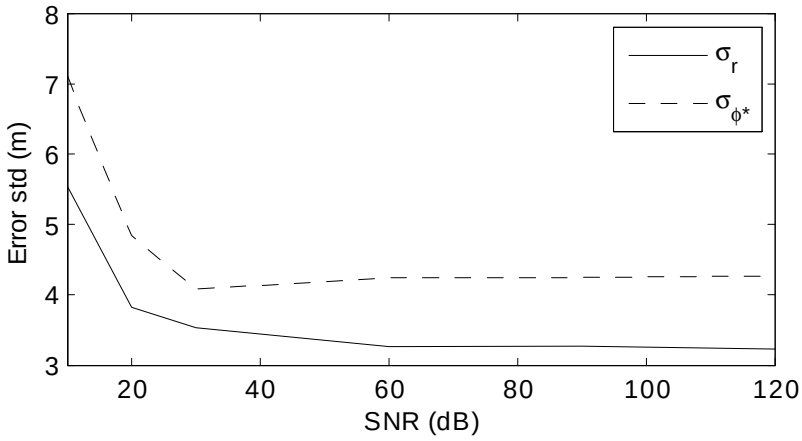

Figure A.12: *Parameter estimates for model C as function of SNR. Target located at fixed position at* $r = 20\,\mathrm{km}$.

The parameter estimates for each of the models are shown in the figures A.12, A.13 and A.14. Figures A.13 and A.14 indicate that the measurement noise covariance is constant when the SNR is higher than 30 dB. This indicates that the measurement noise is unaffected by the noise generated in each pixel, but dominated by the speckle noise in the target image. The speckle noise is independent of the SNR, which may explain the trend seen in the two graphs. Figure A.14 also show that the angular component is a function of the SNR, which also shows a correlation between SNR and the angular component. The estimated KLDs plotted in figure A.15 show that the models O and 3P are more close to the data than model C. Model 3P is equivalent to model O for all SNR except for 10 dB, given that the estimate of $\sigma_{\phi*}$ is zero. The KLD is equal to 95.7 for model O and 3P at SNR=120 dB, and they are equal with three digits precision.

A.2.3 Example 3 - Parameter estimation with target at fixed position and SNR, with varying size

This example was included in order to illustrate the relationship between target size and measurement uncertainty. The targets were rectangular areas, where the length of the target was varied, and the ratio between the length and the width was kept fixed equal to $\frac{1}{6}$. The targets were located at $20\,\mathrm{km}$, and the SNR was kept constant to 80 dB. 1000 point scatterers were used to generate the smallest target of $20\,\mathrm{m}$ x $3.3\,\mathrm{m}$, while 25000 were used to generate the largest target with a size of $500\,\mathrm{m}$ x $83.3\,\mathrm{m}$. 720000 measurements for each target size were used as input to the parameter estimation algorithms.

The results from the simulations are shown in the figures A.16, A.17 and A.18. The figures clearly indicate that there is a correlation between target size and measurement errors. From figure A.17 it can be seen that both parameters are increasing with length, although the σ_t parameter has a spike at $L = 120\,\mathrm{m}$. For the 3P model in figure A.18 it can be seen that the σ_a parameter is increasing with size, and the increase can be crudely approximated as linear. Figure A.18 also shows that there is a relationship between the angular component and target size in the simulations. This relationship is further examined in the next example.

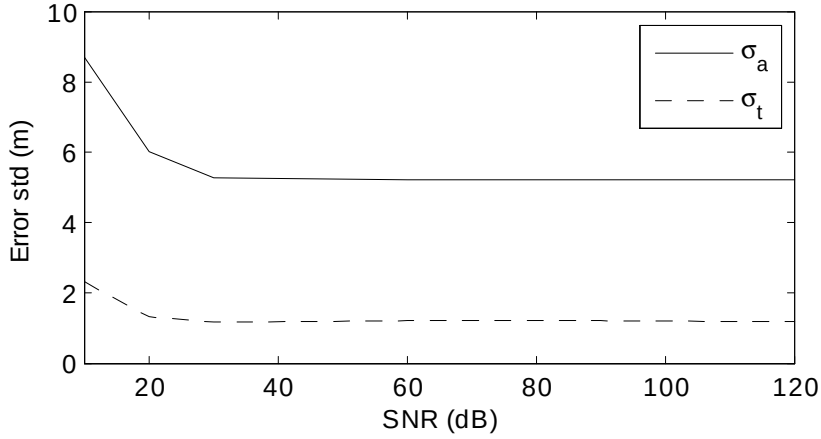

Figure A.13: *Parameter estimates for model O as function of SNR. Target located at fixed position at* $r = 20\,\mathrm{km}$.

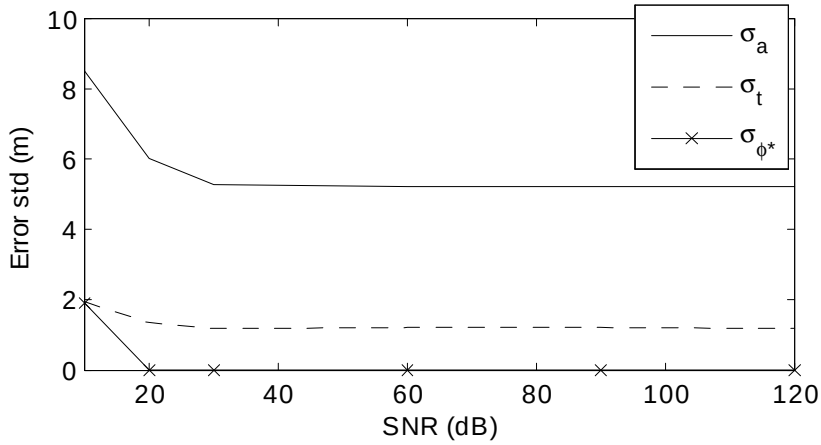

Figure A.14: *Parameter estimates for model 3P as function of SNR. Target located at fixed position at* $r = 20\,\mathrm{km}$.

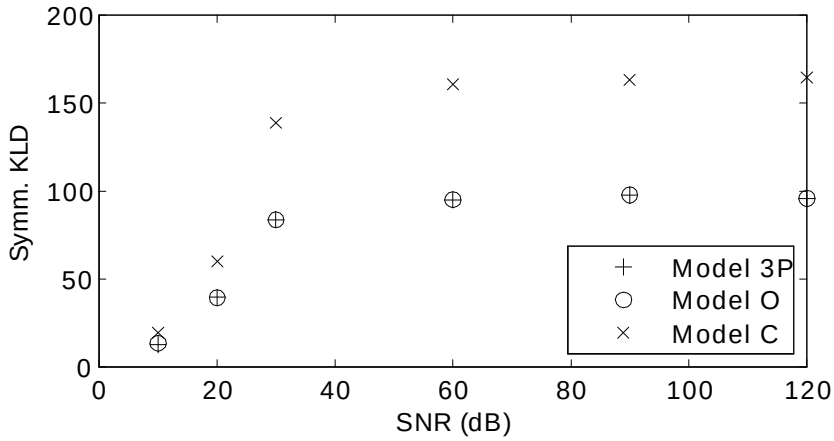

Figure A.15: *Estimated KLD between generated measurments and estimated error models as function of SNR, Target located at fixed position at* $r = 20\,\mathrm{km}$.

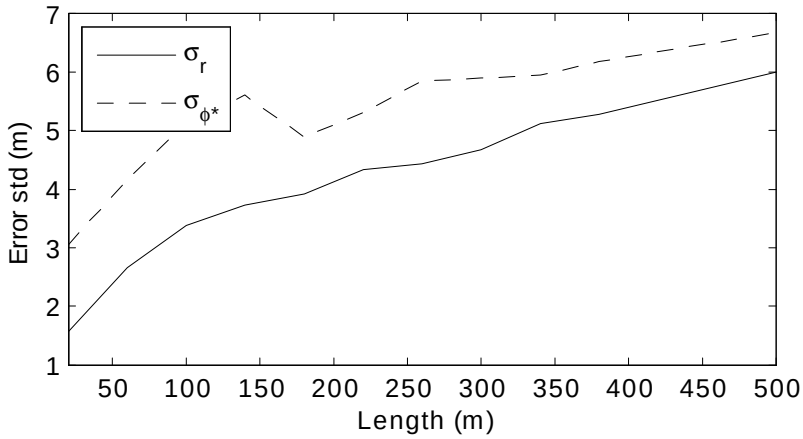

Figure A.16: *Parameter estimation as function of target size for model C.*

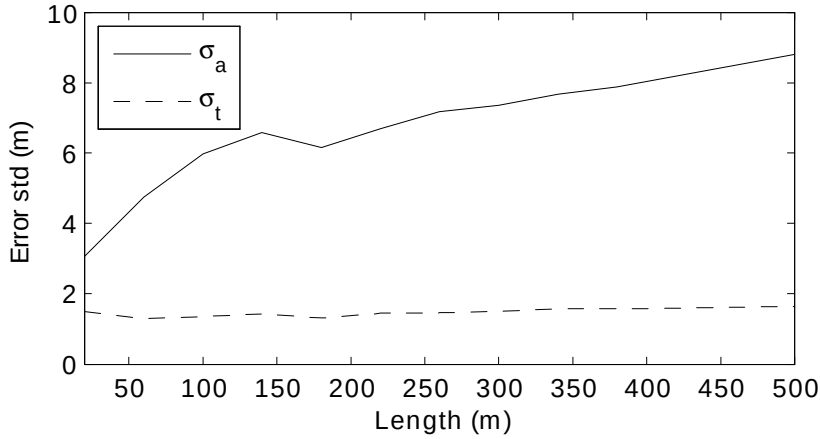

Figure A.17: *Estimated parameters as function of target size, model O.*

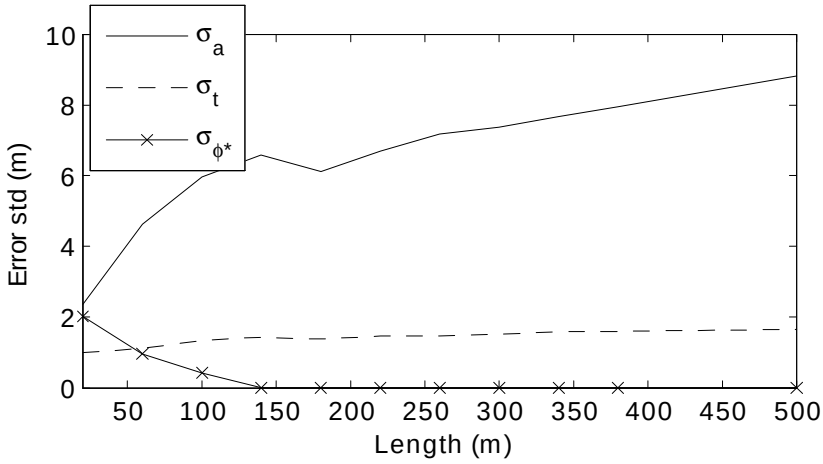

Figure A.18: *Estimated parameters as function of target size, model 3P.*

Table A.1: *Parameters of 3P model estimated as function of system resolution, defined by pulse length (PL) and Lobe width (LW)*

	LW(°)														
	0.25			0.5			1			1.5			2		
PL(m)	σ_a	σ_t	$\sigma_{\phi*}$	σ_a	σ_t	$\sigma_{\phi*}$	σ_a	σ_t	$\sigma_{\phi*}$	σ_a	σ_t	$\sigma_{\phi*}$	σ_a	σ_t	$\sigma_{\phi*}$
3	3.4	0.7	0.1	4.1	0.8	0.02	4.7	1	3E-3	5.0	1.1	3E-3	5.1	1.2	4E-3
6	3.4	0.6	0.4	4.1	0.8	0.5	4.7	0.9	0.4	5.0	1	0.42	5.2	1.1	0.5
12	4.5	0.7	0.6	5.5	0.9	0.6	6.3	1.1	0.5	6.6	1.2	0.6	6.9	1.3	0.6
20	5.4	0.9	0.6	6.7	1.2	0.7	7.6	1.4	0.7	8.2	1.5	0.8	8.5	1.6	0.8
50	6.9	1.1	0.9	8.5	1.5	1.0	10.0	1.8	1.1	10.9	2.1	1.0	11.5	2.2	1.0
100	7.9	1.2	1.1	9.8	1.6	1.3	11.8	2.0	1.7	13.0	2.3	1.8	14.0	2.5	1.8
150	8.4	1.3	1.1	10.4	1.6	1.5	12.8	2.1	2.1	14.4	2.4	2.3	15.4	2.6	2.4

Table A.2: *Paremeters of 3P model estimated as a function of sampling density in range and bearing*

	$\Delta\phi\,(\mathrm{rad})$											
	$\frac{2\pi}{4096}$			$\frac{2\pi}{2048}$			$\frac{2\pi}{1024}$			$\frac{2\pi}{512}$		
$\Delta r\,(m)$	σ_a	σ_t	$\sigma_{\phi*}$	σ_a	σ_t	$\sigma_{\phi*}$	σ_a	σ_t	$\sigma_{\phi*}$	σ_a	σ_t	$\sigma_{\phi*}$
6	7.75	1.7	4.8E-3	7.8	1.8	0.375	8.1	2.0	1.3	10.3	3.0	28.6
12	7.8	1.8	0.146	7.9	1.9	1.05	8.2	2.1	2.1	10.8	3.2	29.0
18	8.0	2.1	0.345	8.0	2.2	1.5	8.4	2.4	2.74	11.4	3.7	29.3

A.2.4 Example 4 - Parameter estimation as a function of resolution and sampling density in range and bearing

In this example, the relationship between the resolution of the system and measurement errors was examined. This was performed by using a fixed size target of 3000 point scatterers uniformly distributed over a $60 \times 10\,\mathrm{m}$ rectangular area, and changing the resolution of the system in the simulations.

The resolution was altered in two different manners. First, the lobe width and pulse length of the system model was changed, while the sampling distances in range and azimuth were kept constant at $6\,\mathrm{m}$ and $\frac{2\pi}{4096}\,\mathrm{rad}$. The target was placed at a distance of 4000 m, and rotated around its axis in 360 steps in each simulation. The SNR was set to 15 dB. A lobe width of 2° at $4000\,\mathrm{m}$ corresponds to $140\,\mathrm{m}$ in the Cartesian frame. Table A.1 shows the estimated angular parameter of model 3P for the simulated resolutions. The simulation was repeated for SNR=30 dB, and the results was similar, but with lower magnitude. The table shows how the angular component of the measurement noise is a function of the resolution in the system.

The second approach was to keep the lobe width constant equal to 0.5° and the pulse length at $20\,\mathrm{m}$ while changing the sampling resolution in range and azimuth. The results from estimating the parameters in model 3P is shown in table A.2. The SNR in the simulation was set to 15 dB, and the same target model was applied as in the table A.1 while the distance was set to $10\,\mathrm{km}$. Table A.2 clearly shows that there is a strong correlation between angular sampling distance and the angular component of the measurement accuracy.

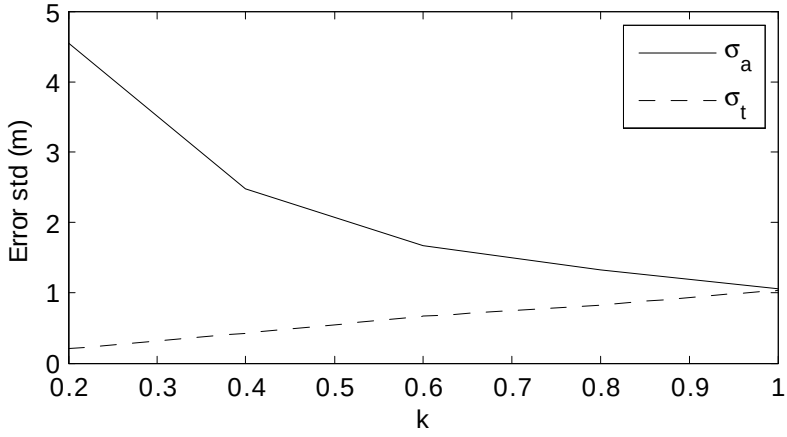

Figure A.19: *Estimated parameters for model O as a function of* $k = \frac{L}{W}$.

Example 5 - Measurement noise as function of target dimensions

This example describes simulations where the relationship between target dimensions and measurement noise was examined. This was examined by changing the width W and length L of a target, while the product $W \cdot L$ was kept constant. The target was constructed by 3000 point scatterers, and the the product $W \cdot L = 1600\,\mathrm{m}^2$. The system was modeled in the same manner as in example 1-4. The target was located at $r = 1000\,\mathrm{m}$ and the SNR was set to 20 dB such that the target was located in the region where model O is more accurate than model C. The target was rotated around its center in 360 steps for each $k = \frac{L}{W}$, and 900000 measurements were generated for each k.

Figure A.19 shows the estimated parameters for model O. The figure clearly shows how $\sigma_a = \sigma_t$ when $L = W$, which implies that the angular and range noise is uncorrelated in this case. σ_t and σ_a may be approximated as be linear functions of k, and figure A.20 shows that the product σ_t and σ_a is approximately constant. The simulations in this example thus show that there is a relationship between the aspect ratio of the target and the ratio between σ_t and σ_a.

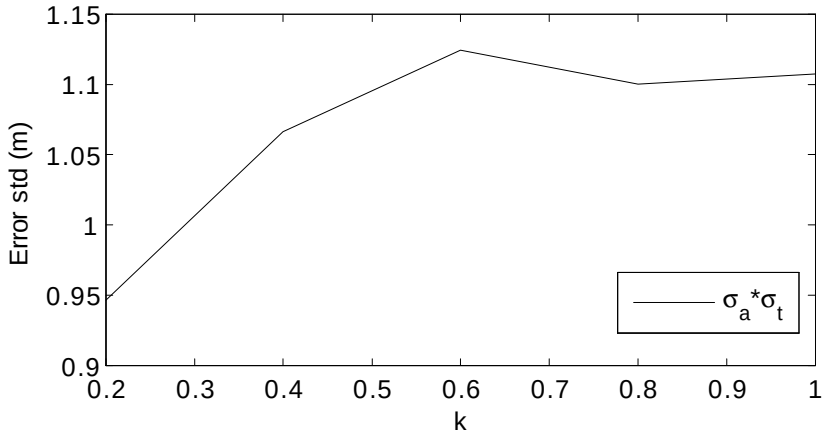

Figure A.20: *Product of estimated parameters for model O as a function of* $k = \frac{L}{W}$.